University of Alberta

SIMULATION OF THE SPUTTER REFLOW OF COPPER

by

Loran Friedich ©

A thesis submitted to the Faculty of Graduate Studies and Research in partial fulfillment of the requirements of the degree of Doctor of Philosophy

Department of Electrical and Computer Engineering

Edmonton, Alberta

Spring 1998

National Library of Canada
Acquisitions and Bibliographic Services
395 Wellington Street
Ottawa ON K1A 0N4
Canada

Bibliothèque nationale du Canada
Acquisitions et services bibliographiques
395, rue Wellington
Ottawa ON K1A 0N4
Canada

Your file Votre référence

Our file Notre référence

The author has granted a non-exclusive licence allowing the National Library of Canada to reproduce, loan, distribute or sell copies of this thesis in microform, paper or electronic formats.

L'auteur a accordé une licence non exclusive permettant à la Bibliothèque nationale du Canada de reproduire, prêter, distribuer ou vendre des copies de cette thèse sous la forme de microfiche/film, de reproduction sur papier ou sur format électronique.

The author retains ownership of the copyright in this thesis. Neither the thesis nor substantial extracts from it may be printed or otherwise reproduced without the author's permission.

L'auteur conserve la propriété du droit d'auteur qui protège cette thèse. Ni la thèse ni des extraits substantiels de celle-ci ne doivent être imprimés ou autrement reproduits sans son autorisation.

0-612-29036-0

Canada

University of Alberta

Faculty of Graduate Studies and Research

The undersigned certify that they have read, and recommend to the Faculty of Graduate Studies and Research for acceptance, a thesis entitled Simulation of the Sputter Reflow of Copper submitted by Loran Friedrich in partial fulfillment of the requirements for the degree of Doctor of Philosophy

Dr. M. J. Brett

Dr. S. K. Dew

Dr. R. Eadie

Dr. R. P. W. Lawson

Dr. S. Robinson

Dr. X. Sun

Dr. G. Tarr

December 16, 1997

To my wife and children

Thesis Abstract

The trend in the microelectronics industry to increase the number of devices per chip continues today from when it began nearly four decades ago. An increase in device density has generally been facilitated by the miniaturization of the device and interconnect features. As a result of the decrease in feature sizes, however, the fabrication of integrated circuits has become dependent upon the fundamental properties of the thin film material and film - substrate interactions. Thus, a new feature scale simulator to be used as a process design and development tool requires both fundamental modeling and process prediction capability.

GROFILMS is a two dimensional thin film process simulator developed to model the fundamental physical properties and characteristics of thin films. Based upon a line segment/nodal description of thin film microstructure, GROFILMS is capable of modeling diffusion, grain growth competition, anisotropic energetics, and ballistic shadowing. Phenomena such as substrate wetting, grain boundary grooving, and surface facetting are accurately represented. From a process development stand point, GROFILMS employs system scale parameters to simulate thin film processing (deposition and anneal) over topographical features such as trenches and vias.

This thesis describes the development of GROFILMS, verification of its fundamental modeling capabilities, and application to thin film processing. In particular, a discussion of the governing physical processes during basic and novel physical vapor deposition (PVD) techniques is presented. The GROFILMS simulator and experimental data are also used in an extensive study of the sputter reflow of copper. The study discusses the practical development of the reflow process for a particular system and determines the effects of the fundamental mechanisms originating from and dependent upon the microstructure of the deposited copper films. Specifically, it is found that the grain boundary density, wetting layer, copper thickness, deposition geometry and substrate topography have important implications for reflow process times and ultimate success.

Table of Contents

Abstract i

List of Tables v

List of Figures vi

List of Symbols ix

Chapter 1: Introduction 1

1.1 Overview of Interconnect Technology 3

1.1.1 Present metallization technology 3

1.1.2 Metallization Requirements 6

1.1.3 Interconnect Fabrication Challenges 6

1.2 Thin Film Process Simulators 10

1.2.1 Physical Simulators 10

1.2.2 Process Simulators 12

1.2.3 Grofilms 14

1.3 Thesis Goals 15

Chapter 2: Fundamental Thin Film Processes 17

2.1 Ballistic fluxes 17

2.2 Nucleation and coalescence 21

2.3 Microstructural and morphological development in thick films 22

2.4 Oblique angle deposition 27

2.5 Substrate wetting and grain boundary grooving 28

2.6 Diffusion and thin films 29

2.6.1 GROFILMS equilibrium model 30

2.6.2 GROFILMS kinetic model 32

2.7 Implementation 33

Chapter 3: GROFILMS Algorithms 35

3.1 Introduction 35

3.2 Line Segment Representation 35

3.3 GROFILMS Equilibrium Model 38

3.4 GROFILMS Kinetic Model 41

3.5 Energetics, chemical potentials, and surface advancement 42

3.5.1 Surface Nodes 42

3.5.2 Grain Boundary Pairs 47

3.5.3 Grain Boundary Grooving Node Pairs 48
3.5.4 Wetting Node Pair 50
3.5.5 Internal Triple Point Node Set 52
3.5.6 Interfacial Node Pairs and Interfacial Triple Point Node Set 57
3.6 Quasi-Three Dimensional Simulations 59
3.6.1 Quasi-three dimensional flux generation 59
3.6.2 Surface energetic calculations 60
3.7 Required Computer Resources 61
3.8 Summary 62

Chapter 4: Modeling the Fundamental Processes 63
4.1 Initial Stages of Thin Film Growth 63
4.2 Thin Film Surface Morphology 67
4.3 Thin Film Microstructure 71
4.4 Deposition Processes 74

Chapter 5: Copper Reflow for Damascene Processing 79
5.1 Cu Sputter Reflow Parameters. 79
5.1.1 Copper Reflow: Experiment and Simulation 83
5.1.2 GROFILMS analysis of the reflow parameters. 85
5.2 Substrate Considerations 92
5.2.1 Multiple feature sizes 92
5.2.2 Underlayer material 95
5.2.3 Copper reflow into via structures 96
5.3 Microstructural Effects on Copper Reflow 99
5.3.1 Analyzing microstructure effects using GROFILMS. 100
5.3.2 Grain boundary grooving and its effect on reflow times. 105
5.4 Summary 109

Chapter 6: Summary and Recommendations 110
6.1 Summary 110
6.1.1 GROFILMS model development 110
6.1.2 Fundamental physical properties and characteristics of thin films 110
6.1.3 Sputter Reflow of Copper 111
6.2 Recommendations for future projects 112

References 115

Appendix A: Chemical Vapour Deposition Simulation 131
A.1 Modeling the physical processes of chemical vapour deposition 131
A.2 Quasi-equilibrium CVD model 133
A.3 Kinetic model of CVD 134
A.3.1 Gas Phase Ballistic Transport 135
A.3.2 Chemisorption probabilities 136
A.4 Surface activated reaction kinetics 138
A.4.1 Adsorption kinetics 139
A.4.2 Desorption kinetics 140
A.5 Adatom and capillarity diffusion 141
A.6 Chemical reactions 141
A.7 Simulations of tungsten chemical vapour deposition 142

List of Tables

Table 1.1 - Intel microprocessor evolution from 1971 to 1997. 2

Table 1.2 - Metallization properties. 7

Table 3.1 - The GROFILMS node types used to represent a thin film. 37

Table 4.1 - Parameters used in generating the wetting examples of Figure 4.2. 65

Table 4.2 - Parameters used in generating the grain boundary grooving examples. 69

Table 4.3 - Grain sizes of a 100 nm thick film of various metals. 74

Table 4.4 - Grain sizes of a 100 nm thick film as simulated by GROFILMS. 74

Table 5.1 - Processing parameters available during copper reflow. 80

Table 5.2 - The physical parameters used in the GROFILMS simulations. 80

Table 5.3 - The pre-exponential diffusion coefficients. 81

Table 5.4 - Cu film profile properties for experiment and simulation. 85

Table A.1 - The fundamental processes during a typical CVD process. 132

Table A.2 - Reaction and process parameters for CVD. 143

List of Figures

1.1 Schematic diagram of multilevel metallization (MLM). 5

1.2 Schematic diagram illustrating the Damascene process. 9

2.1 Schematic diagram of a thin film deposited over topography. 18

2.2 Schematic diagram of the SIMSPUD model. 20

2.3 Polar plot of a SIMSPUD angular distribution. 21

2.4 Thin film structure zone models. 23

2.5 A schematic diagram of thin film deposition over topography. 24

2.6 A polar plot of surface free energy. 26

2.7 Schematic diagram of the columnar orientation. 28

2.8 Schematic diagrams of wetting and grain boundary grooving 30

3.1 Schematic diagram of GROFILMS. 36

3.2 Code listing of the nodal data structures. 38

3.3 Program organization of the GROFILMS simulation. 40

3.4 Diagram of the surface node parameters. 43

3.5 Geometry of an infinitesimal surface node movement. 44

3.6 Diagram of the grain boundary node pair. 47

3.7 Diagram of the grain boundary grooving node pair. 49

3.8 Diagram of the wetting node pair. 50

3.9 Diagram for the chemical potential and its derivatives. 53

3.10 Restricted triple point junction movement. 54

3.11 The geometry for triple point motion calculations. 56

3.12 Diagram of the interfacial triple node set. 58

3.13 Diagram of the cross-sectional views of trenches and vias. 59

3.14 Radius of curvature for out of plane surface curvature calculations. 62

4.1 Simulation of thin film nucleation. 64

4.2 Substrate wetting simulations. 65

4.3 Aluminum deposition over topography. 66

4.4 Verification of simulated wetting characteristics. 68

4.5 Grain boundary grooving simulations. 69

4.6 Verification of simulated grain boundary grooving characteristics. 70

4.7 The surface energetics as a function of surface orientation. 71

4.8 Various forms of crystal facetting. 71

4.9 GROFILMS simulation of a thin film with Zone I microstructure. 72

4.10 Simulations of temperature-dependent microstructures. 75

4.11 Tungsten deposition into a 1:1 aspect ratio trench. 76

4.12 Tantalum deposition into .35 micron 2:1 aspect ratio trench. 77

4.13 Unique microstructure of MgF_2 films grown by glancing angle deposition. 78

5.1 Schematic diagram of the pinhole experiment. 82

5.2 Flux distribution profile from pin-hole flux experiments (Intel system). 82

5.3 Flux distribution profiles as generated by the SIMSPUD simulator. 83

5.4 Copper deposition over 0.35 μm (aspect ratio 2:1) topography. 84

5.5 GROFILMS simulation of copper reflow. 85

5.6 Absolute reflow times versus the anneal temperature. 86

5.7 Normalized reflow times versus film thickness. 88

5.8 Simulations of Cu reflow in a long throw sputter system. 90

5.9 Simulations of Cu reflow in a short throw sputter system. 90

5.10 Bridging or capping of the trench. 91

5.11 Cu reflow into two trenches of different feature sizes (Intel system). 93

5.12 Cu reflow into two trenches of different feature sizes (short throw system). 94

5.13 Cu reflow into two trenches of different feature sizes (long throw system). 94

5.14 As-deposited Cu on a W underlayer. 96

5.15 Dewetting is of Cu on W underlayer. 97

5.16 Sputter reflow of Cu into 0.5 μm deep trench and via with aspect ratio 1:1. 98

5.17 Diagram of grain boundary grooving effects on local surface diffusion. 99

5.18 Cu via reflow without microstructure. 100

5.19 Experimental sputter reflow of copper in 1.5:1 aspect ratio trenches. 101

5.20 Simulation of Cu deposition over four parallel trenches. 102

5.21 Reflow simulations into four parallel trenches (no microstructure). 102

5.22 Reflow simulations with the grain boundary grooving phenomenon. 103

5.23 Reflow simulations with grain boundary grooving and facetting. 104

5.24 Original deposition profile without any microstructure. 106

5.25 As-deposited profile with five grain boundaries and completed reflow. 107

5.26 A plot of reflow times versus the number of grain boundaries. 108

5.27 Transmission electron micrograph of as deposited Cu. 109

A.1 Schematic diagram of basic CVD processes. 132

A.2 Tungsten PVD and CVD simulations. 134

A.3 W deposition rate dependence upon H_2 pressure. 143

A.4 W deposition rate dependence upon WF_6 pressure. 144

List of Symbols

GROFILMS	-	*GR*ain *O*riented *FIL*m *M*icrostructure *S*imulator
SIMBAD	-	*SIM*ulation by *BA*llistic *D*eposition
SIMSPUD	-	*SIM*ulation of *SPU*tter *D*istributions
IC	-	Integrated Circuit
PVD	-	Physical vapour deposition
CVD	-	Chemical vapour deposition
SIA	-	Semiconductor Industry Association
EM	-	Electromigration
MLM	-	Multilevel metallization
ILD	-	Interlayer dielectric
CMP	-	Chemical mechanical polish
MBE	-	Molecular beam epitaxy
t_s	-	film thickness on sidewall of trench
t_t	-	film thickness on top surface
t_b	-	film thickness on bottom of trench/via
$\sigma,\sigma(E),\sigma_0$	-	collision cross section, energy dependent and at $E=E_0$
E,E_0	-	sputtered particle energy, E_0 = 1eV
λ_m	-	mean free path
kT	-	thermal energy
p	-	gas pressure
T_S	-	substrate temperature
T_M	-	melting temperature
ϕ_c	-	columnar orientation
θ_f	-	angle of incoming flux
θ_Y	-	contact (wetting) angle

σ_{sv}, σ_{sb}, σ_{fv}, σ_{gb}	-	interfacial surface tensions
γ_{sv}, γ_{sf}, γ_{fv}, γ_{gb}	-	interfacial surface energetics
θ_g	-	equilibrium grooving angle
D, D_g	-	diffusion coefficients
Γ	-	jump frequency.
β	-	jump distance
ΔG	-	free energy change
A_{sv}, A_{fv}, A_{gb}, A_{fs}	-	interfacial areas
F_v	-	volume free energy
V	-	volume
J, J_g	-	diffusive flux
Ω	-	atomic volume
ν	-	surface concentration
μ, μ_0, μ_1, μ_2	-	chemical potentials
D_0, D_{g0}	-	pre-exponential coefficients
E_a, E_{ga}	-	diffusion activation energies
κ, κ_A, κ_B	-	surface curvatures
θ	-	angle of surface normal for surface energetic dependence
ID	-	algorithmic grain identification number
V_C	-	cached volume
α_i	-	angle of surface normal of line segment i
δ_i	-	length of line segment i
b, b_i	-	lengths along line between next and previous nodes
y	-	perpendicular distance between moving node and line between next and previous nodes
d	-	distance moved by a node

$\boldsymbol{R}, R$	-	motion vector, and distance of triple point
Φ	-	angle of motion vector with horizontal
S	-	surface node
G	-	grain node set
T	-	triple point node set
IT	-	interfacial triple point node set
Sub	-	substrate node
GbG	-	grain boundary grooving node set
W	-	wetting node set
x_{2D}, y_{2D}	-	particle position mapped onto two dimensions
ρ, ϕ, z	-	particle position in three dimensions
Δ	-	1 μm surface depth into the simulation plane
ρ_q	-	radius of curvature for in-plane surface
κ_q	-	curvature of out of plane surface
$P(A)$	-	pressure of gas A
R_i, R_d, R_r	-	adsorption, desorption and limiting reaction rates
s	-	sticking coefficient
w	-	particle weighting
I, I_o	-	impingement rate and normalization factor
ν, k	-	rate and rate constant
*	-	empty adsorption site on surface
c, p	-	gas concentration and pressure
θ_A	-	surface coverage of A

Chapter 1 Introduction

The semiconductor industry has become one of the most influential in our history as it is the nexus between the industrial and the information ages. The major driving forces behind the success of the semiconductor industry are the technological innovations leading to lower cost electronics [1] [2].

To achieve lower cost electronics, the semiconductor industry has relied upon large scale integration of devices onto single chips. The development of integrated circuits (IC) can be traced back to 1958 when the number of components were less than 10 and operating speeds were considerably less than a megahertz. Today, an Intel Pentium processor holds as many as 7 500 000 transistors per chip and can run at over 200 MHz. Table 1.1 details the evolution of Intel product technology [3]. While an increase in device density has lead to an increase in chip speed and thus overall performance, it is the lower cost components that have primarily driven the industry.

The increase in time of the number of devices per chip is referred to as Moore's Law. Originally, Moore's Law predicted a doubling of the number of devices per chip every year. This rate has slowed to doubling every 18 months and now it is more reasonable to assume a doubling every two years. Industry predictions state by the year 2011 there will be microprocessors with 1 billion transistors [4] operating at 10 GHz [5].

The drive to increase the number of devices per chip has motivated innovative research and development in material science, IC fabrication and circuit design. Of particular importance to this thesis are the fabrication considerations arising from the decrease in feature sizes of the on-chip devices and device interconnections. The physical dimensions have decreased in size to allow for the production of the high device density ICs. Feature sizes have decreased from 10 μm in 1971 to 0.35 μm today in the popular Intel processors (see Table 1.1 for details.). Features 0.25 μm in size will be in production soon, followed by 0.18 μm technology in the near future [5].

Table 1.1: Intel microprocessor evolution from 1971 to 1997 [3]

Year	Processor	Number of Components	Minimum Feature Size (μm), Technology	Chip Frequency (MHz)
1971	i4004	2300	10 (PMOS)	0.108
1972	i8008	3500	10 (PMOS)	0.2
1974	i8080	6000	6 (PMOS)	2
1976	i8085	6500	3 (NMOS, HMOS)	5
1978	i8086	29 000	3 (NMOS, CMOS)	5 - 10
1982	i80286	134 000	1.5 (HMOS)	6 - 12
1985	i80386	275 000	1.5, 1.0 (CMOS)	16 - 33
1991	i80486	1 200 000	1, 0.8, 0.6(CMOS)	20 - 50
1993	Pentium	3 300 000	0.6 (biCMOS), 0.35 (CMOS)	75 - 233
1995	Pentium Pro	5 500 000	0.6 (biCMOS) 0.35 (CMOS)	120 - 200
1997	Pentium II	7 500 000	0.35 (biCMOS)	300+

In the past, the trend to decrease the dimensions of the devices has resulted in fabrication obstacles surmounted by innovative techniques in process and materials development. As an example, optical lithography processes (a process used in the patterning of on-chip circuitry) have extended their capabilities by using novel mask designs and photoresists, and decreasing the light source wavelengths [6] [7].

Metallization (the process of supplying conduction lines by thin film deposition of metals) has been greatly affected by miniaturization of the features as the semiconductor technologies move to ultra large scale integration (ULSI) (greater than 10^7 components per chip). Processing has evolved from rather simple sputtering into elaborate techniques involving source-geometry adjustments, collimation, feature-shape adjustments, temperature-controlled processing, ionized sputtering and bias sputtering.

Metallization materials have also evolved from simple materials such as aluminum (Al) on silicon (Si) to aluminum alloys used in conjunction with silicides and refractory

metal diffusion barrier layers [9]. Alternative metals such as copper (Cu) are also used in select processing [8].

Extensive processing and materials research is required to develop the reliable fabrication processes of sub-0.5 μm metallization. A successful tool used to enhance research has been computer simulation. Simulations have been used to aid in process development [10], process control [11], equipment design [12] and device diagnostics [13].

As component miniaturization continues, new technologies must be developed to overcome the inevitable obstacles. The research tools must likewise evolve with the technology. Thus, thin film process simulators must continue to accurately and consistently make processing predictions. However, present research requires the simulation tool to incorporate the fundamental physical phenomena that have begun to significantly determine processing results.

This thesis will describe the motivation behind, and the development of, a thin film process simulator called GROFILMS (*GR*ain *O*riented *FIL*m *M*icrostructure *S*imulator) [14]. GROFILMS simulates the growth and processing of thin films while considering the microscopic fundamental physical phenomena that occur. The simulation results are macroscopic representations of a thin film's morphology and microstructure (on the scale of micrometers). Primary application of GROFILMS is in the metallization procedures of the interconnect technology of integrated circuits. However, GROFILMS can be applied to processes where thin film deposition is required or studied.

1.1 Overview of Interconnect Technology

Semiconductor devices require conducting materials to provide gate contacts, metal-to-silicon contacts, interconnects between devices and bonding pads for final assembly. Integrated circuit (IC) interconnects are the microscopic wiring of the chip that enable the propagation of electrical signals between on-chip devices, and provide power and external communications. The process of metallization is the fabrication procedure providing this network of conduction lines and interconnects for ICs.

1.1.1 Present metallization technology

Silicon dioxide (SiO_2) is regularly used as the interconnect dielectric material. SiO_2

has a moderately low dielectric constant of 3.9, is a good electrical insulator and is chemically inert [2]. This property, combined with its ease of deposition, patternability and compatibility with silicon technology, make SiO_2 an excellent insulating material for use in silicon microelectronics.

Aluminum (Al) and its various alloys have traditionally been used as the primary metallization metal [15]. This is because physical vapour deposition (PVD) processing of low resistivity Al (2.7 μΩ-cm bulk) is compatible with Si-based integrated circuit manufacturing, i.e. low stress Al films are easily sputtered or evaporated.

Drawbacks of Al/Si technology begin as feature sizes decrease. Due to the high solubility of Si in Al, interdiffusion at Al - Si contact interfaces can occur during processing at moderately high temperatures [16]. The interdiffusion can cause the Si to dissolve into the Al creating a void. Al atoms move into the void forming a spike into the device region. Reliability failures due to this phenomenon can be avoided by the use of barrier layers at the Al/Si junction. Al alloys were first employed to further extend the viability of Al-based metallization. The addition of 1.0% Si saturates the Al, eliminates the driving force for dissolution and suppresses junction spiking. Eventually, new barrier layer materials were required as metal silicide layers do not always form stable contacts [9]. Examples of common barrier layers include titanium (Ti), titanium nitride (TiN), and stuffed intermetallic alloys such as titanium-tungsten with or without nitride formation at the grain boundaries (a stuffing effect) TiW(N).

The second major drawback of Al/Si technology arising from the increased current densities and the low melting point of Al is the susceptibility to electromigration (EM) failures. EM is the mass transport of the conductor material under the influence of high current density. EM results as a momentum transfer occurs during interactions between conductor atoms and conductor electrons. The mass transport leads to a divergence in atom flux causing voids and open circuits and interconnect failures. Relationships exist between EM susceptibility, the metal film texture and the number and type of grain boundaries [17] [18].

EM becomes a serious problem as miniaturization and high density integration continue to decrease the metallization line widths and increase current densities. Copper (Cu) is added to Al to form Al-Cu alloys to increase susceptibility to EM failure. The Cu segregates to the grain boundaries and lowers the effective rate of grain boundary diffusion with-

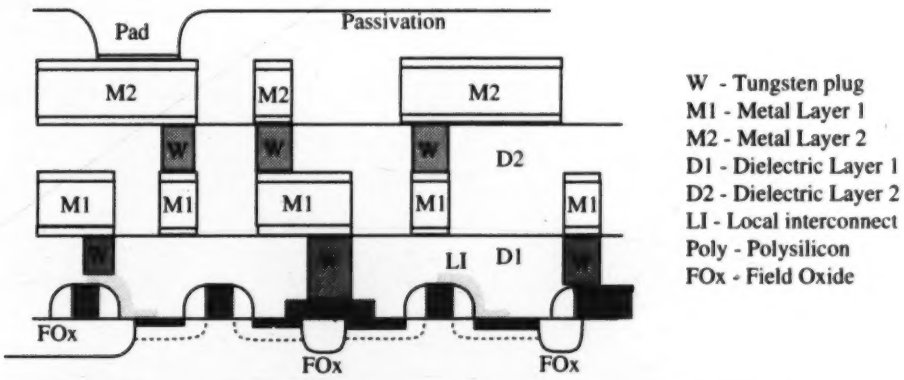

Figure 1.1 Multilevel metallization (MLM) schematic diagram illustrating an integrated device with three levels of interlayer oxides and metal lines.

in the alloy. There is thus an increase in resistance to EM [19]. Maximum resistance to EM is achieved with 4% Cu [16].

The use of Al-Cu alloys as the interconnect material results in trade-offs with processing techniques and metallization properties. As Cu does not easily form a volatile species, difficulties with dry etch processes exist. Increased corrosion rates due to the presence of Cu requires encapsulation of the interconnect lines. The line resistivity of the alloys also increases over that of pure Al. These problems restrict the amount of Cu in the alloy to less than 2%, however, Al-0.5% Cu is generally used to increase the EM reliability of integrated circuit interconnections.

New and innovative circuit layout designs were necessary to reduce delays due to capacitvie coupling of conduction lines and simultaneously increase the packing density of the devices. To this end, multilevel metallization (MLM) design schemes were employed (see Figure 1.1) [20]. The MLM design minimizes interconnect distances and reduces signal transmission delays. IC operating speed is thus enhanced by stacking metallization layers one on top of the other. MLM structures also utilize the vertical dimension permitting increased device density.

The use of MLM, however, tends to leave topographical features with high aspect ratios. These features are to be filled with the metallization material. Consequently, feature miniaturization and design geometry of MLM schemes significantly affect the development of the deposition processes required for successful metallization. For example, uni-

formity of the metal fill is a critical issue as feature dimensions decrease. The sputter deposition of Al is often inadequate for filling vias and forming reliable contacts. Tungsten (W) chemical vapour deposition (CVD) is being used as an alternative contact and via fill metallization [21]. W CVD can be selectively deposited. Good coverage in achieved within high aspect ratio vias. The increased resistance-capacitance time delays which result from the higher resistance of W (5.65 μΩ-cm bulk resistance; higher than 10 μΩ-cm for W CVD thin films [21]) may, however, significantly reduce device performance.

1.1.2 Metallization Requirements

The ever-present trend of device and feature miniaturization is motivated by the demand for increased circuit performance and packing density of devices on a chip. Interconnect technology must overcome major barriers in order to achieve higher speed, higher density circuits [20].

Challenges in interconnect technology include circuit layouts, substrate geometry, and fabrication. Circuit designs are consider the decreasing interconnect separations and high frequency operation of the circuits. Increased RC time delays impose limitations on the circuit layouts. Also, geometry designs and the fabrication processes are important issues as the interconnect dimensions continue to scale. Dielectric deposition and planarization and reliable metal deposition are more difficult.

The properties of the metallization metals are crucial to the development of the interconnect technology and fabrication processes. As features sizes continue to decrease, the requirements of the interconnect metal become increasingly rigorous. The metal must be reliably deposited into increasingly complex topographies; it must handle the higher current densities resulting from decreasing conductive cross sectional areas; and it must remain electrically and structurally stable. A list of the metallization requirements is summarized in Table 1.2 and is a starting point for the evaluation of a metallization material.

1.1.3 Interconnect Fabrication Challenges

Aluminum-based metallization is becoming the primary limiting factor in chip performance. This is due to the reliability issues associated with the stringent requirements of

Table 1.2: Metallization properties required by integrated circuit interconnect technology.

Metallization Property	Issue
Low electrical resistivity	Performance
High electromigration resistance	Reliability
Resistance to stress-induced voiding	Reliability
Oxidization / corrosion resistance	Processing / Reliability
Thermal stability	Processing / Reliability
Silicon process compatibility	Processing
Good adhesion to barrier layer or dielectric	Processing
Ease of deposition and patterning	Processing
Low production cost / high yield	Manufacturing

present MLM schemes. Thus, there is an ongoing research effort dedicated to the development of alternatives to present metallizaiton techniques and materials. Every year, the Semiconductor Industry Association (SIA), which represents a compilation of various members of the semiconductor industry and academia, releases their National Technology Roadmap for Semiconductors (NTRS). The roadmap was presented at the1997 International Conference on Metallurgical Coatings and Thin Films (ICMCTF) in San Diego, CA [22] and covered the many areas of IC fabrication technologies.

Predictions from the SIA metallization roadmap include the following. Metallization will be composed of 2100 meters of interconnect lines per chip by the year 2000. Concurrently, the feature size will shrink to 0.18 μm with aspect ratios up to 3.5 : 1 for logic devices and 6.2 : 1 for DRAM (currently, 0.35 μm features are employed). It is also predicted that the number of levels used in the MLM scheme will be greater than six; the present technology employs 5 levels of metallization (Intel's Pentium processors). The SIA roadmap indicates that interconnect metallization research will be focused on identifying appropriate materials, understanding their properties, and developing the fabrication techniques required for reliable processing.

The search for alternate interconnect metals has included copper (Cu), silver (Ag) and gold (Au). Despite some limitations, Cu is a likely candidate as a replacement metallization

material. Cu has low electrical resistivity (1.67 μΩ-cm) and the use of Cu with insulators with low dielectric constants will be advantageous in reducing the number of metallization levels required. Furthermore, Cu has a higher melting temperature, and substantially higher resistance to EM failure [8] [23]. The use of copper thus enhances the electrical properties of IC's, and should yield significant performance gains. The only metal with lower resistivity than Cu is Ag (1.59 μΩ-cm bulk resistivity) which tends to be reactive and more susceptible to EM failures and is therefore unsuitable.

Recently, IBM announced a new process technology called CMOS 7S [24]. This is the first production technology to use copper metallization with six layers of metal on a chip. The copper process was developed through a close collaboration between IBM's Research and Microelectronics divisions.

Research involving Cu as the interconnect metal is focused on physical vapour deposition (PVD), chemical vapour deposition (CVD) [25] [26] [27] and electrochemical deposition [28] [29] techniques. The traditional means of depositing metals for global metallization is by sputtering (a PVD method). Cu has a high sputter yield and sputter deposits very well. Also, conversion from Al to Cu sputtering would not require significant retooling. However, patterning of Cu is difficult. The conventional dry etching processes are possible but require high temperatures (250°C) which makes it difficult to find stable mask material [30]. Dry etch processes most likely will not be implemented in production. Wet etching may be the starting point for Cu patterning. Due to its isotropic nature, however, wet etching will be limited to the wider interconnection lines [31].

Before widespread use of Cu is viable, the capability of high aspect ratio patterning of Cu interconnects must be possible. This may be achieved by damascene processing [32] [33] [34] which can be used to generate the high aspect ratio inlaid Cu wires and paths needed for the interconnect metallization. The first step in damascene processing, as shown schematically in Figure 1.2 a), is to pattern the interlayer dielectric (ILD). Normally a barrier or adhesion layer is required and this is deposited next [35]. Sputtered or CVD Cu is then used to fill the patterned substrate. Completion of this step is shown in Figure 1.2 b). The excess Cu is removed via a chemical mechanical polish (CMP) leaving the features filled and the surface planarized (Figure 1.2 c)).

One of the key challenges of damascene processing is to completely and reliably fill

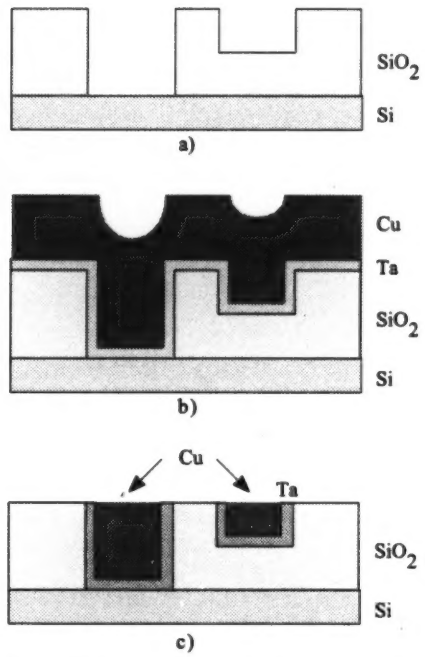

Figure 1.2 Schematic diagram illustrating the Damascene process for filling the features of a MLM structure. In frame a), the interconnect vias and lines are patterned into the interlayer dielectric (SiO_2). This is followed by the deposition of the barrier layer (Ta) and the interconnect metal (Cu) as detailed in b). The final step, c), is the removal of excess metal by chemical mechanical polish (CMP).

the topography. This is especially difficult for dual damascene which also has a via hole to fill at the bottom of the trench. Reliable filling is less of an issue for nearly conformal deposition processes such as CVD or electrochemical deposition, but very challenging for the more popular PVD methods.

Whichever interconnect metallization process is ultimately used, it will be required to reliably fill the extreme feature topographies related with the future MLM schemes. Under conditions of extreme topography, the fundamental material properties become much more important and will dictate process development. Furthermore, the properties of the deposited films, such as microstructure and surface roughness, can also affect device performance or post-processing. Therefore, it is important to understand the physical nature of the materials and how processing procedures can be developed to optimize performance, yield and reliability. Incorporation of the fundamental physics into a process model enables

these concerns to be addressed via simulation studies.

1.2 Thin Film Process Simulators

Process simulations are becoming more popular as the cost of performing experiments rises with the introduction of new technologies. Concurrently, cost of computation has decreased substantially. As well, greater demands are placed upon the physical models, their accuracy and the efficiency of the implemented numerical algorithms.

As a result of the decrease in feature sizes, the fabrication of integrated circuits, particularly metallization, has become dependent upon the fundamental properties of the thin film material and film - substrate interactions. Thus, a new feature scale simulator to be used as a process design and development tool requires both fundamental modeling and process prediction capability. The GROFILMS simulator described in this thesis is a new thin film process simulator that incorporates the fundamental physical properties of the materials and the thin film mechanisms that dominate.

The following paragraphs describe the types of thin film process simulators that presently exist. These simulators generally fall into one of two categories. They are either physical simulators, modeling the fundamental microscopic material properties, or they are macroscopic process simulators.

1.21 Physical Simulators

The physical simulations and the models upon which they are based are very important to materials science as they provide an understanding of the fundamental thin film properties and physical mechanisms. Numerical simulations used in the research into the physical properties of thin films incorporate the fundamental theories and processes of thin film growth. For example, nucleation of heterogeneous thin films is a critical step in the deposition of materials. A simulation study of the growth mechanisms and the resulting atomic structure at the initial stages of film growth provides insight into the governing microscopic processes that will determine the type and structure of the resulting thin film [37]. Another simulation study of nucleation reveals the dominating mechanism during nucleation and film growth as either surface migration or particle impingement depending upon adatom surface coverage [38].

The type of microstructural development of a thin film is governed by one or more dominating physical processes as determined by the deposition conditions and material properties. Thin film microstructures have been examined using Monte Carlo simulations [39] [40]. In these studies, the microstructure of the growing film is governed by the grain boundary movement coupled with a propagating front serving as an advancing film surface. The simulations predict columnar microstructures resulting when the columns reach a limiting size controlled by capillarity-driven grain boundary motion. Anisotropic interfacial energetics are required to examine the abnormal grain growth behaviours that can exist.

Columnar growth of amorphous thin films is shown to occur during sputter deposition [41] [42]. In these models, incident fluxes approach the surfaces from all angles and result in shadowing due to surface morphology. Simulating the shadowing phenomenon coupled with surface diffusion gives results that reproduce the well-known features of columnar growth while providing support for the concept of growth competition between the columns. Another model for thin solid film microstructural development predicts columnar orientation and suggests a relationship between column width and diffusion parameters [43]. This model also indicates the importance of adatom mobility in determining columnar formation.

Numerical simulations can target specific processes and determine their contribution under specified conditions. Fiber texture formation was shown to result from a bias in surface diffusion and anisotropic adsorption energies [44]. The diffusion and adsorption mechanisms were isolated from the other suspected causes of fiber texture such as preferential resputtering and self-shadowing. Simulation results also indicate that void formation was induced by low surface diffusion and high deposition rate.

The deposition systems and the processing parameters will affect the properties of a thin film. For example, the ballistic deposition and aggregation of material typical of PVD processing will moderate the microstructure. Ballistic aggregation models, based upon mean-field, continuum treatment [45] and direct numerical simulation [46] were developed. These models were used to explain columnar microstructure and columnar orientation due to oblique angle incident flux. Another example is the growth of epitaxial films during molecular beam epitaxy (MBE) and CVD. By examining the limiting regimes of two methods of simulation, a comparison between Monte Carlo and molecular dynamics

simulations gives insight into the dominating growth mechanisms [47].

Polycrystalline solids are the focus of many simulation studies. The physics of grain boundaries, for example, has been extensively investigated by numerical methods. It is known that the mobility of grain boundaries is a dominating mechanism for grain growth in polycrystalline solids. Simulation studies reveal the distribution and type of grain boundaries will influence grain growth characteristics in solids [48] [49]. Another fundamental model calculates the surface and grain boundary structure and energetics by using specific embedded atom potentials [50].

The above simulations incorporate models of the microscale processes associated with the fundamental physical characteristics of thin film materials. For example, interatomic potentials are extensively used for atomistic and molecular dynamics simulations [37] [47] [50] [51]. Calculating static energetics to describe the material properties is another example of a model upon which simulations are based. While the results from most fundamental physical simulations are generally microscopic (on the atomic scale), the results of simulations based upon energetics are used to examine the larger bulk properties of materials [43] [44] [48] [49]. Finally, some fundamental models are based upon solving the kinetic equations that describe the dynamics involved. The simulation studies usually discuss the physical problems in terms of rates [52].

Generally, the results from the fundamental physical simulations do not produce macroscopic predictions (on the feature scale) nor are topographies considered. The input parameters are fundamental and do not describe a macroscopic system (on the scale of the deposition chamber). Thus, these simulations are not suitable for use as process optimization or development tools where changes in system or substrate parameters are used to determine film property changes. For example, macroscopic process results from an atomistic model would require considerably more computational power than is feasible for a present desktop workstation [65].

1.2.2 Process Simulators

Process simulators are developed as tools for the process engineer and encompass all of the various steps involved in the fabrication of integrated circuits: isolation, implantation, diffusion and anneals, deposition, etching and lithography. The advantages to the en-

gineer in having the simulation tool are significant. Time-consuming and often expensive design of experiments for process optimization can be facilitated by the use of prescriptive simulations (simulations that allow for the direct modification of input parameters describing the process and produce predictions of the processing results). The engineer can also gain a better understanding of the behaviour of the system under use.

Reactor-scale process simulators incorporate models of the dominating physical mechanisms on the macroscopic scale of the process tool. For example, a PVD reactor-scale simulator, SIMSPUD [54] is capable of modeling various PVD processes. SIMSPUD is a Monte Carlo sputter flux transport code that models a sputter process within the reactor. System geometry, gas pressures, input power, and material types are input parameters; surface profiles and feature scale distributions are simulation results.

The CVD reactor-scale simulation PHEONICS-CVD [55] involves fluid flow and heat transfer, incorporates plasma effects and includes gas phase and surface reactions. Deposition rates, thermal behaviour and system performance results describing the CVD system are provided.

Feature-scale models are employed to aid in the development of the deposition process. The process list that has been modeled is extensive. Simulations have been used to model thin film growth via PVD [36], CVD [36], low pressure CVD (LPCVD) [56] [57], plasma enhanced CVD (PECVD) [58] [59], thermal reflow [53], etching [61], lithography [62] and reactive ion etching [63], to name a few.

Simulations based upon feature-scale models generally produce surface profiles. The surface profile representation facilitates rapid and efficient simulations [61] [62]. Using this representation, however, neglects the microstructural information of the materials. Until recently, the absence of this information was inconsequential as large feature sizes were used.

Other simulations use an aggregate collection of particles (in particular the SIMBAD simulation [36]) to represent film surface and microstructure. The macroscopic aggregate representation, however, does not promote microscopic evaluation and calculation of the fundamental physical properties and characteristics of a thin film. Furthermore, accurate calculation of surface properties such as adatom or precursor concentrations for use in simulating CVD or electrochemical deposition techniques is difficult. There is no mechanism

in which to store surface data such as concentrations and impingment statistics. Finally, the aggregate model is intrinsically an equilibrium model. Simulating kinetic processes such as the chemical reactions during CVD are not possible or approximated by a single parameter (sticking coefficient) at best.

1.2.3 Grofilms

GROFILMS was designed and developed to be a thin film process simulator with the following criteria. The simulator should be based upon an effective model that is both physical and prescriptive. Simulations based on such a model will give predictions as to the future state of a system while considering the fundamental characteristics of the processes or mechanisms involved. System geometry and processing parameters should be adjustable inputs allowing for the study of or development of a process. Other characteristics of good models are (1) simplicity: the dimension or complexity of the model should be as small as possible yet consistent with the particular set of facts or system characteristics, (2) clarity: the model should be easily understood within the context of the language of the model, (3) bias-free: the model should provide the same results independent of user bias, and (4) tractability: computer models should not require more computational power than what is affordable [64].

This thesis will describe the development and application of the physically based thin film process simulator GROFILMS. The development of the GROFILMS simulator is driven by the needs of the process engineer designing processes in the sub-micron regime of ULSI processing. GROFILMS simulates thin film deposition via various PVD and CVD processes and post-processing such as annealing, while incorporating the fundamental physical phenomena that dominate. GROFILMS uses a two-dimensional line segment representation of the surface and microstructure of a thin film. Direct calculation of local properties such as surface free energies are used to model thin film growth processes from nucleation to surface facetting. Previous process simulators do not incorporate this level of detail regarding modeling of the physical mechanisms.

GROFILMS' results are macroscopic representations of a thin film's morphology and microstructure (on the scale of micrometers). The results facilitate easy interpretation of simulation experiments that vary the process parameters. Primary application of GROFILMS

is in the metallization procedures of the interconnect technology of integrated circuits (ICs). Application of GROFILMS to the study of the sputter reflow of copper in presented in this thesis.

1.3 Thesis Goals

As discussed above, models based upon the fundamental physical properties of the materials will be important tools for future semiconductor interconnect metallization process development. A successful process model will fulfil requirements on accuracy, tractability, reproducibility and predictability.

The primary goal of this thesis is to describe the development and use of GROFILMS, a fundamental physically-based thin film process simulator. Two versions of the GROFILMS simulator have evolved. The first version is based upon a quasi-equilibrium energetic model and was developed to perform rapid simulations of thin film growth. A second model involving a kinetic approach was developed in order to simulate the thin film growth processes by solving the relevant rate equations The kinetic model was developed in particular to solve the reaction rate equations of a CVD process and capillarity-driven surface diffusion during post-deposition annealing.

The thin film processes that are important in the GROFILMS model are outlined and discussed in Chapter 2. These processes include the ballistic impingement of fluxes, film nucleation, substrate wetting, surface diffusion and grain boundary migration. Texture formation and Thornton zone structures are discussed in terms of material and process parameters. Furthermore, the surface phenomena of facetting and grain boundary grooving are presented. The above listed processes are modeled by one or both of the GROFILMS simulation modules. Chapter 2 will discuss the fundamental physical description of the phenomena and the computational methods involved in the modeling.

The development of the GROFILMS algorithms will be discussed in Chapter 3. As originally developed by Dr. S. Dew, the GROFILMS simulator uses a line segment / nodal description of the film surface and microstructure. This representation of the film microstructure facilitates the calculation of film properties such as surface curvature, interfacial energetics and crystal surface orientation. Unique to this dissertation are the derivations of the energetic calculations, chemical potentials, and surface advancement are detailed and

presented in Chapter 3.

GROFILMS simulates many fundamental characteristics of thin films during film growth or post-deposition processing. In Chapter 4, the author tests the models on which GROFILMS is based and compares the results to theory and experiment. In particular, GROFILMS is required to demonstrate the effects on film microstructure due to varying deposition temperatures, grain boundary grooving and wetting characteristics over a range of possible interfacial energetics, surface facetting, ballistic self-shadowing of impinging flux, and deposition over topography. Validation of these results are necessary to ensure confidence in subsequent studies and in their conclusions.

Once convinced of the correctness of GROFILMS predictions, the application of the simulator to IC metallizaiton is presented in Chapter 5. A major effort of this thesis and the author is the application of GROFILMS to the sputter reflow of copper for interconnect metallization. The study consists of two sections; a fundamental study of the copper reflow process and a practical application of the simulator for the optimization of a specific copper reflow process. Experimental scanning electron micrographs (SEM) and transmission electron micrographs (TEM) of as-deposited and post-annealed Cu films were provided by Don Gardner at Intel Corporation in Santa Clara.

Chapter 6 summarizes the work comprising this dissertation. A discussion of future projects and recommendations for GROFILMS' research is also presented.

Chapter 2 Fundamental Thin Film Processes

The dominant physical mechanism governing the microstructure of thin films during deposition and post-deposition processing changes with deposition conditions and through the different stages of film growth (nucleation, coalescence, columnar/grain growth). The thermodynamic interfacial energetics determine substrate wetting, grain boundary grooving, facetting and capillarity diffusion. Thin film properties also depend upon incident flux distributions, substrate topographies and process temperatures. The following paragraphs discuss accepted theoretical models of physical phenomena, the processing conditions under which they contribute or dominate and the associated film properties. The theories are translated into numerical methods used by the two distinct GROFILMS models (quasi-equilibrium and kinetic) in Chapter 3.

2.1 Ballistic fluxes

Particle impingement from the vapour affects the properties of thin films deposited by physical vapour deposition (PVD) [66] and chemical vapour deposition (CVD) [67]. On the feature scale and for simple deposition processes, an impinging particle can be described by ballistic motion. Flux distributions describe the incident angle probabilities for the impinging particles. The system geometry and processing conditions will determine the flux distribution that arrives on the substrate and on the feature scale. The physical problems of determining the flux distribution is discussed shortly.

An inherent characteristic of ballistic fluxes is shadowing. Shadowing occurs when the high regions of the substrate topography receive the majority of flux while reducing that arriving at the low regions. The film's step coverage, which is the ratio of film thickness on the sidewalls of trenches or vias to that on the top surface, t_s/t_t (Figure 2.1), is directly affected by the shadowing. The bottom coverage is the ratio of film thickness on the bottom of features to that on the top surface, t_b/t_t (Figure 2.1) and is similarly determined by the flux shadowing. Two other properties of interest for metallization materials are the film's resistivity and reliability under operating conditions. Less dense or highly granular films within the substrate features can increase line resistance and reduce reliability due to in-

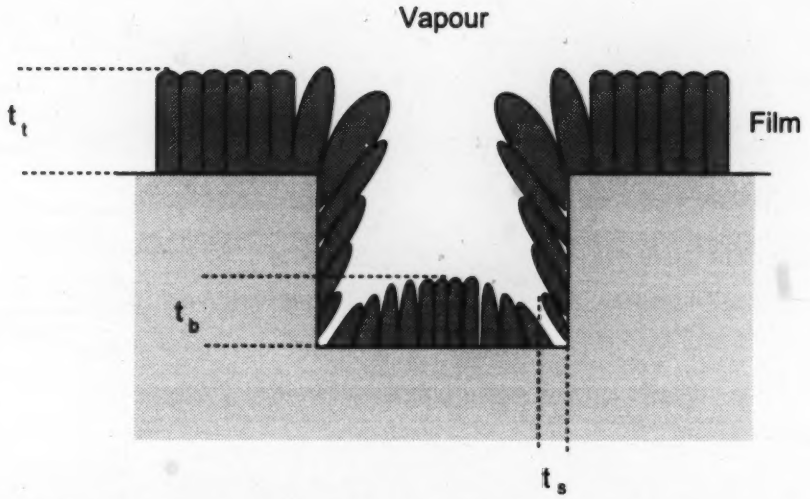

Figure 2.1 Schematic diagram of a thin film deposited over topography. The film thicknesses are labelled for the top surface: t_t, bottom of trench: t_b, and trench sidewall: t_s.

creased voiding or electromigration. Highly columnar, voided structures form due oblique fluxes arriving at the feature walls.

Gas phase collisions of the sputtered atoms within topographical features are not simulated by GROFILMS. This is as there is infrequent interaction between the particles due to the low pressures within the system. Likewise, the pressures of typical CVD processes do not facilitate vapour phase collisions of the precursor particles in the near vicinity of the topography. GROFILMS does, however, require the flux distribution determined by experiment or from the PVD flux transport code SIMSPUD.

SIMSPUD (*SIM*ulation of *SPU*tter *D*istributions) is a three dimensional Monte Carlo simulator that provides a detailed description of flux distributions within a PVD system [69]. SIMSPUD receives the geometry of the physical system, including the substrate - target positions and sizes, and the process conditions (gas pressures, target voltages, temperature and target erosion profiles) as input parameters [70]. Figure 2.2 is a schematic diagram detailing the SIMSPUD algorithms.

Particles are ejected from randomly chosen locations on the target while considering the erosion profile effects. The particle trajectory will depend upon the surface orientation and an emission angular distribution (either input from experimental results or a simple co-

sine distribution is used). During transport of the sputtered atom, elastic collisions are assumed to occur with the gas atoms. New sputtered atom trajectories are calculated using a hard sphere collision model. Collisional frequency is governed by an energy-dependent collision cross section, $\sigma(E)$. SIMSPUD uses a power law to describe $\sigma(E)$:

$$\sigma(E) = \sigma_0\left(\frac{E}{E_0}\right)^{-0.29} \quad \text{For } E > E_0 \tag{2.1}$$

Here, $E_0 = 1\text{eV}$ and $\sigma_0 = \sigma(E_0)$.

SIMSPUD calculates a mean free path, λ_m for a sputtered particle as:

$$\lambda_m = \frac{kT}{p\sigma} \tag{2.2}$$

where kT is the thermal energy of the gas and p is the gas pressure. Ejected particles are allowed to follow their trajectories of motion until they strike the substrate, chamber wall, or collimator or until a gas phase collision occurs. The distance traveled between collisions, λ, is defined by a Poisson distribution about λ_m and shown in Figure 2.2:

$$f_\lambda(\lambda)\mathrm{d}\lambda = \frac{\mathrm{d}\lambda}{\lambda_m}e^{-\lambda/\lambda_m}. \tag{2.3}$$

At the point of the collision, a new particle trajectory is calculated on the basis of the binary elastic hard-sphere collision. The scattering angle is

$$\alpha_{cm} = \pi - 2\,\mathrm{asin}\left(\frac{a}{d}\right) \tag{2.4}$$

where d is the maximum interaction radius between gas and sputtered particle ($d = r_s + r_g$) and a is the collision impact parameter. The sputtered atom will lose energy in the collision according to the relation:

$$\frac{E_{final}}{E_{initial}} = \frac{m^2 + m_g^2 - 2mm_g\left(1 - 2\left(\frac{a}{d}\right)^2\right)}{(m + m_g)^2} \tag{2.5}$$

Statistics are collected at the substrate thereby generating an angular distribution indicative of the flux across the substrate. The distributions can be used to determine unifor-

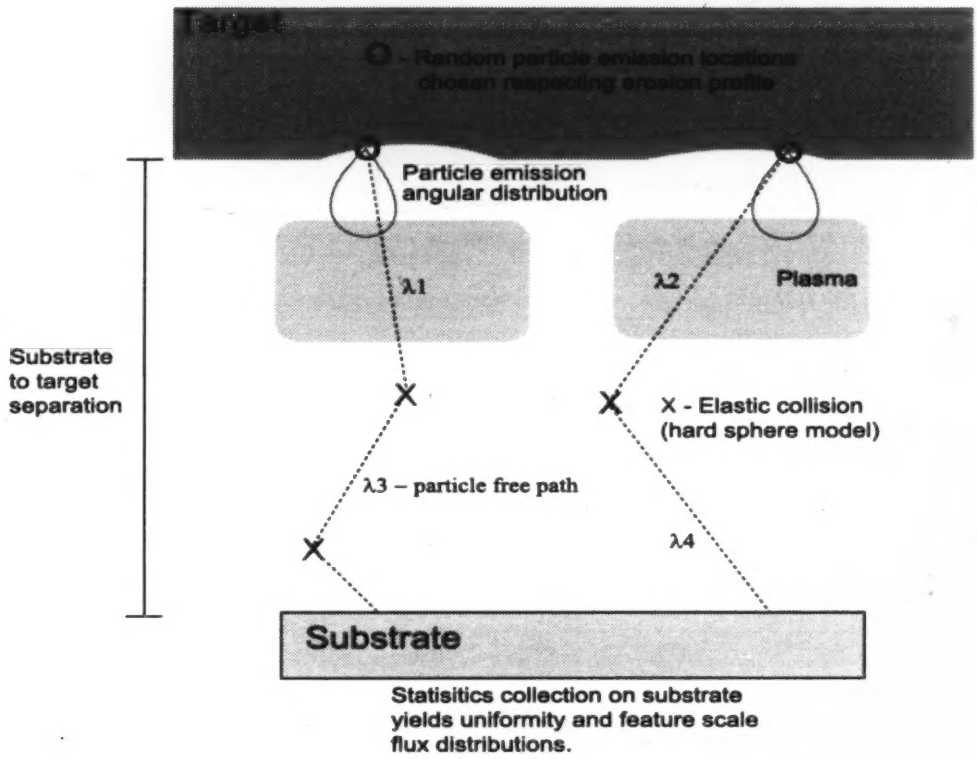

Figure 2.2 Schematic diagram of the SIMSPUD model of a sputter system. Shown are the erosion profile on the target, the particle emission distributions, flux transport, gas collisions and data collection at the substrate.

mity across the substrate or used as input for feature scale modelling. An example of SIMSPUD output simulating the sputtering of Cu in a 1 mTorr argon gas pressure and a target-to-substrate distance of 10 cm is presented in Figure 2.3. The data is presented in a polar plot with the probability of a particle arriving at a particular angle given by the radius at that angle. The flux impingement distribution is stored and is used as an input for the feature scale film growth simulator, GROFILMS or an alternate film growth model, SIMBAD [36].

To simulate the ballistic impingement of particle flux on the feature scale, GROFILMS generates particles and launches them from randomly chosen locations within the vapour. Each particle is given a linear trajectory predetermined from the angular distribution describing the incoming flux. Impact locations are found on the surface by following the par-

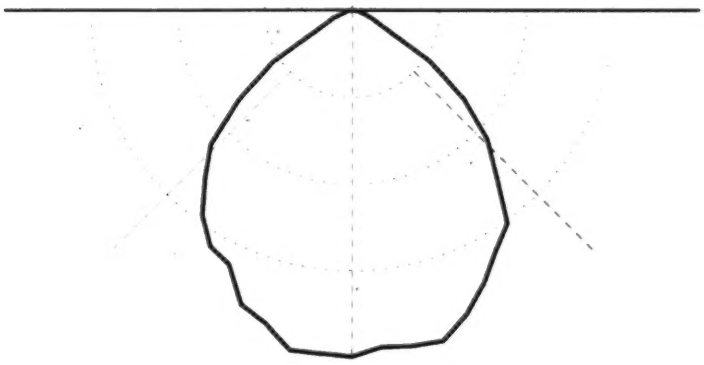

Figure 2.3 Polar plot of the angular distribution of incoming flux as generated by a SIMSPUD simulation of a Cu sputter system at 1 mTorr gas pressure and 10 cm target to substrate separation.

ticle's trajectory.

A particle has distinct definitions for the equilibrium and kinetic GROFILMS models. A particle in the equilibrium growth model represents a specific volume of material and is used to model the collective behaviour of a large number of atoms (ranging from 10^4 to 10^6). Within the kinetic GROFILMS model, particles are considered as counters used to obtain a statistical description of the flux impingement along the surface. Impingement rates and thus the number of incident particles are calculated across the surface.

2.2 Nucleation and coalescence

Film growth begins with the nucleation of the impinging vapour particles. Upon arrival onto a clean substrate, the particles may be reflected from the surface or they may physisorb (physically adsorb) to the surface. The particle in the physisorbed state is called an adatom and is mobile. The adatom will diffuse along the surface of the substrate until it nucleates (forms clusters with other adatoms), comes to rest on the substrate or film or re-evaporates. As the nuclei sizes increase, it becomes energetically more favourable for the nuclei to continue growing and the probability for re-evaporation decreases. The nucleated islands will grow according to the impingement rate of the particles (either from the vapour or through surface diffusion) and through coalescence (merging of nuclei to form an energetically more favorable larger nucleus).

The two GROFILMS models differ in handling the nucleation phenomenon. The equi-

librium model assumes the formation of the stable large nuclei or islands and immediately renders them for subsequent energetic calculations and graphical output. The assumption is valid as the particle in GROFILMS represents a large number of atoms (see p. 21). Further, it is known that metals form stable nuclei with very few atoms [71].

The nucleation process is, however, very much a non-equilibrium kinetic process. The GROFILMS kinetic model considers the various rate equations, including flux impingement rates, adatom diffusion over the substrate surface, and the distribution of critical and sub-critical nuclei due to condensation, evaporation and coalescence. The adatom diffusion is controlled by variation in adatom concentrations along the surface. The concentration will vary according to condensation and evaporation rates at the nuclei. The rate of change in the population of the nuclei depends upon the size distribution of the nuclei which in turn depends upon the number density of adatoms.

Nuclei will tend to coalesce into larger, more stable islands, thereby reducing the number of smaller nuclei. Voided regions form between the islands. These will eventually fill due to the increasing sizes of the islands rather than further nucleation. As the population of stable nuclei grows, adatom evaporation rates drop and the adatoms condense on the islands. Eventually there will be sufficiently large islands to be graphically rendered and used for energetic calculations by GROFILMS.

2.3 Microstructural and morphological development in thick films

The structural development of PVD films depends upon the physical and processing parameters during the deposition. As discussed above, the ballistic impingement of incident fluxes plays a role in determining film properties. Also important are the deposition temperature, substrate topography, material properties and processing conditions.

The microstructure of thin films can be highly porous and have a columnar or fibrous structure. Alternatively, the films can be dense, textured, and polycrystalline. The relationship between deposition conditions and the structure of thick (on the order of 100 μm) films was introduced by Movchan and Demchishin [72]. Their explanatory model (the MD model) describes the structure of evaporated thin films according to the ratio of deposition or substrate temperature, T_S, to the melting temperature of the material, T_M, and is presented

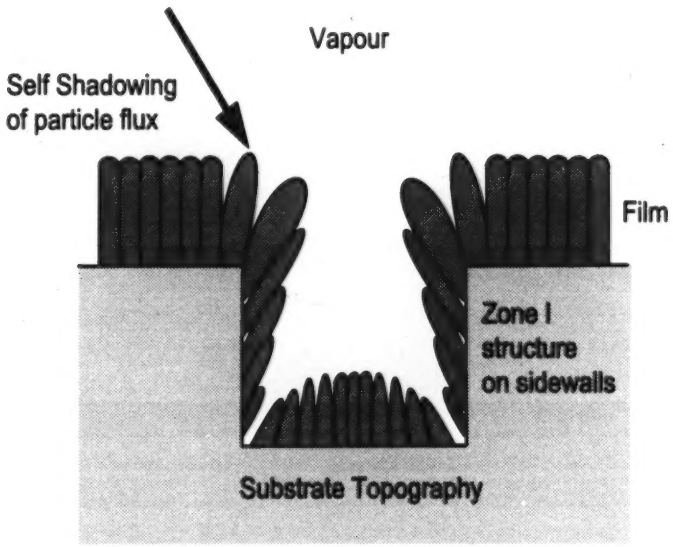

Figure 2.4 A schematic diagram of thin film deposition over topography shows the development of Zone I microstructure along the sidewalls of the trench. The process of self-shadowing (flux shadowed by columnar growth of the film) is displayed.

schematically in Figure 2.5 a).

Three structural zones were identified in the MD model. Zone I refers to the low temperature deposition; T_S/T_M ranges up to 0.3 for metals (0.26 for oxides). Under these conditions, there is very little or no surface diffusion to affect film properties during growth. The dominating mechanism dictating the evolution of the film structure during deposition is the shadowing of the ballistic fluxes. Self-shadowing (shadowing of the fluxes by the film structure rather than substrate topography as shown schematically in Figure 2.4) along with low diffusion forms a porous film comprised of isolated columns. The columns and the voids between them can vary widely in size.

Zone I structures can form within topographical features [74]. The shadowing mechanism dominates within substrate topography even under conditions of moderate surface diffusion. The film covering the sidewalls of trenches receives flux incident at oblique angles and will often display a Zone I structure with the columns oriented toward the direction of the incoming flux (see Figure 2.4). This is a concern for metallization as the less dense columnar structure along the sidewalls can cause reliability problems and an increase in the resistivity of the film.

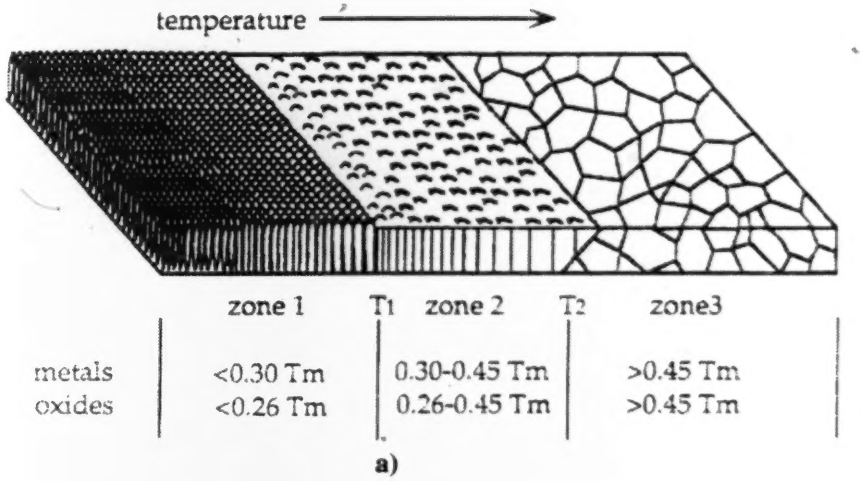

a)

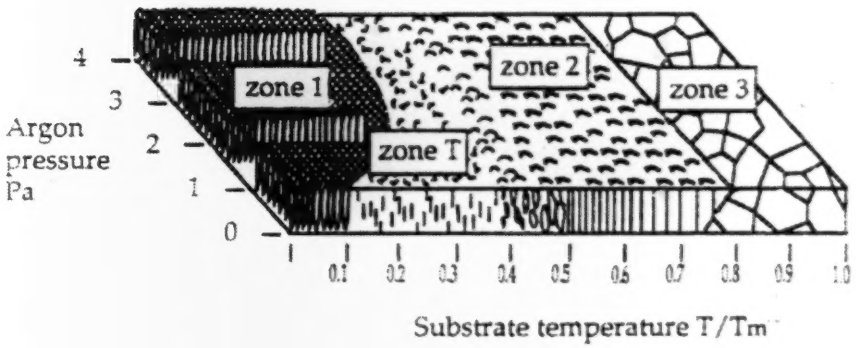

b)

Figure 2.5 a) The three-zone structure model developed by Movchan and Demchishin to describe the thick film microstructure deposited by evaporation and its relationship to the ratio of substrate temperature to the melting temperature of the film material. b) The revised structure zone model to include the effects of the sputtering gas pressure. (Figure used with the permission of R. N. Tait) [73]

The Zone II structure lies within the temperature ratio range of 0.3 to 0.45-0.5. At these temperatures, surface diffusion is significant and will dominate the formation of the film structure. Within this zone, a columnar structure exists with well defined boundaries. These boundaries are mobile and contribute to the evolution of the film texture. Interfacial surface energetics play an important role in forming the surface morphology as grain boundary grooves and, at elevated temperatures, facets appear. Furthermore, grain growth

competition is primarily controlled by surface diffusion and the mechanisms governed by interfacial energetics (such as grain boundary grooving and facetting).

Zone III structures occur during high temperature depositions. Here, bulk diffusion can occur and influence film texture and structure by recrystallization and the migration of mobile grain boundaries. The film is composed of large equiaxed grains that often exhibit a distinct preferential texture.

The MD structure zone model was subsequently revised by Thornton [74] to include the effects of ambient gas pressures during sputter deposition (see Figure 2.5 b)). Thornton introduced a new zone as a transition between zones I and II [75]. The new zone, called Zone T, is in the low pressure regime of sputter-deposited films. The structure of a Zone T film is influenced by greater surface mobility and thus less by shadowing effects. The film consists of fibrous grains, is much denser and the surface is smoother than Zone I films.

Energetic particle bombardment is one mechanism for the formation of the Zone T microstructure [76]. Bombardment energy is a function of bias potentials and to a strong degree the ambient gas pressure (higher pressures decreases average energy of the sputtered species through gas phase collisions). The thermal energy of the adatoms increases with bombardment energy. Thus, the Zone T structure becomes more prevalent at lower T_S/T_M as increased bombardment energy serves to densify the physical structure. To a certain degree, resputtering effects will occur with increased energies. Other film properties that are subject to change are increased defect creation affecting nucleation and adhesion, film morphology, and film stress [77].

An increase in ambient gas pressures is assumed to provide collisional scattering thus enhancing the oblique component of the particle flux. In this manner, the properties of a Zone I film structure can be extended to higher temperatures (reducing the size of Zone T) due to the increase in atomic shadowing and energy loss from the bombarding particles.

A final consideration to the development of thin film structure is chemically induced adatom mobility [76]. The adsorption/desorption characteristics of the vapour species can affect the mobility of adatoms through the possible complex surface chemical interactions. This phenomenon is more of a concern for plasma sputtering processes and the chemically active CVD processes. As yet, chemically induced structural influences are difficult to describe parametrically due to the complexity of the surface chemistry.

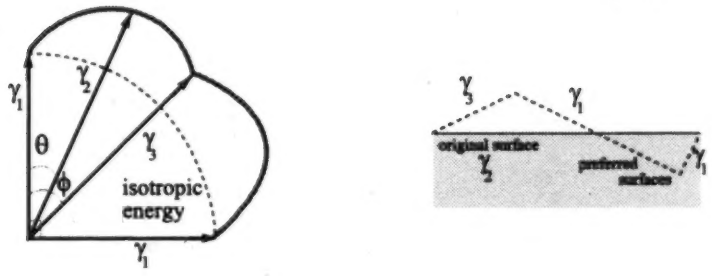

a) b)

Figure 2.6 a) A polar plot of the variation of the surface free energy with orientation produces cusps at angles corresponding to the facetted planes. b) The original flat surface with surface energy γ_2 is replaced by the preferred surface composed of an arrangement of facets which have in total more surface area than the original but with lower total free energy.

The texture of a film refers to the tendency for the film material to form preferred crystallographic orientations. A thin film's texture depends upon the deposition conditions [78] and is most prominent in zone II and zone III films. The texture will be determined by substrate-film interactions, nucleation, grain growth and competition and grain boundary migration. The competition between grains during Zone II film growth, and thus the resulting dominant film texture (if one exists), is governed by surface diffusion and the interfacial energetics of the contributing granular structure. Texture of a Zone III film is determined by both surface and bulk diffusion.

The interfacial surface energetics of each grain are determined by its crystal orientation, the surface type (grain boundary or surface) and local geometry. A grain's crystal orientation is determined during nucleation. GROFILMS assigns a crystal orientation to each grain as it nucleates. This orientation is chosen from a predefined probability distribution. The predefined distribution is used to describe the preferred orientation characteristic exhibited by some materials during nucleation.

It is the nature of some materials to expose crystal planes on their surfaces. The origin of this phenomenon, referred to as facetting, comes from the variation in the surface free energy with respect to the orientation of the crystal face. The lower energy planes are more favorable and will tend to grow preferentially during deposition (when surface diffusion

dominates) or will form during annealing. The anisotropic growth of grains will be a factor in determining film texture and morphology by affecting the growth between competing grains.

Equilibrium shapes for facetting of a crystal surface are described by a polar or Wulff plot [79] of the surface tension. Figure 2.6 shows an example of the variation of the surface energy with orientation and the formation of low energy planes which in fact may increase the total surface area though achieve a minimum energy.

As GROFILMS is a two-dimensional simulator and the crystal structure is variable in three dimensions, anisotropic surface tension variability is limited to a projection onto a specific crystal plane.

2.4 Oblique angle deposition

Very little adatom diffusion occurs during evaporation on low-temperature substrates. Thus the atoms generally stick where they land or move only very short distances. This type of behaviour results in a characteristic Zone I structure as discussed on p. 23.

Geometrical effects such as ballistic shadowing play an important role in the evolution of the film's structure. The dominant mechanism is the interception of the majority of the local vapour flux by the columnar structures which have grown slightly larger than their neighbours. These columns will grow at an accelerated rate and will eventually completely overshadow their neighbours. Through such competition many columns will be shadowed and eventually will no longer grow. The films end up being highly porous and composed of isolated columnar structures.

Films grown with oblique angles of incoming flux will grow columnar structures oriented toward the flux. Figure 2.7 demonstrates this phenomenon schematically. The formation of the columnar structures and their orientation toward the incoming flux is instrinsic to the GROFILMS' algorithms.

An experimentally derived empirical formula call the tangent rule [80] aids in predicting columnar orientation phenomena. The tangent rule relates the angle of the incoming flux, θ_f, to the orientation of the columns; ϕ_c:

$$2\tan\phi_c = \tan\theta_f \tag{2.6}$$

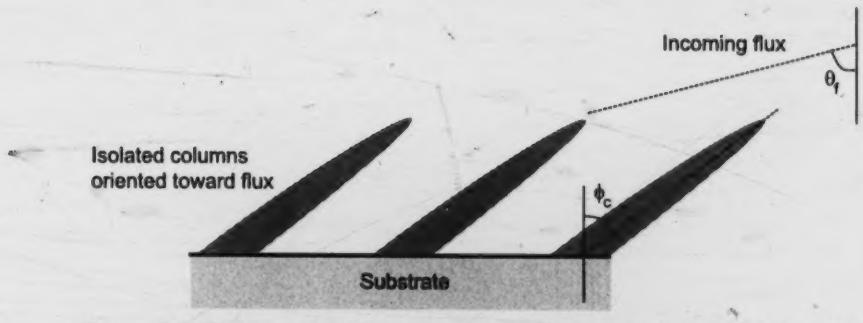

Figure 2.7 Schematic diagram of the columnar orientation toward the incoming flux that develops during oblique angle deposition.

Tait worked on improving the understanding of the angular relationships by providing expressions based on geometrical arguments [81]. His work describes column angle and film density as a function of deposition angle.

2.5 Substrate wetting and grain boundary grooving

Substrate wetting and grain boundary grooving are material phenomena governed by interfacial energetics. A material that covers a surface is said to wet it well; one that agglomerates or balls up and leaves much of the surface uncovered has poor wetting properties.

Historically, Young proposed a balancing of the horizontal surface tension forces to determine the contact angle, θ_Y and thus the degree of wetting [82]:

$$\cos\theta_Y = \frac{(\sigma_{sv} - \sigma_{sl})}{\sigma_{fv}}. \tag{2.7}$$

Here, the σ are the surface tension forces with the surfaces defined by the subscripts sv: substrate and vapour, sf: substrate and film, and fv: the film and the vapour.

The wetting phenomenon has since undergone more rigorous analysis and the contact angle is shown to be determined by the principle of free energy minimization [83]. Assuming isotropic interfacial energetics, the equilibrium condition of the system as shown in Figure 2.8 (a) is described by:

$$\gamma_{sv} = \gamma_{sf} + \gamma_{fv}\cos\theta_Y \tag{2.8}$$

The γ's are the free energy per unit surface area of the same surfaces defined above.

The parameter θ_Y in both equations is the wetting angle and it can vary from very high angles describing poor wetting to very low angles or good wetting, depending on the system.

Grain boundary grooving is a surface phenomenon and occurs where grain boundaries are exposed at the surface [85]. The morphology of polycrystalline thin films is affected by grooving where grain boundary energetics are significant enough to deform the surface and during processes where surface diffusion dominates. The magnitude of grooving is governed by the interaction between the surface and grain boundary tensions. Balancing the tensions as shown in Figure 2.8 (b) leads to the equilibrium condition:

$$\sigma_{gb} = 2\sigma_{fv}\cos\left(\frac{\theta_g}{2}\right) \tag{2.9}$$

where θ_g (as in Figure 2.8 b)) is the angle between contacting grains (grooving angle) and the σ's are the interfacial tensions between the film and vapour (fv) and the grain boundary (gb). In terms of free energy minimization, (2.9) is rewritten using γ's; the interfacial energetics:

$$\gamma_{gb} = 2\gamma_{fv}\cos\left(\frac{\theta_g}{2}\right) \tag{2.10}$$

Increased grain boundary grooving generally leads to rougher surfaces.

2.6 Diffusion and thin films

The diffusion phenomenon is plays an important role in materials research. The discussion of this phenomenon is limited to diffusion associated with the metallization processes of thin metal films: bulk diffusion, surface self-diffusion, adatom diffusion and grain boundary migration. The emphasis in the development of the GROFILMS simulator was placed on surface diffusion and grain boundary migration since these are dominant at the typical processing temperatures. Bulk diffusion in thin films is important only for specific materials and processing conditions (such as high temperature Al [84]). Adatom diffusion plays a very important role in CVD processes and is discussed in detail in Appendix A.

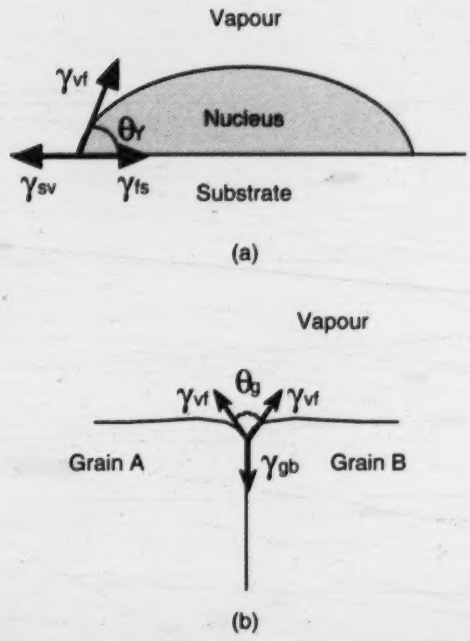

Figure 2.8 Schematic diagram illustrating (a) the wetting and (b) grain boundary grooving equilibrium angles that result from interaction of interfacial energetics. The vectors are the various interfacial tensions: *vf* - vapour/film, *sv* - substrate/vapour, *fs* - film/substrate, and *gb* - grain boundary.

2.6.1 GROFILMS equilibrium model

To simulate diffusion using an equilibrium energetics model, GROFILMS uses a characteristic diffusion length. The diffusion length is defined as the distance within which many particles would distribute themselves. In the GROFILMS simulation, a particle (representing the behaviour of many atoms) is allowed to diffuse from its impact point a distance according to this characteristic length. The growth model of GROFILMS is governed by lowering the total free energy of the system. Thus the location at which the particle will relax is one within the diffusion length that will result in the greatest energy minimization.

In determining the characteristic diffusion length of a material, one starts by solving the problem of determining where an atom will be at time *t* if it has a particular jump frequency and jump distance. In particular, the solution to the random-walk problem on a plane (two dimensional diffusion) gives the mean square distance an atom will diffuse in

time t is given as $4Dt$ [86]. The diffusion coefficient, D, depends upon the atom jump frequency, Γ, and jump distance, β, and is therefore material and temperature dependent:

$$D = \frac{1}{4}\Gamma\beta^2 \tag{2.11}$$

One can discuss the solution to the random-walk problem in terms of the characteristic diffusion length, $\lambda = 2\sqrt{Dt}$. The diffusion coefficient, D, retains its definition as outlined above. The time t, however, is defined to depend upon deposition parameters such as deposition rates and contamination levels. Thus, λ can be used to describe the diffusion characteristics during thin film deposition that are process and material specific.

Calculation of the surface and interfacial energetics is necessary to simulate diffusion using the equilibrium model. The free energy change, ΔG, of a thin film system is found to be related to the free energies of the surfaces and the free energy of the volume [71]. Equation (2.12) shows this relationship.

$$\Delta G = \gamma_{sv}A_{sv} + \gamma_{fv}A_{fv} + \gamma_{gb}A_{gb} + \gamma_{fs}A_{fs} + F_vV \tag{2.12}$$

The γ's are the interfacial energies of the surfaces as previously defined with the addition of grain boundaries *gb*. The *A*'s are the corresponding interfacial and surface areas. F_v is the free energy associated with the volume of material, *V*. To determine where the greatest energy minimization will occur due to the deposition of material, the derivative of the free energy change with volume, $\frac{d}{dV}\Delta G$, is calculated along the surface. From equation (2.12), the derivative is

$$\frac{d}{dV}\Delta G = \sum_S \frac{d}{dV}(\gamma_S A_S) + F_v. \tag{2.13}$$

In equation (2.13), the subscript S is used to denote the surfaces used in equation (2.12). The calculation of $\frac{d}{dV}\Delta G$ will depend upon the local geometries (A_S) and the local energetics (γ_S). As the GROFILMS simulator compares the values of $\frac{d}{dV}\Delta G$ along the surface, the constant free energy term associated with the volume, F_v, can be neglected. Chapter 3 discusses the algorithms formulated to solve equation (2.13) for various components of the thin film microstructure.

2.6.2 GROFILMS kinetic model

To simulate surface self-diffusion, grain boundary migration and adatom diffusion (see Appendix A for a complete discussion on adatom diffusion), the GROFILMS kinetic model solves diffusive current equations using finite difference analysis. The diffusive flux is calculated using the Nernst - Einstein equation [87]:

$$\vec{J} = \frac{\Omega \nu}{kT} \bar{D} \cdot \nabla \mu \tag{2.14}$$

where Ω is the atomic volume, the term ν is the surface concentration and kT has its usual meaning of thermal energy. D is the effective surface diffusivity tensor and μ is the chemical potential. Considering a simple one-dimensional, isotropic system, the diffusivity, D, is dependent upon an activation energy, E_a, a pre-exponential factor, D_0, and temperature, T, in a typical Arrhenius manner:

$$D = D_0 \exp\left(-\frac{E_a}{kT}\right). \tag{2.15}$$

The surface diffusion currents, J, are driven by local gradients in the chemical potential which in turn varies due to surface curvature. The chemical potential is written in terms of the surface geometry and free energy by the Herring formula [88]. In one dimension the chemical potential is:

$$\mu = \mu_0 + \kappa \Omega \gamma(\theta). \tag{2.16}$$

Here μ_0 is the chemical potential of a flat surface, κ is the local surface curvature taken to be positive for a convex surface, and $\gamma(\theta)$ is the surface free energy. In the case of an anisotropic surface free energy, γ will depend upon the angle of the surface normal, θ, in relation to the crystal orientation. Thus, the chemical potential of a system deviates from the equilibrium value (the potential for a flat surface) by an amount proportional to the curvature of the surface and the surface tension.

The gradient of the chemical potential, μ, is:

$$\nabla \mu = \Omega[\gamma(\theta) \nabla \kappa + \kappa \nabla \gamma(\theta)] \; . \tag{2.17}$$

If an isotropic surface free energy is considered, the second term of equation (2.17) becomes zero and the gradient in surface curvature is the sole driving force for the diffusion. This drives the diffusion of material from convex to concave regions and tends to smooth out the surface. An anisotropic surface free energy will result in a non-zero value for $\nabla\gamma(\theta)$ in equation (2.17) and is the origin of the facetting phenomenon.

During a process where the energy required for internal diffusion across grain boundaries is sufficient (such as during an anneal), microstructural evolution can occur through grain boundary migration [89] [90]. The motion is a phenomenon arising from the transport of material from one grain across a boundary to another. The possible driving forces for grain boundary migration include internal elastic strain, stored energy in the form of cold worked material and interface curvature. Grain boundary curvature is the driving force considered in the development of GROFILMS.

The Gibbs-Thompson equation gives the difference in the chemical potential across a boundary with a curved surface as [89]:

$$\mu_2 - \mu_1 = 2\gamma_{gb}\Omega\kappa. \tag{2.18}$$

where $\mu_{1,2}$ are the chemical potentials for the surfaces of grains 1,2, and Ω is the atomic volume, γ_{gb} is the grain boundary surface free energy and κ is the interface curvature. Thus, a grain boundary surface with a significant curvature will have a high chemical potential. Since the migrating material will diffuse from the high potential to the low, i.e. from the convex side of the grain boundary to the concave, the net effect will tend to straighten out the grain boundaries. GROFILMS kinetically calculates a flux of migrating atoms along the grain boundary using the following equation for the atomic flux, J_g:

$$J_g = -\frac{D_g \Omega \nu_g}{kT}(\mu_2 - \mu_1). \tag{2.19}$$

The equation for the diffusion coefficient D_g, is similar to (2.15) because of the Arrhenius dependence on temperature.

2.7 Implementation

Incorporation of the fundamental models into GROFILMS is important for the accurate

representation of the physical processes occurring during thin film growth. The next chapter discusses the algorithms and data structures upon which the models are implemented.

Chapter 3 GROFILMS Algorithms

3.1 Introduction

The initial development of the algorithms for the equilibrium GROFILMS simulator was done by Dr. S. Dew, co-developer of the SIMBAD/SIMSPUD process simulators [54]. The motivation behind the development of GROFILMS was to extend the ability to accurately represent the film and its physical properties and characteristics. In doing so, Dr. Dew developed the line/segment representation, data structures and processes such as diffusion and surface advancement. Subsequent work involved the modification of existing methods, verification of the models and addition of the kinetic processes, etching and grain boundary routines. Verification and applications presented in Chapters 4 and 5 also define the contributions to this body of work.

The implementation of the theories presented in the previous chapter is the focus of the following discussions. To begin, the thin film surface morphology, microstructure representation and manipulation are based upon a line segment / nodal description. Each model of the fundamental processes discussed in Chapter 2 is implemented in this representation. New equations are derived from the line segment geometries and are presented and discussed in this chapter.

3.2 Line Segment Representation

Representation of the thin film surface profile, microstructure and the topography over which it is deposited is important for both visual presentation of results and implementation of the algorithmic solutions of the physical processes. GROFILMS uses a line segment/ nodal approach for describing the film properties. Figure 3.1 presents a schematic diagram detailing the line segment method used to describe a thin film and its processes.

There exist eight unique nodal types each representing a specific element of the thin film microstructure. The node types are listed in Table 1 and presented in the schematic diagrams in Figure 3.1. The nodes that have paired up to form interfaces such as grain boundaries, substrate/film interfaces or triple points are treated as single node units. For each of these node types, interfacial energetics, local chemical potentials, other local quantities and

Figure 3.1 Schematic diagram of a thin film representation using GROFILMS. The different node types are labelled as in Table 1. Also shown are the local advancement and etching of the film surface and grain boundary migration.

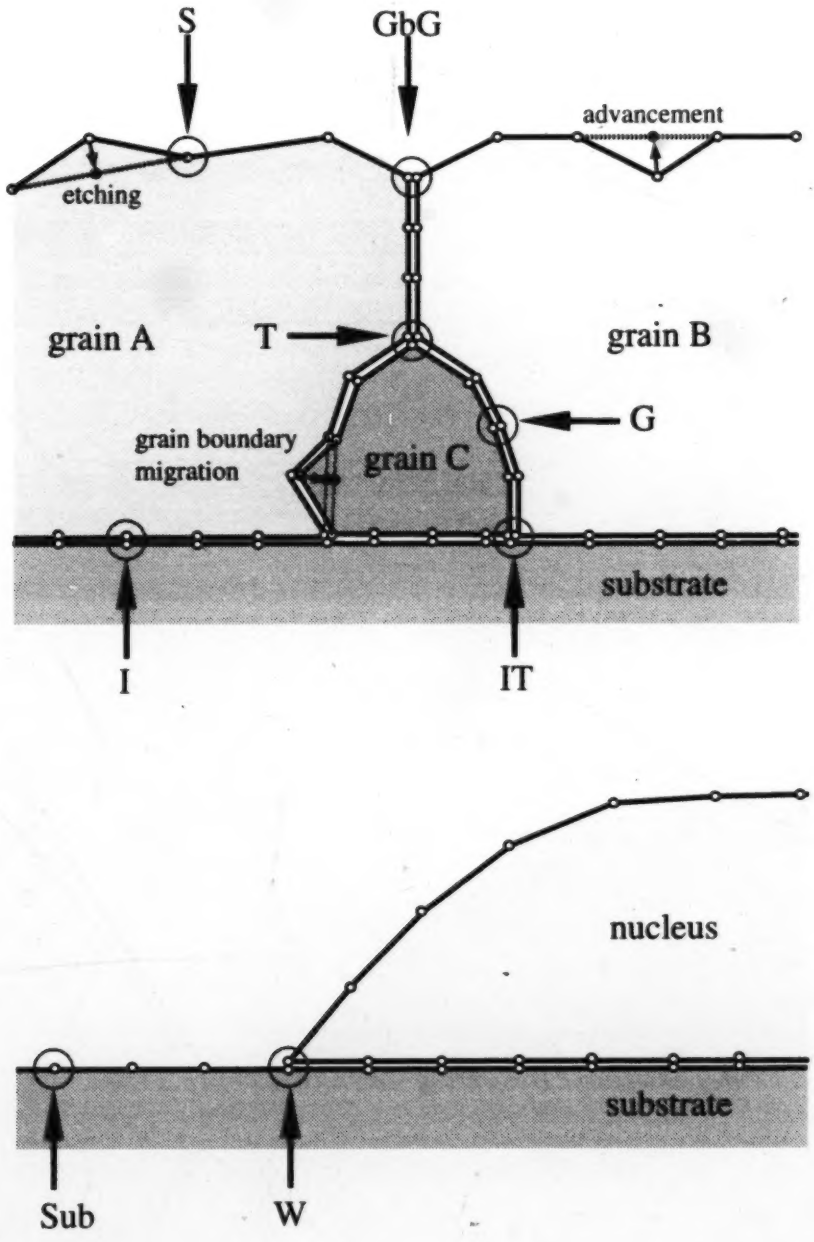

nodal movement are solved uniquely. As nodes are advanced, GROFILMS determines their fate by checking for collisions with other nodes or line segments. Nodes are dynamically added or deleted from memory as the surface and microstructure evolves. Nodal density is maintained close to that corresponding to one node per cell.

To implement the line segment method, the simulation space is divided up into cells, the number of which depends on the desired resolution. Periodic circular boundary conditions are imposed along the sides to prevent edge effects. Each cell contains a pointer to a bidirectional linked list of interconnecting nodes (linked via the `next` and `prev` pointers to the next and previous nodes in the list respectively). Line segments can be drawn between the nodes for surface representation and geometrical analysis.

The microstructure of a thin film is composed of grains or polycrystalline columns. Each grain or column is given an identification number to aid in the interfacial calculations and for storing grain-related information such as an associated crystallographic orientation. The outlines of each grain are represented by the line segments. During output, each grain or nucleus generated by GROFILMS is assigned a random color to highlight the microstructural character of the film.

Table 3.1: The specific node types used to represent a thin film and its microstructure using GROFILMS

Node identifier as shown in Figure 3.1	Node description
S	Surface node
Sub	Substrate surface node
GbG	Grain boundary grooving node pair
W	Wetting node pair
G	Grain boundary node pair
I	Interfacial node pair
T	Internal triple point node set
IT	Interfacial triple point node set

Figure 3.2 presents the code fragment defining the film node structure (`FILM_NODE`) which stores the local quantities and the pointers to the linked list. Local physical properties are stored in an additional data structure called `S_COMP` which houses data on capillarity

```
typedef struct film_struct FILM_NODE;
struct film_struct {
        MATERIAL_TYPE type;  /* material type */
        unsigned char flags; /* node property flags */
        int       grain_id; /* unique grain id */
        double    pos_x,    /* node position (x,y) */
                  pos_y;
        double    len_p,    /* length to prev node */
                  len_n;    /* length to next node */
       FILM_NODE  *prev,    /* pointer to prev node */
                  *next,    /* pointer to next node */
                  *grain,   /* grain (if applicable) */
                  *auxptr;  /* next node in same cell */
#ifdef KINETIC_GROFILMS
        void      *comp;    /* local physical details */

#else /* EQUILIBRIUM_GROFILMS */
        double    surface_E; /* free energy change volume */
#endif
};

typedef struct surf_compos S_COMP;
struct surf_compos {          /* composition structure */
        int       type;       /* surface comp type */
        float     surface_E;  /* capillarity diffusion */
        float     dK_dV;      /* first order correction */
        float     *conc;      /* adatom concentration */
        float     *vol;       /* solid volume array */
        float     *impinge;   /* impingement rate array */
};
```

Figure 3.2 Code fragment listing of the data structures (`FILM_NODE`) and the composition data structures that store the local physical quantities.

diffusion terms, adatom concentrations, impingement rates and excess volumes. Also, to minimize computation, local quantities such as next and previous node distances, positions and indentifier flags are stored in the `FILM_NODE` data structure.

3.3 GROFILMS Equilibrium Model

There are two major components of the equilibrium GROFILMS simulator: the ballistic impingement and the process stages as shown in the program execution schematic diagram of Figure 3.3. To represent the ballistic impingement of particle fluxes, a Monte Carlo par-

ticle generator launches particles with a specified trajectory. Surface impact locations are found with the local and feature-scale topographies taken into account. At this point, a decision is made as to what occurs next. The process will depend upon the particle type (sputtered material, bombarding ion, reflecting precursor species) and process probability (resputtering probability).

Thermodynamic equilibrium, presented beginning on p. 30, is the fundamental premise upon which diffusion and film deposition of the equilibrium GROFILMS model is based. Surface processes such as diffusion and growth are directly controlled by thermodynamic considerations. Implementation is determined by minimizing the total free energy of the system when new material is added to the system. This material is frozen in the appropriate position for the remainder of the simulation. Rather than explicitly calculating the free energy of the system, GROFILMS calculates the rate of change of the free energy with increasing volume, $\frac{d}{dV}\Delta G$, along the surface of the film (see equation (2.13)).

$$\frac{d}{dV}\Delta G = \sum_{S}\frac{d}{dV}(\gamma_S A_S) + F_v \tag{3.1}$$

Thus, keeping the system's total free energy to a minimum is achieved by regulating deposited material to locations where the rate of change of energy is a minimum. In this manner, the free energy change of the volume, F_v, can be neglected.

The GROFILMS equilibrium model is well suited for simulating the deposition of materials by either sputter or evaporation techniques. During these deposition processes, the film growth (and microstructure development) is generally governed by a single localized process. For example, film growth during low temperature sputtering is dominated by the shadowing of incident fluxes. The same equilibrium approximations made for the quasi-equilibrium, ballistic aggregation model used by SIMBAD [54] are valid for the GROFILMS simulator. Furthermore, using this approach to simulate film growth is fast, thereby freeing up computer resources. Non-localized phenomena, such as surface diffusion during an anneal, or the influence of competing processes require the comprehensive treatment of a kinetic model.

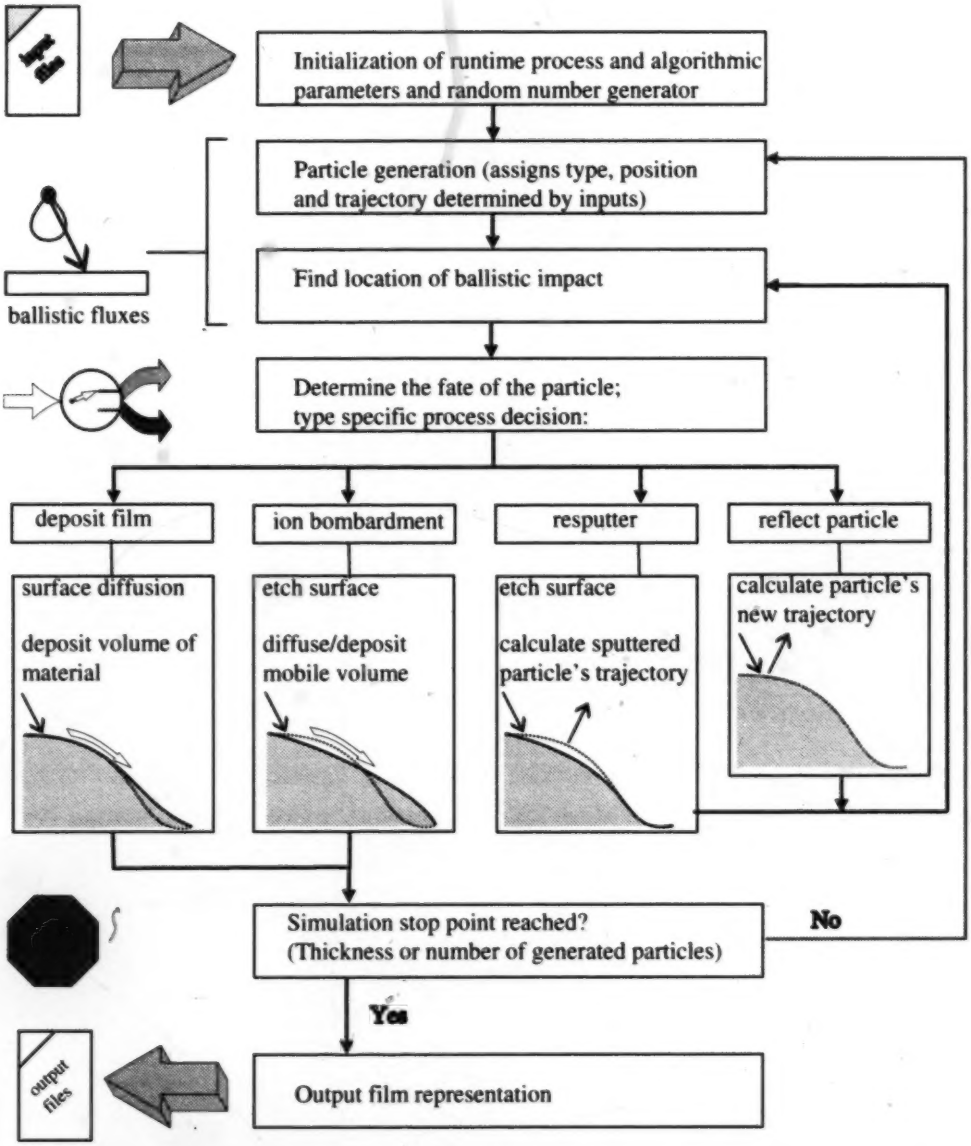
Initialization of runtime process and algorithmic parameters and random number generator
Particle generation (assigns type, position and trajectory determined by inputs)
ballistic fluxes
Find location of ballistic impact
Determine the fate of the particle; type specific process decision:
deposit film
ion bombardment
resputter
reflect particle
surface diffusion
deposit volume of material
etch surface
diffuse/deposit mobile volume
etch surface
calculate sputtered particle's trajectory
calculate particle's new trajectory
Simulation stop point reached? (Thickness or number of generated particles)
No
Yes
output files
Output film representation

Figure 3.3 Program organization of the GROFILMS simulation based upon the quasi-equilibrium models. Input files supply process and algorithmic parameters.

3.4 GROFILMS Kinetic Model

The GROFILMS kinetic model is necessary for accurately simulating deposition and post-processing techniques that are determined by a number rate equations. For example, metal CVD relies on the adsorption of precursors, desorption of by-products and chemical reactions at the surface. Under varying processing conditions, different reactions can be the limiting factor governing the thin film properties and deposition rates.

The kinetic model of GROFILMS calculates flux impingement rates, diffusion rates and surface reaction rates and thus the change in populations and surface advancement with time. Each of these rate equations is determined by the local geometry and properties of the film. Calculating and storing local surface areas, population densities and volumes is performed by GROFILMS. Further discussion on the kinetic algorithms for these processes can be found in Appendix A.

Of primary interest in this thesis is the kinetic modeling of surface self-diffusion due to capillarity forces (see p. 30). A kinetic description of diffusion is required as reflow distributes material globally, thereby making an localized equilibrium model ineffective. The diffusive flux current given by the Nernst - Einstein equation (2.14) is solved along the surface of the film. GROFILMS calculates the rate at which the volume of material flows into or away from each node. For each time step, the fluxes are converted to an absolute volume change. The volume of material at each node is stored in a temporary cache, V_C, and represented by surface advancement only after a threshold, V_T, is surpassed. The threshold is required to keep simulation execution times down as it would be computationally expensive to represent every change in volume with the movement of the nodes (especially when the volume is very small compared to the simulation resolution).

The local chemical potential is a function of the local surfaces, A_S, and the cached volume:

$$\mu = \mu(A_S) + \left(\frac{d\mu}{dV}(A_S)\right)V_C. \tag{3.2}$$

The second term of equation (3.2) is required to determine the local chemical potential due to the unrepresented cached volume and can be considered a first-order correction to the chemical potential solution.

3.5 Energetics, chemical potentials, and surface advancement

Each of the eight unique nodal representations of the film microstructure have their own energetics and chemical potential calculations. These quantities dictate diffusion and growth behaviour of thin films as outlined in Chapter 2. Reuse of code and simplification of calculations are possible by noting the following definition of the chemical potential:

$$\mu = \left(\frac{\partial G}{\partial N}\right)\Big|_{T,p} = \Omega\left(\frac{\partial G}{\partial V}\right)\Big|_{T,p} \tag{3.3}$$

Thus, in determining the chemical potential for kinetically solving the diffusion equations, reuse of the derivation for $\frac{d}{dV}\Delta G$ is possible with the multiplicative factor Ω, the atomic volume. The volume derivative of the chemical potential used in equation (3.2) is thus proportional to the second volume derivative of the free energy change:

$$\frac{d\mu}{dV}\Big|_{T,p} = \Omega\frac{d^2G}{dV^2}\Big|_{T,p} \tag{3.4}$$

Nodal movement represents local film growth, etching or boundary migration. The node placement is determined by the local geometry and the volume of material to be deposited. The line segment representation used by GROFILMS is strictly two dimensional (quasi-three-dimensional simulations are discussed in section (3.6) on p. 59) thus a volume of material is represented by a two-dimensional area multiplied by a depth standardized for convenience at one micron. For example, a volume of 0.01 μm^3 is represented by an areal change of 0.01 μm^2.

While the possible locations for a node are infinite within the simulation space, the line segment description of the thin film microstructure is still represented by a set of discrete lines. It is the geometry set out by these discrete line segments that is the foundation for all calculations. The following paragraphs detail the advancement and etching of the various surfaces as well as the energetic and chemical potential calculations used in both the equilibrium and kinetic models.

3.5.1 Surface Nodes

The surface nodes are the point of connection between two line segments forming the

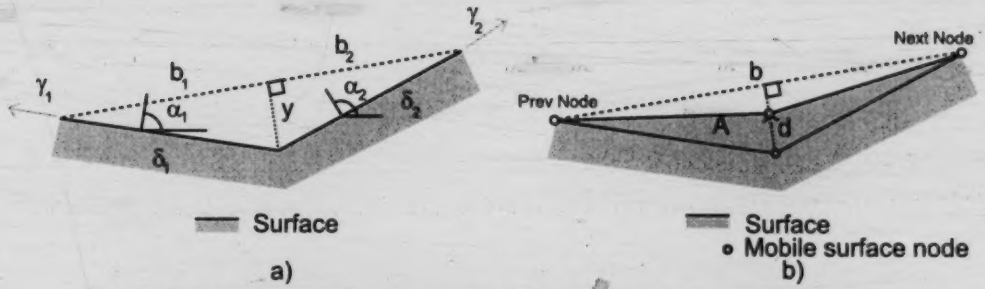

Figure 3.4 (a) Schematic diagram of the surface node parameters used in energetic and chemical potential gradient calculations. y is measured perpendicularly from the line connecting the next (Next) and previous (Prev) nodes. As this surface is concave, y is negative. The advancement of the surface node is represented in b). The distance the node moves depends upon the volume and the local geometries.

interface between a solid material (substrate or film) and the vapour or vacuum (Labelled *S* in Figure 3.1). Figure 3.4 a) describes in detail the local energetic parameters and line segment geometries needed in the following calculations.

Using the surface node geometries shown in Figure 3.4 a) to solve for the derivative of the change of free energy, ΔG, with volume V (equation (2.13) on p. 31) results in equation (3.5):

$$\left(\frac{d}{dV}\Delta G\right)_S = \Delta\left(\gamma_1\frac{d\delta_1}{dV} + \gamma_2\frac{d\delta_2}{dV} + \delta_1\frac{d\gamma_1}{d\alpha_1}\frac{d\alpha_1}{dV} + \delta_2\frac{d\gamma_2}{d\alpha_2}\frac{d\alpha_2}{dV}\right) \tag{3.5}$$

where the chain rule has been applied to the surface free energy derivative:

$$\frac{d\gamma_i}{dV} = \frac{1}{\Delta}\left(\frac{d\gamma_i}{d\alpha_i}\frac{d\alpha_i}{dA_i}\right). \tag{3.6}$$

The subscript *S* indicates the function is for surface nodes only. The δ_i are the line segment lengths and the γ_i are the surface free energies dependent upon the normal of the crystallographic surface orientation, α_i. The subscript i in equation (3.6) and the subscripts in the following equations refer to the summation over the line segments (i=1,2). The volume of material, V, is represented by multiplying the area on the simulation plane by the 1μm depth, Δ. The in-plane surface area is found by multiplying the line segment length, δ_i, by Δ.

To solve each of the volume derivatives in equation (3.5), an infinitesimal advance-

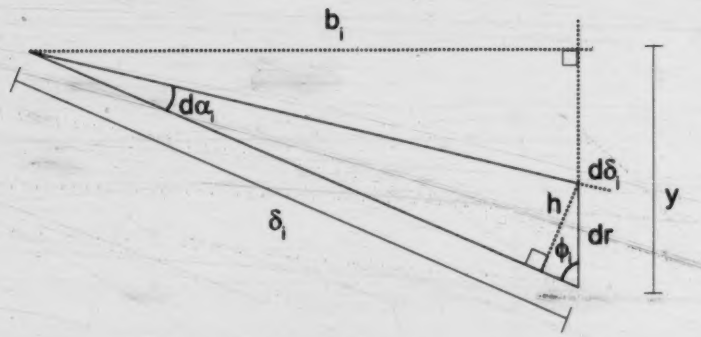

Figure 3.5 Geometry of an infinitesimal movement, *dr*.

ment of the surface node is considered, as in Figure 3.5. Using the line segment geometries, the first two derivatives of equation (3.5) can be rewritten as:

$$\frac{d\delta_i}{dA_i} = \frac{2}{\delta_i \tan\phi_i} = \frac{2y}{\delta_i b_i} \tag{3.7}$$

Again, the area, A_i, is the volume, V, divided by the depth, Δ.

Equation (3.6) can be rewritten using the following relationships:

$$d\alpha_i \approx \tan(d\alpha_i) = \frac{h_i}{\delta_i} \tag{3.8}$$

and

$$\tan\phi_i = \frac{h}{d\delta_i} = \frac{b_i}{y}, \qquad \therefore h = \frac{b_i d\delta_i}{y} \tag{3.9}$$

Thus:

$$d\alpha_i = \frac{b_i}{y\delta_i} d\delta_i \tag{3.10}$$

and

$$\frac{d\alpha_i}{dA_i} = \frac{d\alpha_i d\delta_i}{d\delta_i dA_i} = \left(\frac{b_i}{y\delta_i}\right)\left(\frac{2y}{\delta_i b_i}\right) = \frac{2}{\delta_i^2} \tag{3.11}$$

Substituting equations (3.7) and (3.11) into equation (3.5) yields:

$$\left(\frac{d}{dV}\Delta G\right)_S = 2\sum_i\left(\frac{1}{\delta_i}\frac{d\gamma_i}{d\alpha_i} + y\frac{\gamma_i}{\delta_i b_i}\right) \tag{3.12}$$

In the case of isotropic surface tension, where $\gamma_1 = \gamma_2 = \gamma$ and $\frac{d\gamma}{d\alpha} = 0$, equation (3.12) reduces to

$$\left(\frac{d}{dV}\Delta G\right)_S = 2\gamma y\sum_i\frac{1}{\delta_i b_i}. \tag{3.13}$$

Equation (3.12) is the energy minimization that the quasi-equilibrium model uses to govern film growth. Essentially, the minimization of the free energy is equivalent to the minimization of the geometrical area of the film. Concave surfaces have negative values of y yielding a negative value for $\left(\frac{d}{dV}\Delta G\right)_S$ (see Figure 3.4 a)). This means deposition of material at this point will serve to decrease the total free energy of the film. The magnitude of $\left(\frac{d}{dV}\Delta G\right)_S$ increases as the concavity increases resulting in some locations being more favorable for growth over others. The energy derivatives for convex surfaces will have positive values reflecting the energy penalty for depositing material on that location.

Chemical potentials and their volume derivatives are required for the kinetic simulation of capillarity-driven surface diffusion. Using the thermodynamic relationship of equation (3.3), the chemical potential is:

$$\mu_S = 2\Omega\sum_i\left(\frac{1}{\delta_i}\frac{d\gamma_i}{d\alpha_i} + y\frac{\gamma_i}{\delta_i b_i}\right) \tag{3.14}$$

The volume derivative of the chemical potential is found by solving (3.4). This begins as:

$$\frac{d\mu}{dV} = 2\Omega\sum_i\left(\frac{d\gamma_i}{d\alpha_i}\frac{d}{dV}\left(\frac{1}{\delta_i}\right) + \frac{1}{\delta_i}\frac{d^2\gamma_i}{d\alpha dV} + \left(\frac{\gamma_i}{\delta_i b_i}\right)\frac{dy}{dV} + \frac{y}{b_i}\left(\frac{1}{\delta_i}\frac{d\gamma_i}{dV} + \gamma_i\frac{d}{dV}\left(\frac{1}{\delta_i}\right)\right)\right), \tag{3.15}$$

where each derivative in (3.15) is solvable in terms of the line-segment geometry. The volume derivative of the first term is:

$$\frac{d}{dV}\left(\frac{1}{\delta_i}\right)^{\cdot} = \frac{1}{\Delta}\frac{d}{dA_i}\left(\frac{1}{\delta_i}\right) = \frac{1}{\Delta}\frac{d}{d\delta_i}\left(\frac{1}{\delta_i}\right)\frac{d\delta_i}{dA_i} = -\frac{2y}{b_i\delta_i^3}\left(\frac{1}{\Delta}\right). \tag{3.16}$$

The second derivative of the second term in (3.15) becomes:

$$\frac{d^2\gamma_i}{d\alpha_i dV} = \frac{1}{\Delta}\left(\frac{d^2\gamma_i}{d\alpha_i^2}\right)\frac{d\alpha_i}{dA_i} = \frac{1}{\Delta}\left(\frac{d^2\gamma_i}{d\alpha_i^2}\right)\frac{2}{\delta_i^2} \tag{3.17}$$

where the final step uses equation (3.11). The third term derivative is:

$$\frac{dy}{dV} = \frac{1}{\Delta}\frac{dr}{dA_i} = \frac{1}{2\Delta}b_i \tag{3.18}$$

Using equations (3.6) and (3.11) and substituting (3.16), (3.17) and (3.18) into (3.15) finally yields:

$$\frac{d\mu}{dV} = \frac{4\Omega}{\Delta}\sum_i\left(\frac{\gamma_i}{b_i^2\delta_i}\left(2-\frac{y^2}{\delta_i^2}\right)+\frac{d\gamma_i}{d\alpha_i}\left(\frac{2y}{b_i\delta_i^3}\right)+\frac{d^2\gamma_i}{d\alpha_i^2}\frac{1}{\delta_i^3}\right), \tag{3.19}$$

which simplifies in the case of isotropic surface energetics:

$$\frac{d\mu}{dV} = \frac{4\Omega}{\Delta}\sum_i\frac{\gamma_i}{b_i^2\delta_i}\left(2-\frac{y^2}{\delta_i^2}\right). \tag{3.20}$$

The kinetic algorithms use finite difference calculations to determine the gradient in the chemical potential from equations (3.12) or (3.13) in accordance with equation (3.3). Surface diffusion fluxes (equation (2.14)) are calculated along the surface and an absolute volume change is calculated for each time step. Advancement/etching of a node is performed when the magnitude of the cached volume surpasses a programmed threshold.

Calculation of the surface node motion is based upon the local geometrical configuration. For both deposition and etching, the node moves in the direction perpendicular to the line connecting the next (Next) and previous (Prev) nodes (see Figure 3.4 b)) This line serves to define the local surface normal. The distance, *d*, the node moves is determined by V, the amount of material to be deposited at that node:

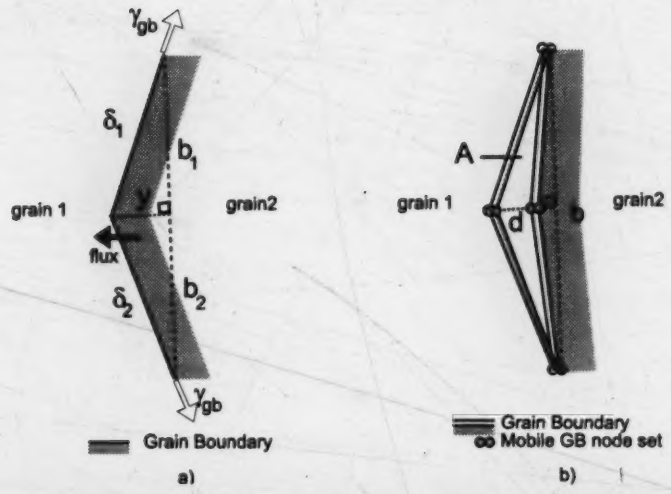

Figure 3.6 a) Schematic diagram of the grain boundary node pair with the material flux and energetics indicated. b) shows the motion of the nodes during grain boundary migration (in the direction opposite to that of the material flux).

$$d = 2\left(\frac{V}{\Delta}\right)\frac{1}{b} \tag{3.21}$$

where again, Δ, the 1μm depth is taken into consideration.

3.5.2 Grain Boundary Pairs

The internal microstructure of a thin film is characterized by the presence of the grain boundaries. Grain boundary nodes (labelled *G* in Figure 3.1) are paired nodes as each grain contributes a node. Grain boundary migration can occur as discussed on p. 33, thus requiring the calculation of local chemical potentials differences as described in equation (2.18). A schematic diagram of the grain boundary line segment/nodal geometries used in the calculations is presented in Figure 3.6 a). The motion of a grain boundary node is shown in Figure 3.6 b).

Grain boundary migration calculations need to be standardized in a way that makes the calculations uniform throughout the entire simulation space. This was accomplished by the following grain boundary migration definitions. All chemical potential calculations are evaluated with respect to the grain with the lower sequentially assigned identification (ID) number and diffusive fluxes are added positively onto the grain with the lower ID. Figure

3.6 a) shows the material flux moving from the grain with ID = 2 to the other with ID = 1. The material is thus accumulating on grain 1. The curvature (calculated with respect to grain 1) is negative and the volume added is positive. Finally, to be consistent, movement is also decided with respect to the grain with the lower ID.

The calculation of the chemical potential difference along a grain boundary surface is given by the Gibbs - Thomson equation (2.18) on p. 33. The chemical potential difference across the grain boundary is solved using the line segment geometries in Figure 3.6 a) where the curvature, κ, can be calculated as:

$$\kappa = \frac{dA}{dV} = y\sum_i \frac{1}{b_i \delta_i} \tag{3.22}$$

where the last step is derived from equation (3.7). As the GROFILMS simulator does not consider anisotropic grain boundary energetics, the resulting equation for the chemical potential difference is:

$$\Delta\mu_G = 2\gamma_{gb} y\sum_i \frac{1}{\delta_i b_i}, \tag{3.23}$$

and the volume derivative of $\Delta\mu_G$ is:

$$\left(\frac{d}{dV}\Delta\mu\right)_G = \frac{2\Omega}{\Delta}\sum_i \frac{\gamma_{gb}}{b_i^2 \delta_i}\left(2 - \frac{y^2}{\delta_i^2}\right) \tag{3.24}$$

The motion of the grain boundary node is determined in a similar manner to that of the surface node. For evaluating the distance moved by a grain boundary node, equation (3.21) is reused.

3.5.3 Grain Boundary Grooving Node Pairs

Grain boundary node pairs that are also part of the surface of the film are designated grain boundary grooving nodes (labelled *GbG* in Figure 3.1). These nodes are unique because their energetics incorporate both surface and grain boundary contributions. As discussed on p. 28, the grain boundary grooving phenomenon occurs at this surface location due to this interaction of the surface and grain boundary energetics. Figure 3.7 a) presents the necessary parameters and geometric variables used in calculating the local energetics.

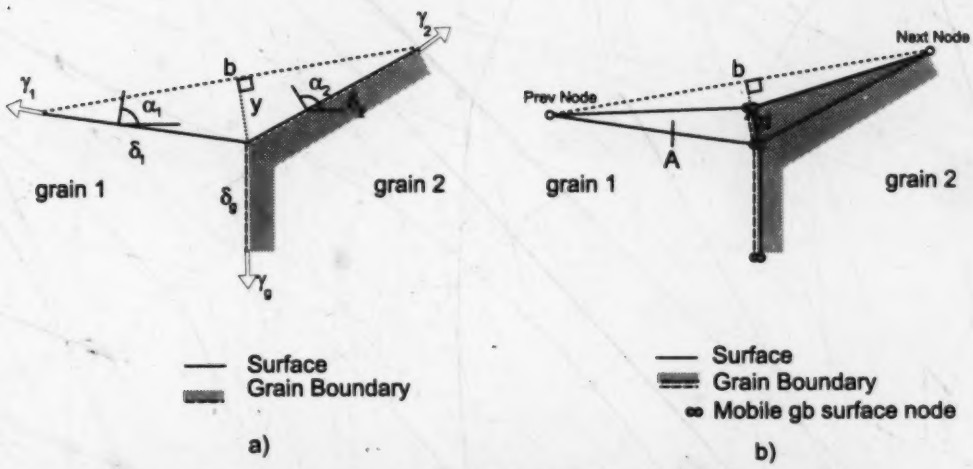

Figure 3.7 (a) Schematic diagram of the grain boundary grooving node pair and the parameters used in energetic and chemical potential calculations. The motion of the grain boundary grooving pair is shown in (b).

Figure 3.7 b) schematically shows the advancement of a grain boundary grooving node pair.

Calculation of the free energy derivative for grain boundary grooving nodes (subscript *GbG*) is similar to that for the surface nodes. However, there is the contribution from the grain boundary, as shown in equation (3.25):

$$\left(\frac{d}{dV}\Delta G\right)_{GbG} = \left(\frac{d}{dV}\Delta G\right)_{S} + \frac{d}{dV}(A_{gb}\gamma_{gb}) \tag{3.25}$$

Considering isotropic grain boundary free energies, (3.25) reduces to:

$$\left(\frac{d}{dV}\Delta G\right)_{GbG} = \left(\frac{d}{dV}\Delta G\right)_{Surf} + \gamma_{gb}\frac{dA_{gb}}{dV}. \tag{3.26}$$

Using the two dimensional geometry set out in Figure 3.7 a), the resulting function for $\left(\frac{d}{dV}\Delta G\right)_{GbG}$ is:

$$\left(\frac{d}{dV}\Delta G\right)_{GgG} = \frac{2\gamma_{gb}}{b_1 + b_2} + 2\sum_i\left(\frac{1}{\delta_i}\frac{d\gamma_i}{d\alpha_i} + \frac{\gamma_i y}{\delta_i b_i}\right). \tag{3.27}$$

Likewise, the chemical potential calculations at a grain boundary groove are:

$$\mu_{GbG} = \Omega\left(\frac{d}{dV}\Delta G\right)_{GgG}. \tag{3.28}$$

The volume derivative of the chemical potential at a grain boundary groove is identical to that for a surface node, equation (3.19) or (3.20), as the first term in (3.27) is zero. The remainder is equal to that of the surface node calculations.

When considering deposition of material, the movement of the grain boundary grooving nodes is very similar to that of a regular surface node. The motion is along the line perpendicular to the line connecting the next and previous neighbouring nodes on the surface (labelled in Figure 3.7 b)). The distance is determined by equation (3.21). The grain boundary will extend as the surface advances. GROFILMS adds new grain boundary node pairs when the resolution requirements dictate.

Etching of material at the grain boundary groove removes film material from the surface at the location of the groove. Etching at a groove will tend to deepen the groove along the grain boundary. Thus etching is restricted along the grain boundary.

3.5.4 Wetting Node Pair

The wetting node pair exists as an interfacial boundary between the film and substrate and as a surface. An example of these nodes is labelled *W* in Figure 3.1. The wetting phenomenon of materials is discussed on p. 28.

The equation for the change in free energy derivative (3.1) for the wetting node pair becomes:

$$\left(\frac{d}{dV}\Delta G\right)_W = \frac{d}{dV}(A_{sf}\gamma_{sf} + A_{sv}\gamma_{sv} + A_{fv}\gamma_{fv}) \tag{3.29}$$

To solve (3.29), the surface free energy associated with the interfacial boundary (between the substrate and film) and the surface free energy of the substrate are assumed isotropic ($\frac{d\gamma_{fs}}{d\alpha} = 0$ and $\frac{d\gamma_{sv}}{d\alpha} = 0$). The following relations derived from the geometry of Figure 3.8 a) are used to solve (3.29):

$$\frac{dx}{dA} = \frac{2}{y}, \quad \text{and} \quad dx = \frac{\delta}{x}d\delta. \tag{3.30}$$

The first volume derivatives can then be written as:

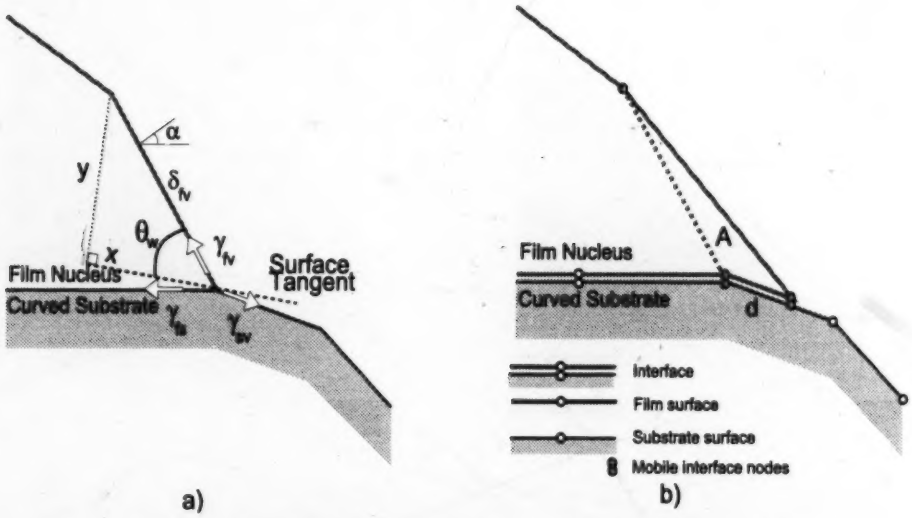

Figure 3.8 (a) Schematic diagram of the wetting node pair and the parameters used in energetic and chemical potential gradient calculations and (b) the advancement motion.

$$\frac{dA_{fs}}{dV} = -\frac{dA_{sv}}{dV} = \frac{dx}{dA} = \frac{2}{y} \tag{3.31}$$

The derivative of the film surface area with volume (the third term in (3.29)) becomes:

$$\frac{dA_{fv}}{dV} = \frac{d\delta}{dA} = \frac{2x}{y\delta} \tag{3.32}$$

where the equations of (3.30) are used in the last step. And finally, the derivative of the film surface free energy with volume is solved using:

$$d\alpha \sim \tan d\alpha = \frac{\sin\theta_w}{\delta} dx = \frac{2}{\delta^2} dA \tag{3.33}$$

where (3.30) was used in the final step. Thus, $\frac{d\gamma_{fv}}{dV}$ becomes:

$$\frac{d\gamma_{fv}}{dV} = \frac{1}{\Delta d\alpha}\frac{d\gamma_{fv}}{d\alpha}\left(\frac{d\alpha}{dA}\right) = \frac{2}{\Delta\delta^2 d\alpha}\frac{d\gamma_{fv}}{d\alpha} \tag{3.34}$$

Thus, by substitution of equations (3.31) to (3.34) into (3.29), the final form of the derivative of the free energy change is:

$$\left(\frac{d}{dV}\Delta G\right)_w = 2\left(\gamma_{fv}\frac{x}{y\delta} + (\gamma_{fs} - \gamma_{sv})\frac{1}{y} + \frac{x}{\delta^2}\frac{d\gamma_{fv}}{d\alpha}\right) \tag{3.35}$$

The chemical potential of the wetting node is calculated from (3.35) as:

$$\mu_w = \Omega\left(\frac{d}{dV}\Delta G\right)_w \tag{3.36}$$

The first derivative of the chemical potential, $\left(\frac{d\mu}{dV}\right)_w$ is solved by using the above relationships plus the additional relation:

$$\frac{d}{dV}\left(\frac{1}{\delta}\right) = -\frac{1}{\Delta\delta^2}\frac{d\delta}{dA} = -\frac{2x}{\Delta y\delta^3} \tag{3.37}$$

to give:

$$\left(\frac{d\mu}{dV}\right)_w = \frac{2\Omega}{\Delta}\left(\frac{\gamma_{fv}}{y^2\delta}\left(1 - \frac{x^2}{\delta^2}\right) + \frac{1}{y\delta^2}\left(1 + \frac{x}{\delta} - \frac{2x^2}{\delta^2}\right)\frac{d\gamma_{fv}}{d\alpha} + \frac{x}{\delta^4}\frac{d^2\gamma_{fv}}{d\alpha^2}\right). \tag{3.38}$$

Movement of the wetting nodes is restricted along the substrate as shown in Figure 3.8 b). The distance is calculated knowing the volume to be deposited, V as:

$$d = \frac{2V}{y\Delta}. \tag{3.39}$$

3.5.5 Internal Triple Point Node Set

Internal triple points describe the special scenario where three grains come together to form a line (a point in two dimensions) rather than a surface (line) [89]. Referring to the schematic diagram of Figure 3.1, this point is described by a three node set labelled with a *T*. The schematic diagram used in calculating the chemical potentials is shown in Figure 3.9. In this figure, the motion of the triple point is given by the vector ***R***. However, as will be discussed below, the chemical potential calculations and the subsequent triple point motion are highly dependent on this vector. Thus it must be determined first.

Consider first the following description of a triple point. The triple point is defined by three grains that meet at some point O as shown in Figure 3.10. The interfacial surface ten-

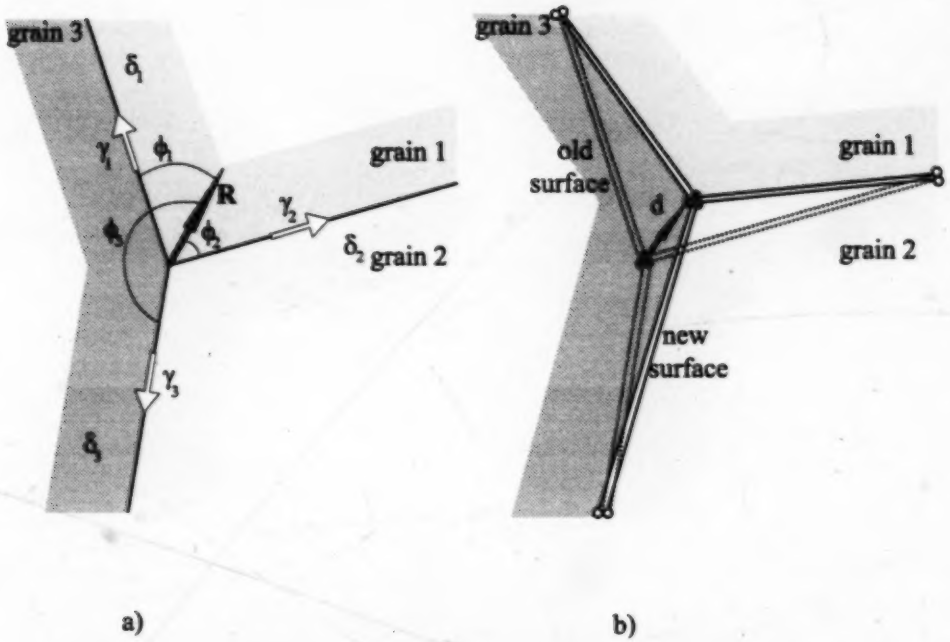

Figure 3.9 a) The geometry used in calculating the chemical potential and its derivatives in GROFILMS. b) The triple point motion as represented using the nodal description.

sions are given by σ_{12}, σ_{23}, and σ_{13}. Balancing the tensions vectorially at the triple point determines the equilibrium angles θ_1, θ_2, and θ_3. If the three contributing surfaces have the same tensions ($\sigma_{12} = \sigma_{23} = \sigma_{13}$), the three angles should be equal (120°) when equilibrium is established.

Calculation of the thermodynamic potential at this point can be found considering the grain boundary surface energetics, γ_{gb} and a differential change in geometrical configuration. This function has been calculated for restrictive motion of the triple point as illustrated in Figure 3.10 (see reference [89] chapter 7 for the calculation of the potential for motion along one of the grain boundaries). However, the triple point in the GROFILMS simulation has the freedom to move in any direction within the simulation plane. In Figures 3.9 and 3.11, this direction is shown by the vector ***R***. Thus, the potentials calculated at a triple point are direction of motion as well as geometry dependent. This is described by the following definition:

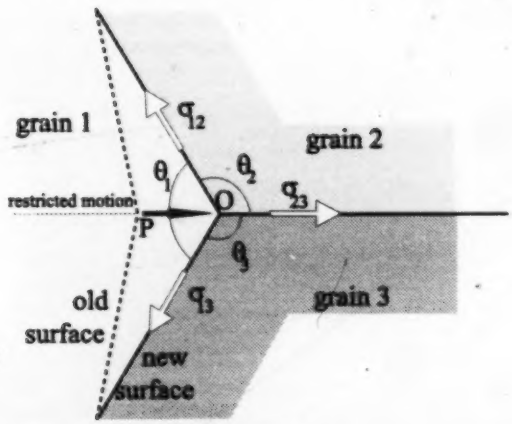

Figure 3.10 Restricted triple point junction movement along one of the grain boundaries from point P to point O. If each of the tensions is equal, at equilibrium the angles between each of the grain boundaries, θ, is 120°.

$$(\Delta\mu)_T = \Delta\mu_T(A_s, \boldsymbol{R}) \tag{3.40}$$

where T refers to the triple point nodes and

$$\boldsymbol{R} = \boldsymbol{R}(R, \Phi). \tag{3.41}$$

The first step in triple point calculations is to determine the motion vector, $\boldsymbol{R}$. This vector is defined by the direction of motion that will result in the greatest reduction in the total free energy of the system per distance travelled. $\boldsymbol{R}$ is determined by summing the contributing motion vectors of each of the three grains, $\boldsymbol{r}_i$. In two dimensional cartesion coordinates, each vector is $(x_i\hat{i} + y_i\hat{j})$ and $\boldsymbol{R}$ is:

$$\boldsymbol{R} = (x_1 + x_2 + x_3)\hat{i} + (y_1 + y_2 + y_3)\hat{j} \tag{3.42}$$

Thus, Φ, the angle $\boldsymbol{R}$ makes with the horizontal and defines the direction of motion for the chemical potential calculations is:

$$\Phi = \operatorname{atan}\frac{X}{Y} = \operatorname{atan}\left(\frac{\sum x_i}{\sum y_i}\right). \tag{3.43}$$

The next step is to determine each of the contributing vectors, $\boldsymbol{r}_i$. These vectors have direction and magnitude. The direction, given by the angle of the vector with respect to the

horizontal, ϕ_i, is determined from the local geometry; the direction is perpendicular to the line joining the next and previous nodes of the grains triple point node. Figure 3.11 shows each of the vectors $\boldsymbol{r}_i$ as determined from the geometry.

The magnitude of each vector reflects the extent to which that node deviates from an equilibrium state and how fast motion in that direction will lead to equilibrium. The magnitude is thus dependent upon $\Delta\theta_i$, the deviation from the equilibrium angle of 120° (assuming isotropic grain boundary energetics):

$$\Delta\theta_i = \theta_i - 120° \tag{3.44}$$

Positive values for $\Delta\theta_i$ indicate that the internal angle is greater than the equilibrium value and motion of the triple point to the convex side (away from the grain) will decrease the angle. Likewise, a negative value for $\Delta\theta_i$ will result in $\boldsymbol{r}_i$ having a negative magnitude and motion will be into the grain and thereby increase the angle.

The magnitude of the $\boldsymbol{r}_i$ are also moderated by the rate in which the angles, θ_i, will change with infinitesimal motion in the direction of $\boldsymbol{r}_i$.

$$\frac{d\theta_i}{d\boldsymbol{r}} = \left(\frac{\sin\omega_1}{\delta_1} + \frac{\sin\omega_2}{\delta_2}\right)_i \tag{3.45}$$

where the ω_j are the angles between the motion vector and the grain boundary j. Thus, the $\boldsymbol{r}_i$ are:

$$\boldsymbol{r}_i = \left(\Delta\theta_i \frac{d\theta_i}{d\boldsymbol{r}}\right)\hat{r} + \phi_i\hat{\phi} = \Delta\theta_i\left(\frac{\sin\omega_1}{\delta_1} + \frac{\sin\omega_2}{\delta_2}\right)_i (\cos\phi_i\hat{i} + \sin\phi_i\hat{j}). \tag{3.46}$$

By substituting the results of (3.46) into (3.42) and (3.43) gives the final form for the direction of the motion vector $\boldsymbol{R}$:

$$\Phi = \text{atan}\left(\frac{\sum_i \Delta\theta_i\left(\frac{\sin\omega_1}{\delta_1} + \frac{\sin\omega_2}{\delta_2}\right)_i \sin\phi_i}{\sum_i \Delta\theta_i\left(\frac{\sin\omega_1}{\delta_1} + \frac{\sin\omega_2}{\delta_2}\right)_i \cos\phi_i}\right) \tag{3.47}$$

In determining the current flux of material, the driving force is the difference in the chemical potential from equilibrium, $(\Delta\mu)_T$. Here, the subscript T refers to the triple point

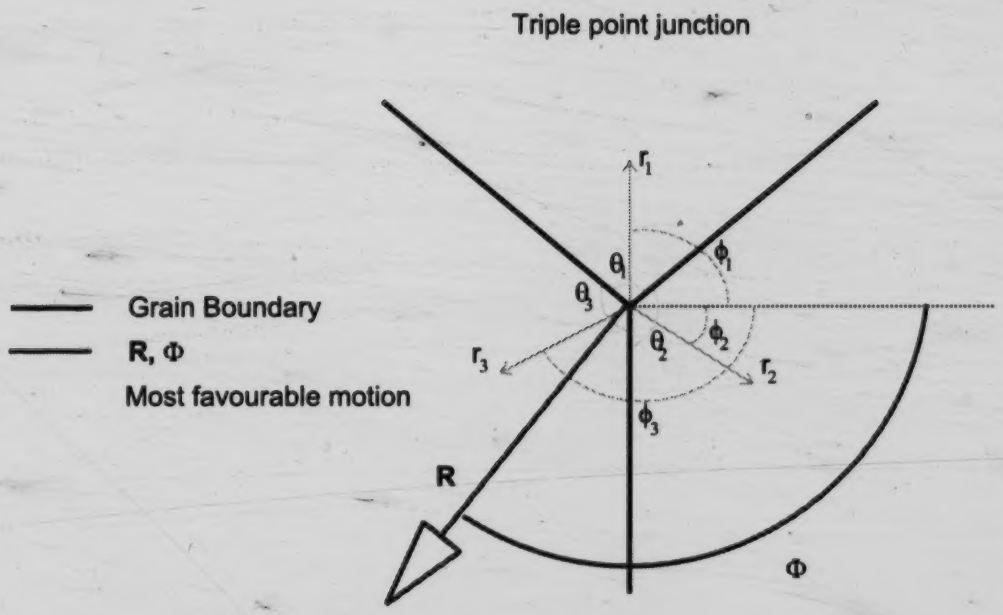

Figure 3.11 To determine the most favorable motion; r,Φ, for a triple point junction, the above geometry is used in calculation of (3.47)

node. Placing the direction of motion vector determined above into the line segment geometries as in Figure 3.9 a), $(\Delta\mu)_T$ can be calculated from:

$$(\Delta\mu)_T = \Omega\frac{d}{dV}\Delta G_T = \gamma_{gb}\frac{d}{dV}\sum_i^3 (A_{gb})_i \tag{3.48}$$

where the $(A_{gb})_i$ are the areas of each of the three grain boundaries meeting at the triple point. The derivatives are:

$$\left(\frac{dA_{gb}}{dV}\right)_i = \frac{d\delta_i}{dA} = \frac{d\delta_i}{dr}\frac{dr}{dA} = \frac{2\cos\phi_i}{\delta_i \sin\phi_i} \tag{3.49}$$

such that:

$$(\Delta\mu)_T = -2\Omega\gamma_{gb}\left(\sum_i \frac{\cot\phi_i}{\delta_i}\right) \tag{3.50}$$

The cached volume must also be taken into consideration when calculating the value of

$(\Delta\mu)_T$. Thus the value of $(\Delta\mu)_T$ is changed by $V_C\left(\frac{d}{dV}\Delta\mu\right)_T$ where the derivative is found to be:

$$\left(\frac{d}{dV}\Delta\mu\right)_T = \frac{4\Omega\gamma_{gb}}{\Delta}\sum_{i=1}^{3}\frac{(\cot\phi_i)^2}{\delta_i^3}, \tag{3.51}$$

where the following relation was used with (3.49):

$$\frac{d}{dV}\frac{1}{\delta_i} = \frac{1}{\Delta}\frac{d}{d\delta}\left(\frac{1}{\delta}\right)\frac{d\delta}{dA} = -\frac{1}{\Delta}\frac{1}{\delta_i^2}\frac{d\delta_i}{dA} \tag{3.52}$$

As with each node or node set, the distance moved during its motion is determined by the local geometry and the amount of volume to be deposited. In the case of an internal triple node set, the distance, *d*, is calculated as:

$$d = \frac{2V}{\Delta}\left(\sum_i \delta_i \sin\phi_i\right)^{-1}. \tag{3.53}$$

3.5.6 Interfacial Node Pairs and Interfacial Triple Point Node Set

The node pairs marking the boundary between two different materials such as the substrate and the film are designated as interfacial node pairs (labelled *I* in Figure 3.1). The representation of this boundary is not only useful for separating film and substrate, but the boundary can play an important role in diffusion and reaction (silicide formation) problems. Current implementation of the GROFILMS simulator does not incorporate these phenomena and does not allow for the migration of this boundary.

Interfacial triple point node sets represent points at which two grains contact each other on the substrate/film interface. These nodes (labelled *IT* in Figure 3.1) belong to the grain boundary and can likewise migrate. The chemical potential calculations use the geometry shown in Figure 3.12 a). The nodal motion is shown in Figure 3.12 b).

The derivative of the free energy change with volume is solved at the interfacial triple point. The result is multiplied by the atomic volume to get the chemical potential.

$$\Delta\mu_{IT} = \Omega\left(\frac{d}{dV}\Delta G\right)_{IT} = \Omega\gamma_{gb}\frac{dA_{gb}}{dV} \tag{3.54}$$

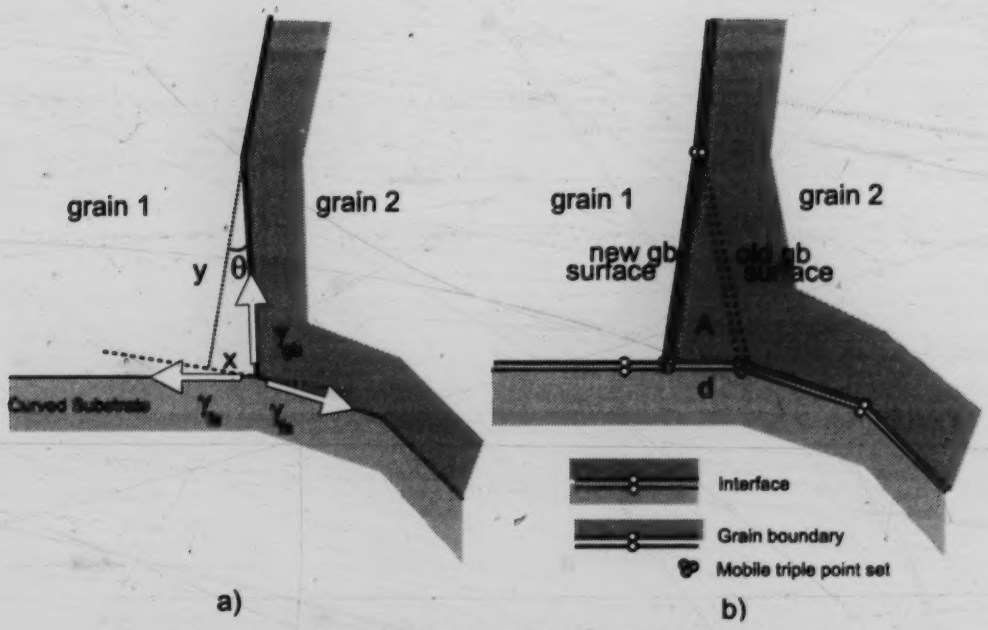

Figure 3.12 a) Schematic diagram of the interfacial triple node set. The geometry is outlined in a). b) shows the motion of the triple point along the substrate / film interface.

The contribution to $\Delta\mu_{IT}$ due to the changing of the interfacial boundary from one grain to the other is not included in the calculation. It is assumed that the interfacial energetics between the film and substrate are identical for each grain regardless of orientation.

The following relationship

$$\frac{dA_{gb}}{dV} = \frac{d\delta}{dA} = \frac{2x}{y^2} \tag{3.55}$$

is substituted into (3.54) to give:

$$\Delta\mu_{IT} = \frac{2\gamma_{gb}\Omega x}{y^2} \tag{3.56}$$

The volume derivative of $\Delta\mu_{IT}$ is found to be:

$$\left(\frac{d}{dV}\Delta\mu\right)_{IT} = \frac{4\Omega\gamma_{gb}}{\Delta y^3} \tag{3.57}$$

where:

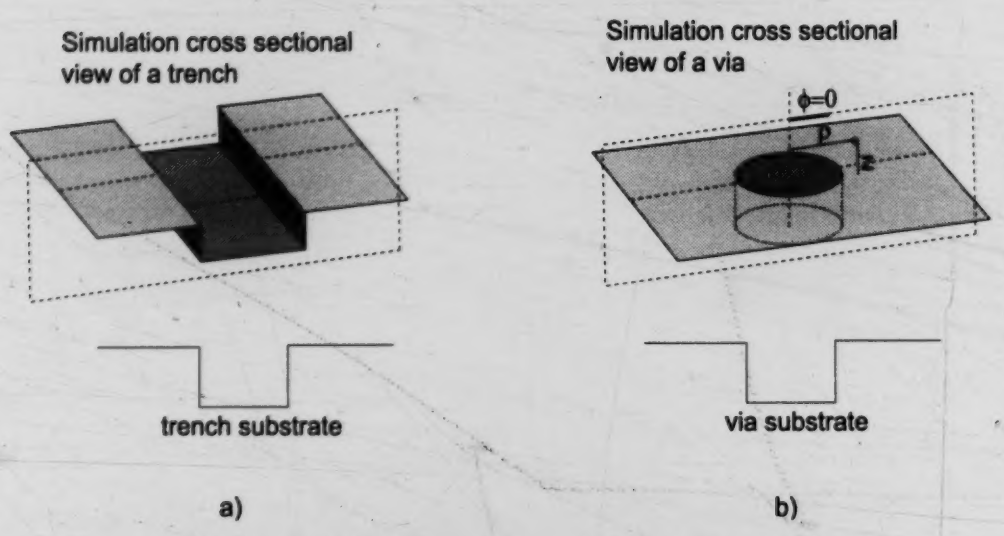

Figure 3.13 Schematic diagram of the cross-sectional views of trenches (a) and vias (b). The views appear the same in simulation results, but are derived from different symmetries.

$$\frac{dx}{dV} = \frac{2}{\Delta y} \tag{3.58}$$

3.6 Quasi-Three Dimensional Simulations

Vias and trenches are the most common topographical features that must be filled for successful metallization. Dual damascene processing is an exception where vias exist within trenches. The inherent symmetries of the features are exploited by the GROFILMS simulator: trenches are considered symmetrical in the plane of the simulation while vias exhibit symmetry through any plane passing through the central axis of the via. These symmetries are made explicit in Figure 3.13. With appropriate projections, these important three dimensional structures can be simulated by a two-dimensional simulator like GROFILMS.

3.6.1 Quasi-three-dimensional flux generation

A complete discussion of the cylindrical symmetry solution to flux generation as applied to the thin film deposition simulator SIMBAD is presented in Appendix A of reference [54]. The same solution, called quasi-three-dimensional in previous work [36], is applied

by GROFILMS in the calculation of a true three-dimensional trajectory represented in cylindrical coordinates $(\rho, \phi, z)_{3D}$. The particle position is mapped onto the two-dimensional simulation space by

$$x_{2D} = \frac{1}{2}\text{width} \pm \rho, \tag{3.59}$$

$$y_{2D} = z. \tag{3.60}$$

where $\frac{1}{2}$ width is the middle of the simulation space corresponding to the axis of symmetry. The choice of $\pm$ depends on whether the particle is in the left or right half of the simulation. Both are equivalent, but a particle generated on one side should never cross to the other.

There exists no explicit dependence of the two-dimensional position on ϕ as the projection is kept in the plane of the simulation. This plane as shown in Figure 3.13 rotates around the axis of symmetry with the particle thereby keeping ϕ=0. The trajectory is stepped and periodically mapped onto the two dimensional simulation plane to check for impact on the surface of the film or substrate.

The contribution of the particles to the surface is also affected by the cylindrical symmetry of the quasi-three-dimensional model. In particular, the quasi-three-dimensional algorithms generate many more particles and impact locations at larger radii, ρ. This is because there is a correspondingly larger area to which the particle contributes (the area at radius ρ is $2\pi\rho\, d\rho$ which increases linearly with ρ). Thus particles must be effectively weighted according to the impact radius. In the same manner as the discrete particle generation of the SIMBAD simulator, GROFILMS discards the particles according to a probability function proportional to $1/\rho$ (with a limitation on ρ as it approaches zero) [54].

3.6.2 Surface energetic calculations

Unlike the trench simulations that assume a standard depth into the plane of the simulation (see p. 42), the approach used here must take into consideration a surface with curvature into the plane of the simulation. The surface curvature, or the radius of curvature, is directly dependent upon the radius of the hole in the film. It is assumed that the out-of-plane curvature is uniform along its entire circumference. Thus, equation (2.16) describing the local surface chemical potential is rewritten as:

$$\mu = \mu_o + \Omega\gamma(\kappa + \kappa_q) \tag{3.61}$$

where $\kappa_q = 1/\rho_q$ is the contribution of the out-of-plane curvature as shown in Figure 3.14. ρ_q is determined by:

$$\rho_q = \frac{\rho}{\cos\theta_s} \tag{3.62}$$

where ρ is the distance between the axis of symmetry and the surface element and the angle θ_s gives the orientation of the surface normal with respect to the horizontal. Thus for surfaces whose normal is perpendicular to the radial line (for example, the flat top surfaces), there is no out-of-plane curvature.

Grains or columns that are of sizes far less than the topographical feature size require different treatment of the extra out-of-plane curvature term when calculating the local chemical potentials. This is because the column structure should not be assumed to have a uniform out-of-plane curvature of the order of the feature radius. Rather, the column has a finite depth, and its surface curvature is not affected by the existence of cylindrical symmetry. This type of film structure usually results from processes where there is a low surface diffusion component. Under these conditions, the shadowing of ballistic flux dominates the development of film microstructure and filling properties and the out-of-plane curvature driven diffusion can be neglected.

The out-of-plane curvature of the surface of a via hole is negative when the surface normal is oriented toward the axis of symmetry, positive otherwise. The magnitude of the curvature will increase greatly with diminishing hole diameter. For materials and processes where capillarity-driven diffusion will redistribute material, the locations of lower thermodynamic potential (the regions of the hole with the smallest diameter) are the most favorable. Thus, there is the tendency for via holes to rapidly close off with decreasing size.

3.7 Required Computer Resources

GROFILMS was developed on a myriad of work stations including but not limited to Sun SPARC station 20, Digital Alpha Station 200, Pentium 166 Mhz (Linux), and Hewlett Packard 712/60. On these machines, the GROFILMS equilibrium model can simulate the deposition of a thin film using computational times on the order of a few minutes. The ki-

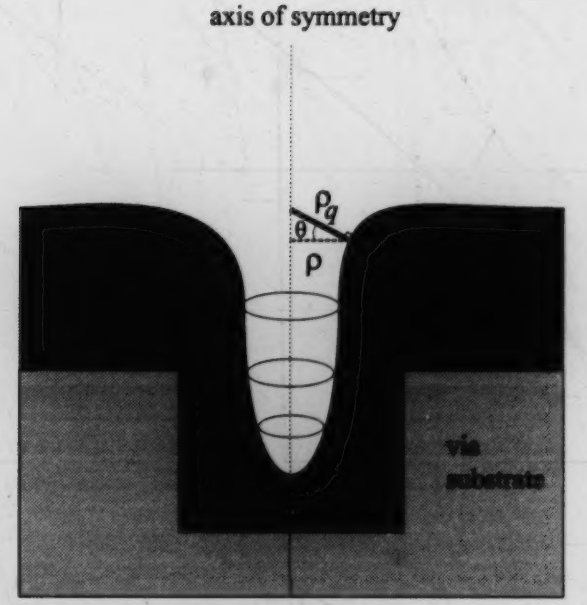

Figure 3.14 Schematic diagram of the radius of curvature for out-of-plane surface curvature calculations.

netic simulations require more time as they must solve reaction and diffusion equations along the surface and microstructure of the thin film. The reflow simulations, as presented in Chapter 5 of this dissertation, require computational times ranging from 1 to 12 hours. Memory resources necessary reached maximum of 4 megabytes of random access memory. The important simulation parameters governing the computational and memory requirements are the simulation resolution and space, and number and type of reaction and diffusion equations and parameters.

3.8 Summary

The algorithms that define the GROFILMS simulator are very much dependent upon the line segment/nodal description of the film. The geometrical solutions to calculating local physical quantities were presented in this chapter. These solutions and the discrete film representation are used for the simulation of the physical models presented in Chapter 2. The next chapter will demonstrate the ability of the GROFILMS simulator to accurately model the physical phenomena that characterize thin films.

Chapter 4 Modeling the Fundamental Processes

Testing GROFILMS to properly model the most basic characteristics exhibited by thin films deposited by physical vapour deposition is important in order to gain confidence in the simulation. The fundamental processes include nucleation, wetting phenomena, surface phenomena such as facetting and grain boundary grooving, development thin film microstructure including columnar and grain growth, and film coverage over topography. Furthermore, basic deposition conditions reflected by the ballistic description of the incoming fluxes are tested.

4.1 Initial Stages of Thin Film Growth

Nucleation and coalescence are the first stages in the growth of thin films during both CVD and PVD processing and are important in determining the eventual structure and properties of the film. Growth of stable islands and the extent to which coalescence occurs dictates the initial sizes of the subsequent grains or columns. The main mechanism for controlling the island sizes is the thermal energy-controlled surface diffusion of the mobile adatoms. The islands in this model are considered immobile. This assumption is justified as the much greater adatom mobility dominates transport. Chapter 2, p. 21 discusses nucleation and coalescence in terms of the energetic and kinetic theoretical considerations for the GROFILMS models.

A material-independent parameter used to describe the thermal energy state of the system is the ratio of the substrate or deposition temperature, T_S, to the melting temperature, T_M, of the deposited material. A high density of small stable islands will develop during depositions where the temperature ratio T_S/T_M is low. The low thermal energy reduces the distances the adatoms travel and allows them to nucleate in many closely spaced islands. The high density of small nuclei will lead to a large number of columns. Competition between the growing columns will eventually become the governing mechanism of the film microstructure. The lower density, larger nuclei formed during a deposition with more thermal energy will evolve into a more granular microstructure where grain growth competition will play a major role in determining the eventual film texture.

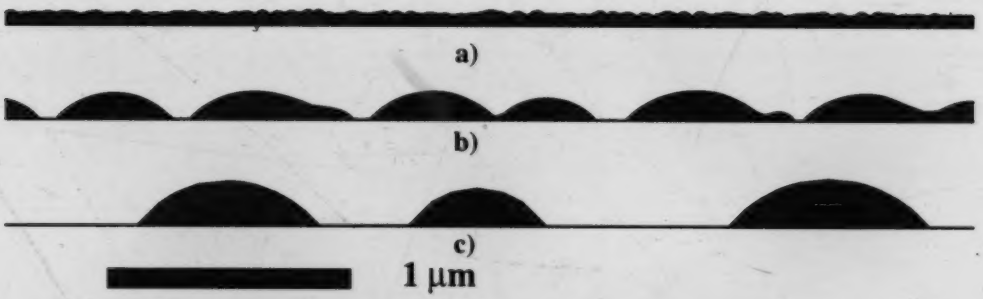

Figure 4.1 Nucleation of thin films occurs during the initial stages of growth. The density and size of the nuclei depends upon the material specific temperature ratio: T_S/T_M. A low temperature deposition is shown in a). b) and c) are simulations with increasing temperature ratios (diffusion lengths).

The GROFILMS energetic model illustrates the nucleation phenomenon as dependent upon the substrate/metal melting temperature ratio. In each of the simulations of Figure 4.1, the same volume of material is deposited but with a change in the thermal energy available (by change of diffusion length).

Figure 4.1 a) is a GROFILMS simulation of the nucleation during a low temperature deposition. The film has formed a continuous layer yet it has evolved from an extremely large number of nucleation sites. Figure 4.1 b) and c) show simulation results where the thermal energy has been increased. These films are composed of large islands, some of which have come into contact and formed grain boundaries. The wetting properties are also evident where the substrate has remained exposed. Figure 4.1 c) in fact is completely composed of large isolated islands.

The wetting properties of a thin film are governed by the interfacial and surface energetics of the system. The variation in substrate wetting between different materials is characterized by a wetting angle as discussed in Chapter 2, p. 28. For metallization processing, the metal/substrate wetting characteristics are very important. In particular, the filling of sub-micron features is affected by the metal's ability to cover the surface [91].

The results of the energetic GROFILMS model of film nucleation are presented Figure 4.2. A variety of possible wetting properties of different materials is demonstrated. For example, Figure 4.2 shows islands with wetting angles of 10°, 45° and 135°. These simulations show wetting behaviour expected at the initial stages of thin film growth. Table 4.1

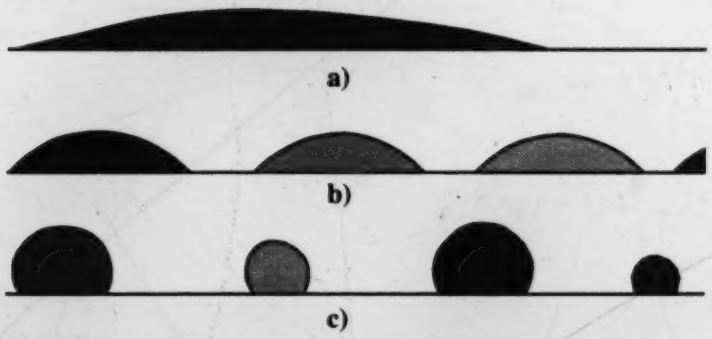

Figure 4.2 (a) Almost complete wetting (θ=10°) generated with; (b) partial wetting (θ=45°); and (c) almost no wetting (θ=135°). In each simulation, film surface tension is 1.4 J/m^2. The simulation width is approximately 1 μm.

summarizes the interfacial energetics used in generating Figure 4.2.

As an example of wetting characteristics of a metal influencing metallization process development, GROFILMS is used to study the implications of poor substrate wetting by PVD aluminum on SiO_2 [14] [92]. GROFILMS illustrates the complications with hot aluminum deposition by comparing two deposition simulations at different temperatures. A hot deposition (Figure 4.3 a)) is used to increase adatom mobility and aid in the filling of trenches. However, it often results in a poorly wetted substrate which can lead to voided regions. By depositing a cold layer of aluminum as the initial step (Figure 4.3 b)), a wetting layer providing good coverage is formed. Subsequent deposition can proceed at the higher temperatures to aid in trench filling. These results are in accordance with the known problems associated with sputtered aluminum depositions under conditions of high temperature [16].

Table 4.1: Parameters used in generating the wetting examples of Figure 4.2. The film surface tension is 1.4 J/m^2.

Figure 4.2	Substrate surface energy (J/m^2)	Interfacial energy (J/m^2)	Resulting wetting angle
(a)	1.5	0.14	10°
(b)	1.24	0.25	45°
(c)	1.25	2.1	135°

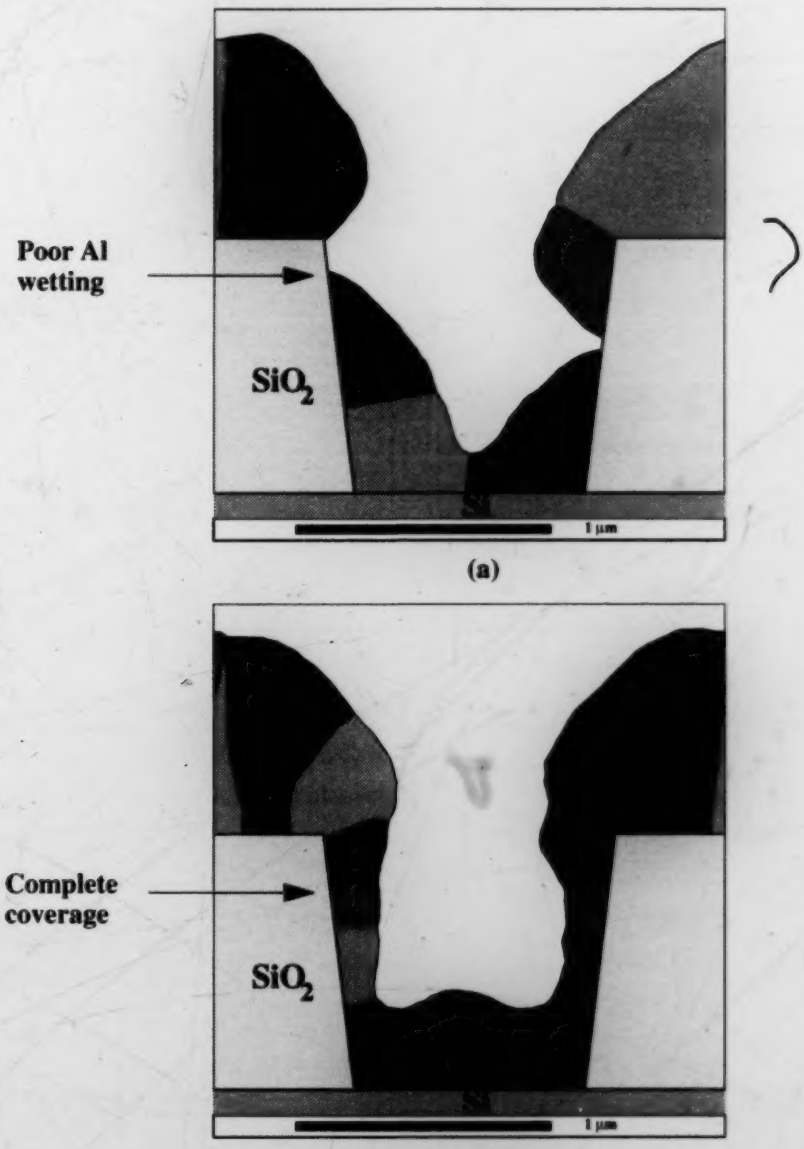

Figure 4.3 (a) Aluminum deposition over topography at high temperature. The poor wetting character of Al on SiO_2 results in incomplete filling and film discontinuities. (b) To avoid this problem, a wetting layer (Al deposited at lower temperature) is used to completely cover the topography before the temperature is raised to increase Al mobility.

The GROFILMS model is further tested by comparing simulation output to known analytical equilibrium solutions. Specifically, for substrate wetting, the values of the isotropic energetics γ_{sv} and γ_{fs} are varied such that the phenomenon covers the entire range of wetting, i.e. from almost perfect wetting to almost zero wetting. Typical values used are for the film surface free energy: gold, γ_{vf} is 1.4 J m^{-2}[79]; substrate surface energy: silicon, γ_{sv} is 1.24 J m^{-2} [93]; and the interfacial energies: copper on silicon, γ_{fs} is 0.2 J m^{-2}.

The contact angle, θ_S, is calculated from the results generated by GROFILMS.θ_S is determined by taking an average of many wetting angles. and compared with the theoretical angle, θ_Y, predicted from thermodynamic equilibrium (see equation (2.8) on p. 28). A plot of the wetting angles versus $(\gamma_{sv} - \gamma_{fs}) / \gamma_{vf}$ is presented in Figure 4.4. The solid line represents the equilibrium angle, θ_Y and the dark circles are the results derived from GROFILMS simulations. The magnitude of the standard deviation in the measurements is less than that covered by the filled circles, so no error bars are present. Agreement is evident between the theoretical equilibrium wetting angles and those generated by GROFILMS.

4.2 Thin Film Surface Morphology

The surface morphology of a thin film describes the roughness of surface features. A thin film's morphology will depend upon deposition conditions as well as the fundamental properties of the material. For example, the extent to which grain boundary grooving occurs or whether or not a material will facet is dictated by surface and interfacial energetics. Further, high temperature processing enhances a phenomenon such as facetting by supplying the thermal energy that regulates diffusion. The surface morphology of a metal film is particularly important as it can affect subsequent processing. For example, rough surfaces can degrade lithography, increase anneal times or cause unreliable deposition of other materials and thus affect processing.

Grain boundary grooving is a surface phenomenon that will affect the film's morphology (see p. 28 for a discussion). Graphical demonstrations as generated by the GROFILMS simulation of the phenomenon are presented in Figure 4.5. The figures illustrate that an increase of the grain boundary energy can cause a significant change in the surface morphology. Figure 4.5 a) has zero grain boundary energy which effectively eliminates grain boundary grooving. The surface of this thin film simulation is smooth regardless of the

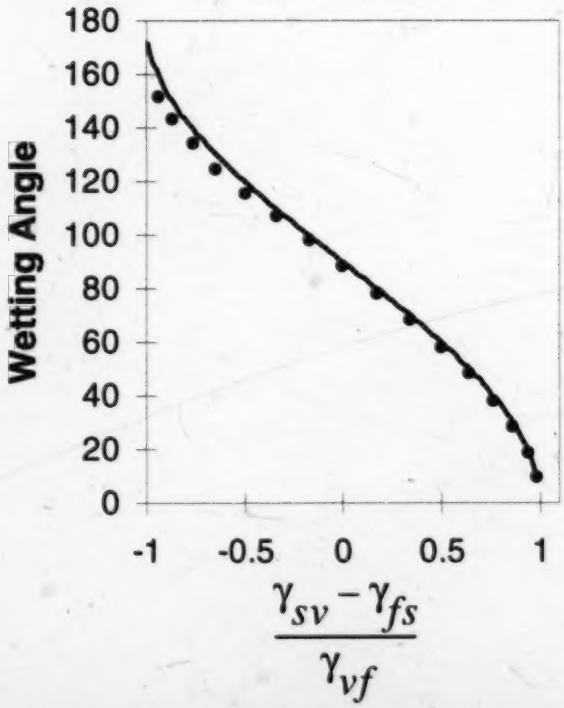

Figure 4.4 A comparison of the equilibrium wetting angle as calculated from equation (2.8) (solid line) with the wetting angles generated by GROFILMS (solid circles). Both calculations are plotted versus $\gamma_{sv} - \gamma_{fs} / \gamma_{vf}$. The comparison ranges from almost complete wetting (θ=10°) to almost no wetting (θ=160°)

number of grains. Figure 4.5 b) and c) have non-zero values for grain boundary energy thus resulting in a rougher surface morphology. The grooving angles and the surface energies (γ_{vf} and γ_{gb}) used in the generation of Figure 4.5 are listed in Table 4.2. These values were chosen for purposes of illustration as actual values for various materials are often difficult to obtain.

To test the GROFILMS model, a comparison of the generated output is made to the expected equilibrium grooving angles (see equation (2.9) on p. 29). A value for the surface energy, γ_{vf} is set at 1.24 J·m^{-2} and the grain boundary energy, γ_{gb}, is changed to generate the entire range of possible grooving angles: from 0° to 90°. A grooving angle, $\phi_S/2$, is calculated from the GROFILMS simulations and compared to $\phi_e/2$, as determined by equation (2.9). $\phi_S/2$ is plotted in Figure 4.6 (dark circles) versus the input value of the grain boundary

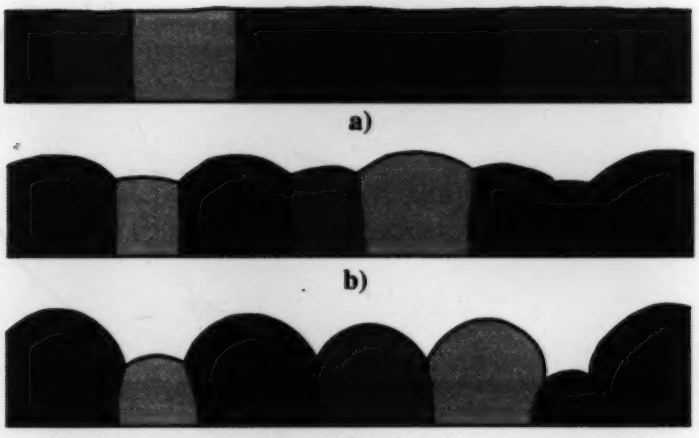

Figure 4.5 Different magnitudes of grain boundary grooving dependent on the input parameters γ_{vf} and γ_{gb} (see Table 4.2). (a) No grain boundary grooving; (b) medium grooving occurring with $\phi/2=60°$; and (c), high grooving $\phi/2=30°$. The lines are used to illustrate the grooving angles. The simulation width is approximately 1 μm.

energy. The solid line represents the equilibrium grooving angle, $\phi_g/2$. Agreement is good over the entire range of possible grooving angles.

Table 4.2: Parameters used in generating the grain boundary grooving examples of Figure 4.5.

Figure 4.5	Surface energy (J/m^2)	Grain boundary energy (J/m^2)	Resulting grooving angle ($\theta_g/2$)
(a)	1.4	0.0	90°
(b)	1.4	1.4	60°
(c)	1.4	2.4	30°

Another prominent surface phenomenon is facetting. Facetting will directly affect the morphology of a thin film as the crystal planes of relative low energy become exposed and create a rough surface. Facetting is most likely to occur during high temperature processes such as an anneal. See p. 33 for a discussion on the origin of the facetting phenomenon.

To illustrate the facetting phenomenon, the GROFILMS simulation can employ an anisotropic surface free energy. The surface energy variation chosen in this section approx-

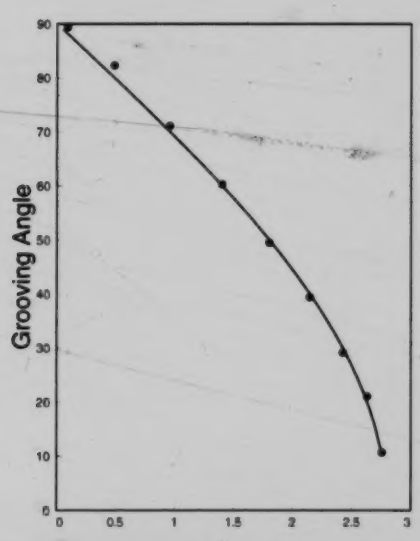

Figure 4.6 A comparison of the equilibrium grooving angle ($\phi_g/2$) calculated from equation (2.9) with the grain boundary grooving angles generated with GROFILMS ($\phi_S/2$). Both calculations are determined with a surface tension of 1.24 J m^{-2} and plotted against the grain boundary interfacial tension, γ_{gb}.

imates that perpendicular to the [100] plane of a body centered cubic (bcc) crystal [79]. The surface energetics approximation is presented in Figure 4.7. Here, the surface energy is given versus the surface orientation measured with respect to the crystal orientation, α. The figure shows an oscillating behaviour of γ_{vf} with minima occurring every 45°. While not representative of all bcc crystals and using a low level of detail, this function qualitatively reproduces the crystal surface energetic configuration. The magnitude of the surface energy function in Figure 4.7 is representative of a bcc metal such as W.

Facetting results generated by GROFILMS are presented in Figure 4.8. Figure 4.8 (a) exhibits no facetting. These nuclei were generated with isotropic surface tensions and are included for comparison. Figure 4.8 (b) demonstrates facetting. There appears a preferential growth of planes at 45° to each other. This is expected as the Wulff plot and Figure 4.7 predicts these planes to be stable for a bcc crystal. A preferred crystal orientation was assumed to be prevalent during nucleation, hence the regular distribution of favourable planes and similar grain structures.

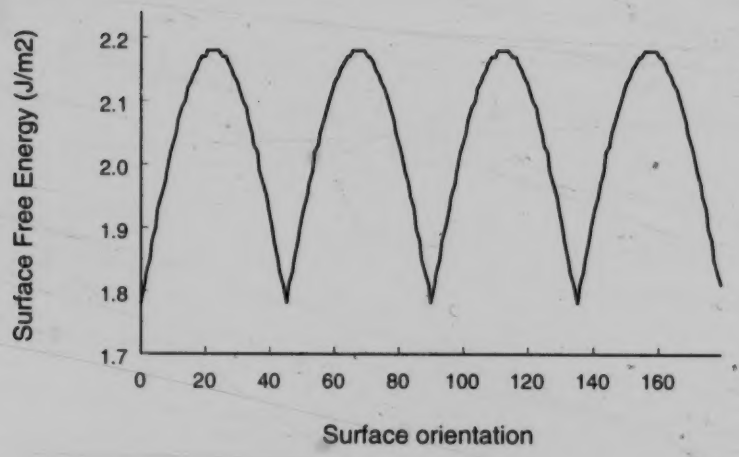

Figure 4.7 The surface energetics as a function of surface orientation. The energetics approximates those taken perpendicular to the [100] plane of a bcc crystal. Low energy surface crystal orientations exist every 45°

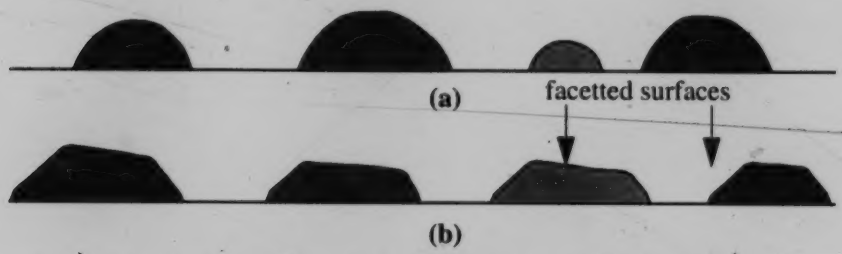

Figure 4.8 Various forms of crystal facetting. (a) Using isotropic surface tension results in no facetting. (b) Favourable planes occurring every 45° as predicted by a Wulff plot perpendicular to the [100] plane of a cubic crystal. The grains were generated with a preferred orientation during nucleation. The simulation width is approximately 1μm.

4.3 Thin Film Microstructure

The performance of the metallization materials are greatly dependent upon the microstructure of the films. For example, the frequency and sizes of the grains composing the interconnect material will influence material properties such as resistivity [94] and reliability issues such as electromigration susceptibility [18]. The microstructure of barrier layers can

Figure 4.9 GROFILMS simulation of a thin film with possible Zone I microstructure. Many voids exist between the columns though not visible at the current resolution.

affect performance as the grain boundaries of a columnar or highly granular microstructure will eventually allow for diffusion of materials. Thus, the microstructure of the thin films used for metallization is an important property to understand.

The Movchan-Demchishin (MD) and Thornton Zone models describe some of the structures of thick films that can be expected under various deposition conditions. The relevant discussion is presented in Chapter 2. Generally, these same structures can be reproduced by the GROFILMS simulations. All simulations in this section use a flux distribution of a typical metal evaporation. Each simulation has a bcc facetting component as described on p. 69.

Figure 4.9 is a GROFILMS simulation of a thin film 0.7 μm thick. The deposition conditions were chosen to result in a typical zone I structure. The very low diffusion length (0.0025 μm) and high resolution of the simulation space give rise to the large nucleation density and thus the many columns. From the nucleation layer rises a region of intense competition between the growing columns that continues to 500 nm of growth. At this point, the columns grow and form many small voided regions not easily noticed in the graphical representation.

This film therefore appears quite dense even though a highly porous film is expected. The dense simulated film structure can be attributed to two conditions. First, the GROFILMS simulation is two dimensional and does not consider the finite three dimensional character of the columns. (See the discussion in p. 42 for the symmetry used in the GROFILMS simulation.) Second, under such low diffusion conditions, the local growth at the impingement

point on the surface is expected to be highly directional, that is, parallel to the incoming flux. The GROFILMS advancement routines as outlined in Chapter 3 are geometric solutions. Geometric surface motion is defined as motion that is dependent only upon the position and local shape of the surface [95]. The discrepancy between directional and geometric surface growth may make true reproduction of Zone I growth difficult.

By increasing the temperature or choosing a material with a lower melting temperature (thereby increasing T_s/T_m) one increases diffusion and thus changes the film morphology and microstructure. Figure 4.10 a) was generated by using a diffusion length of 0.01 μm. This simulated film exhibits many of the fundamental characteristics of thin films: facetted surfaces have begun to form. Examples of the emerging facets and the existing domed columns are labelled on the figure. Where the grain boundaries intersect the surface, grooves form. The magnitude of the grooves depends upon the variation of the local surface energies. For example, the groove labelled A in Figure 4.10 a) is much deeper and pronounced than that labelled B.

The microstructure of Figure 4.10 a) consists of densely packed fibrous grains. Grain boundaries exist rather than the isolated columns of Figure 4.9. Competition between grains under these deposition conditions can be dependent upon both film energetics (surface-diffusion-controlled) and shadowing. Many of the initial grains are likely shadowed during growth as their larger neighbours continue to grow at faster rates. With thicker films, the mechanism for competition between grains is likely controlled by surface diffusion and interfacial energetics.

Figure 4.10 b) is very similar to Figure 4.10 a) in that the surface exhibits facetting and grain boundary grooving. The grain sizes are appreciably larger as the simulated temperature increase enhanced the surface diffusion length. The diffusion length used in the simulation was 0.05 μm.

The last simulation, Figure 4.10 c) used a diffusion length of 0.09 μm. Here, the grain sizes are substantially larger. Grain growth competition is dominated by low energy facetting as the surface diffusion facilitates facet formation.

Experimentally, the grain sizes of 100 nm thin films of various metals were determined as a function of T_S/T_M [96]. At this thickness, the results indicate the grain sizes for zone II films range from 5.5 nm to approximately 110 nm. A similar analysis of the simu-

lations of Figure 4.10 was performed. The grain sizes are calculated at the lines indicating 100 nm and 500 nm of growth. The results are shown in Table 4.3 and indicate the simulations of Figure 4.10 a) and b) would be within Zone II (see Figure 2.4). However, considering the sizes of the grains, these films would be in the higher temperature range of Zone II. The simulation results of Figure 4.10 c) would likely evolve into a Zone III film as the grain sizes at 100 nm are 115.7 nm. Furthermore, at the higher temperatures, bulk diffusion and grain boundary migration will tend to reconstruct the microstructure by eliminating the small energetically unfavourable grains.

Table 4.3: Grain sizes of a 100 nm thick film of various metals at different deposition temperatures. Results obtained from reference [96]

Experimental Temperature Ratio	Grain size at 100 nm thick (nm)
0.25	5.5
0.5	109

Table 4.4: Grain sizes of a 100 nm thick film as simulated by GROFILMS.

GROFILMS Simulation Diffusion Length	Grain Size at 100 nm thick (nm)	Grain Size at 500 nm thick (nm)
0.01	39	129
0.05	71.1	185
0.09	115.7	366

4.4 Deposition Processes

When studying thin film deposition, accurately representing the phenomena associated with growth is important. The ability to incorporate substrate topography with any feature size and shape is equally important when using a model to optimize process development for microelectronic metallization. It is necessary to successfully predict film properties such as bottom coverage, sidewall coverage and film microstructures (see p. 17 for the definitions of these properties).

An example of using GROFILMS to simulate deposition over topography is presented in Figure 4.11 a). This is a simulation of tungsten deposition into a 1:1 aspect ratio trench.

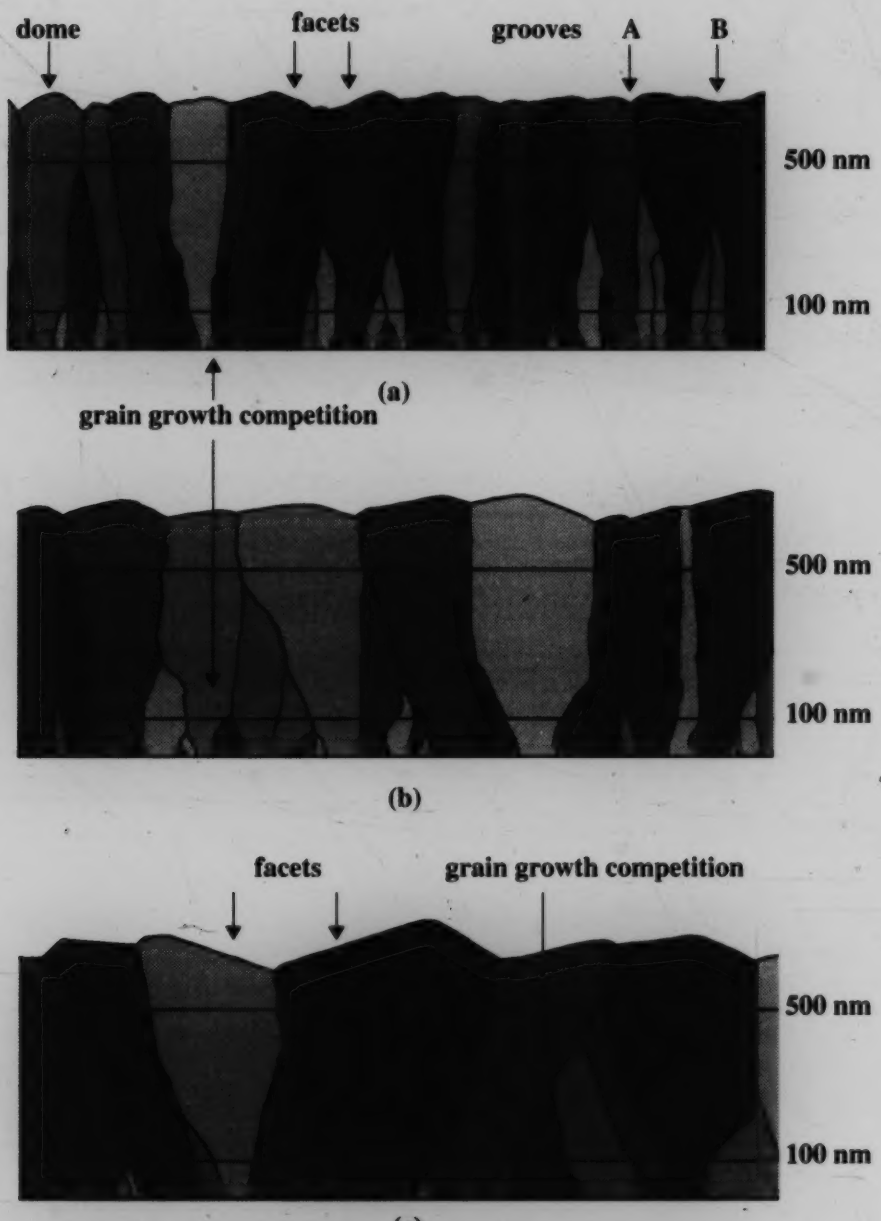

Figure 4.10 Simulations of temperature-dependent microstructures. (a) Highly fibrous and dense film generated with a diffusion length of 0.01 μm. (b) An increase in temperature (diffusion length of 0.05 μm) during growth enhances grain boundary grooving. (c) Further increases in temperature result in facetting and the growth of large grains. A diffusion length of 0.09 μm was used. The simulation width is approximately 2 μm.

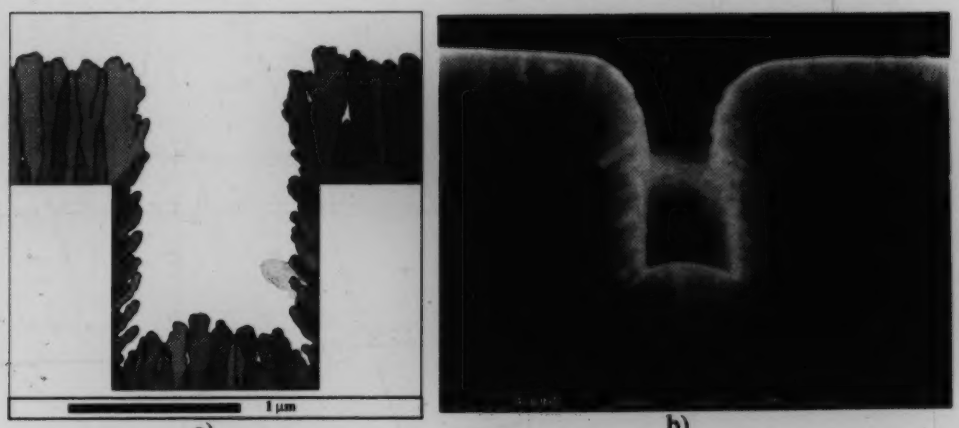

Figure 4.11 Tungsten deposition into a 1:1 aspect ratio trench. a) is the GROFILMS simulation and b) is an experimental SEM.

From this result, one can determine the sidewall coverage to be 0.2 and the bottom coverage to be approximately 0.5 (see p. 17 for coverage definitions). The microstructure is composed of porous columns with the sidewall columns oriented toward the incoming flux. The porous microstructure along the sidewalls may determine reliability of the film as a barrier layer. Figure 4.11 b) is an experimentally obtained SEM [54] with a sidewall coverage of 0.4 and bottom coverage of 0.55.

Another practical example presented in Figure 4.12 is the deposition of a very thin tantalum layer (50 nm) into a 0.35 μm 2:1 aspect ratio trench. This type of tantalum thin film is used as a wetting/barrier layer for copper metallization. The simulation results show that for the particular system configuration (1 mTorr, 30 cm target-substrate separation) generates a film that may not be suitable for metallization as there are locations where the sidewall coverage is very low and the microstructure is highly granular (shown in the increased magnification of Figure 4.12 b))

Within the regime of thin film growth where flux shadowing dominates, the impinging flux of a PVD system is important in determining the structure and morphology properties of a thin film. This thin film growth regime is modeled by GROFILMS. In particular, the effects of oblique angle deposition and low surface mobility on the growth of the thin film microstructure are examined by modeling the deposition of porous MgF_2.

Experimentally, the deposition of extremely porous MgF_2 [68] is accomplished by

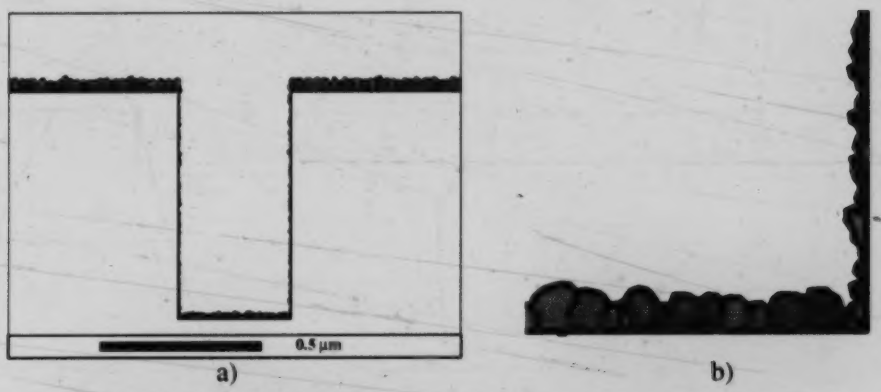

Figure 4.12 a) Ta deposition into .35 micron 2:1 aspect ratio trench for use as a Cu metallization barrier layer. b) Magnified view of the bottom right corner showing microstructure.

the complete control over the direction of the incoming flux. The incoming flux arrives at the substrate at a highly oblique angle ($\theta = 85°$) accentuating the shadowing effects of the film microstructure. The system is kept in this state to create the columnar structures oriented toward the source. After a predetermined time, the position of the source of the incoming flux is switched to the symmetric angle ($\theta = -85°$). Once again, the system creates columnar structures oriented toward the flux.

The deposition of MgF_2 via evaporation does not impart much thermal energy to the surface adatoms. This, along with the bonding of the two chemical species, results in very little surface diffusion of the adatoms. Given that the spread in the flux distribution is small due to the significant distance between target and substrate within the evaporator, the columnar structures grow according to the location of the source.

A scanning electron micrograph (SEM) of the deposited film is presented in Figure 4.13 (a). The microstructure has a convincingly *zigzagular* structure reflecting the time varying location of the evaporated source. Simulation results by GROFILMS (Figure 4.13 b)) indicate that the dominant growth mechanism determining the unique film structure is the shadowing effect of the ballistic flux in conjunction with minimal surface diffusion. Also the comparison of experimental and simulation results provided verification of the ballistic shadowing capabilities of GROFILMS.

The unique characteristics and properties of the *GLAD* films offer a range of possible applications including chiral optics, polarizers, and catalytic surfaces. Successful predic-

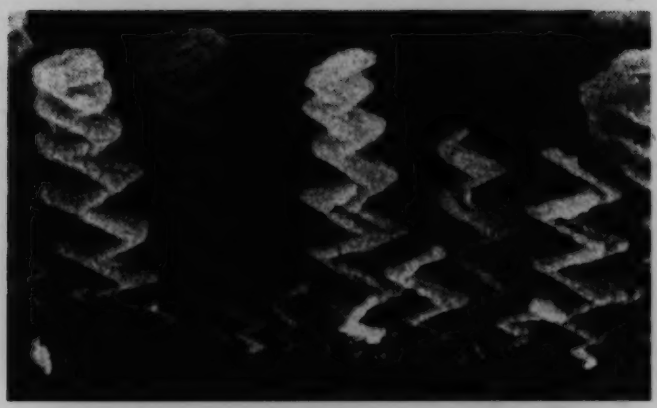

(a)

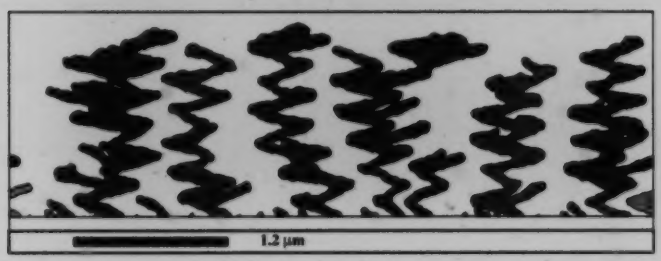

(b)

Figure 4.13 Unique microstructure of MgF_2 films as formed by exploiting the self-shadowing mechanism of the incoming ballistic flux. The height of the MgF_2 is approximately 1.2 μm. A time-varying incident angle deposition results in the *zigzagular* structure as noted in both the experimental SEM [68] (a) and the GROFILMS simulation (b).The simulation confirms the significance of the self-shadowing mechanism involved during film growth.

tion of the film properties via computer simulation can aid in complicated designs and experiments.

Chapter 5 Copper Reflow for Damascene Processing

Chapter 1 discusses the challenges of fabricating interconnections for ULSI circuits. One particular development was the introduction of copper (Cu) as an alternative metal to the traditionally used aluminum. Cu's main advantages, as outlined beginning on p. 7, are its increased reliability and interconnect performance. Though thin films of Cu can be deposited by PVD, CVD and electrochemical methods, the patterning of Cu interconnect lines suitable for ULSI is difficult. Damascene processing, again introduced in Chapter 1, is one proposed solution to the problems associated with Cu interconnection patterning. This chapter will present an in-depth simulation study of the Cu reflow stage (the filling of the trenches and vias) of the damascene process.

5.1 Cu Sputter Reflow Parameters.

It is important that the fabrication engineer fully understand the adjustable parameters that describe each step of the process such that the process can be developed and optimized. The processing parameters related to copper reflow fall under the two separate processes of copper film deposition and subsequent anneal. Table 5.1 lists the adjustable parameters, the process to which they belong, and the simulation using the parameter to model the process. The simulators SIMSPUD and GROFILMS can reduce the time and cost of process development by preparing a complete design of experiments using the parameters listed in Table 5.1.

The GROFILMS thin film process simulator is used in an extensive study of the copper reflow process. The first step of this study is to collect a database of all the relevant physical quantities. For the most part, these quantities can be found in the literature. The physical properties, their values and the references in which they were found are tabulated in Table 5.2.

Table 5.1: Processing parameters available during copper reflow and the corresponding simulation.

Parameter	Process	Simulation
Gas pressure	Deposition	SIMSPUD
Target diameter	Deposition	SIMSPUD
Target-substrate distance	Deposition	SIMSPUD
Power	Deposition	SIMSPUD
Film thickness	Deposition	GROFILMS
Topography	Deposition	GROFILMS
Underlayer Material	Deposition/Anneal	GROFILMS
Temperature	Deposition/Anneal	GROFILMS
Time	Anneal	GROFILMS

Table 5.2: The physical parameters used in the GROFILMS simulations.

Physical Parameter	Symbol	Value	Reference:
Cu surface diffusion activation energy	E_a	0.83 eV	[97]
Cu grain boundary migration activation energy	$E_{a\,gb}$	0.42 eV	a
Cu surface energy	γ_{vf}	1.78 J/m^2	[98]
Cu grain boundary energy	γ_{gb}	0.625 J/m^2	[98]
Cu/Ta interfacial energy	γ_{sf}	0.477 J/m^2	[99]
Ta surface energy	γ_{sv}	2.15 J/m^2	[99]
Cu/W interfacial energy	γ_{sf}	1.52 J/m^2	[99]
W surface energy	γ_{sv}	2.4 J/m^2	[99]

a. The value of 0.42 eV is approximately one half of the surface self-diffusion activation energy. Subsequent literature searches revealed a value of 1.1 eV would better approximate the actual grain boundary migration activation energy [90].

Two particularly important parameters are the pre-exponential coefficients, D_0, of the diffusion coefficients in equations (2.15) and (2.19). The values for the D_0's were determined by matching the required simulation time for complete reflow to that found experi-

mentally. The grain boundary migration diffusion coefficient was chosen to produce sufficient grain boundary motion, such that the microstructure tended to equilibrium configurations. The disagreement between the grain boundary migration values is not a concern as experimentally determined values can vary widely over orders of magnitude, depending upon measurement techniques, experimental conditions and type of grain boundary. Table 5.3 lists the simulation and reported values for the diffusion coefficients.

Table 5.3: The pre-exponential diffusion coefficients.

Physical Parameter	Symbol	GROFILMS Value	Reported Values	Ref:
Surface diffusion coefficient	D_0	0.1 cm^2/sec	0.1 - 2.6 cm^2/sec	[100]
Grain boundary migration diffusion coefficient	D_{0gb}	10^{-3} cm^2/sec	10^{-5} cm^2/sec	[101]

The feature scale flux distribution is dependent upon the deposition system and process parameters (pressure, power, geometry). There are two sources for flux distribution data suitable for the GROFILMS simulator. One is obtained from pin-hole experiments. The pin-hole experiments allow sputtered flux through a small aperture to impinge upon a substrate underneath as demonstrated in the schematic diagram of Figure 5.1. The film deposited on the substrate will exhibit a thickness profile characteristic of the impinging flux. Experimentally obtained flux angular distribution, presented in Figure 5.2, was provided by D. S. Gardner at Intel Components Research laboratories in Santa Clara, CA. This distribution describes the Cu sputtering process used by Gardner to deposit the experimental results in this thesis.

A second source for feature-scale flux distributions is the SIMSPUD simulator. SIMSPUD is described in detail on p. 18 and requires the input parameters as listed in Table 5.1. Two flux distributions are generated by SIMSPUD for use in this thesis. These distributions are the results of simulating a long throw (30 cm. target-to-substrate separation) and short throw (10 cm. target-to-substrate separation) Cu sputter process in 1 mTorr Ar. The generated profiles are shown in Figure 5.3 and show a much narrower distribution for the long throw system (solid line) than that of the short throw system (dotted line).

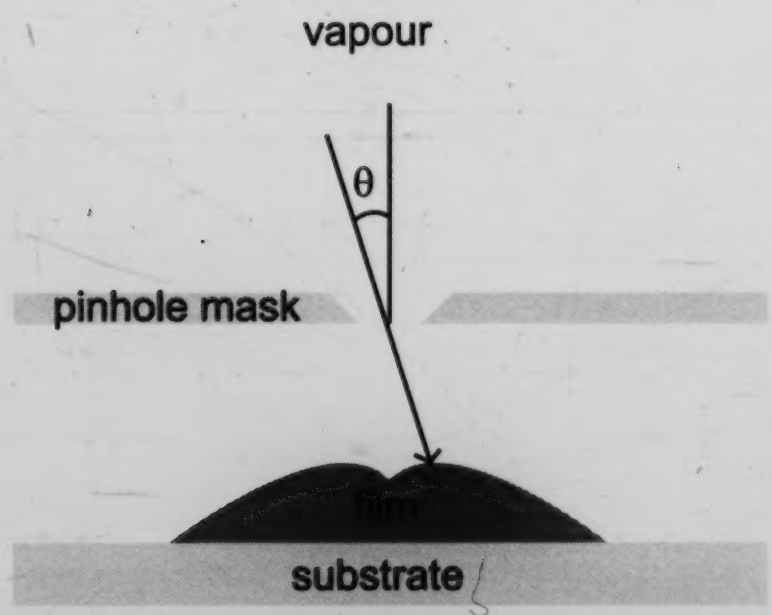

Figure 5.1 Schematic diagram of the pinhole experiment used to obtain the system-dependent incoming flux distribution. The exaggerated deposited film profile reflects the incoming flux at the pinhole.

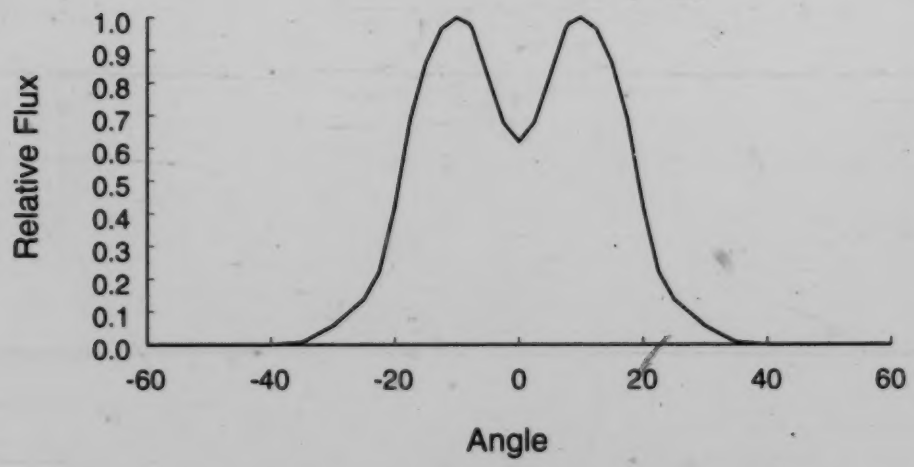

Figure 5.2 Flux distribution profile as obtained by pin-hole flux experiments on the sputter deposition system used for the experimental results of this chapter.

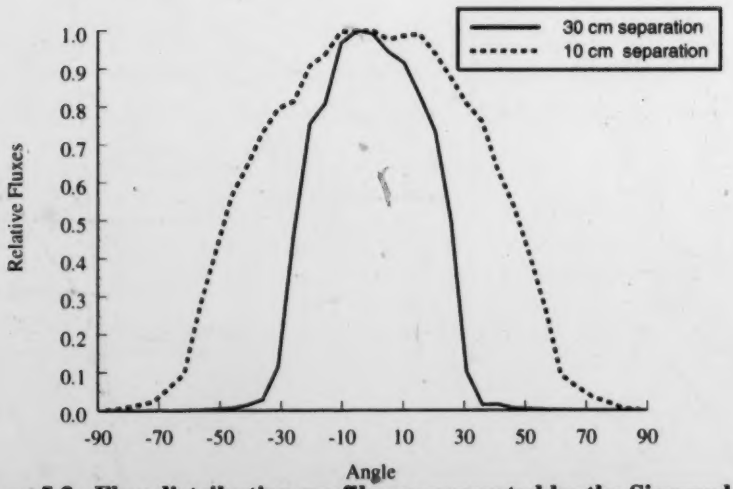

Figure 5.3 Flux distribution profiles as generated by the Simspud simulator. The two systems simulated were Cu sputtering in 1 mTorr Ar with substrate to target separation of 30 cm (solid line) and 10 cm. (dotted line).

5.1.1 Copper Reflow: Experiment and Simulation

The experimental results in this chapter were provided by D. S. Gardner at Intel Components Research. The topography used in the reflow experiments consists of trenches and vias patterned into SiO_2. A 30 nm tantalum (Ta) underlayer was initially deposited to provide a good wetting/adhesion layer for the Cu film (see p. 76). The sputter deposition system attained high sputtering rates of greater than 2 μm/min at a true ultra-high vacuum with base pressures of about 10^{-9} Pa (10^{-11} Torr). The very low base pressure minimizes the amount of contamination on the copper surface. The reflow process involved the deposition of copper followed by an anneal without exposure to air.

The first stage of a Cu reflow process is the deposition of a thin film of Cu over the topography. Figure 5.4 a) is a scanning electron micrograph (SEM) of the as-deposited Cu on a 0.35 μm wide 2:1 aspect ratio trench. Apparent in this figure are the Ta underlayer, the significant Cu film thickness (> 1.0 μm), the low sidewall coverage and the bottom coverage. This film was subsequently annealed during the second stage of the process. Anneal temperature was held at 450°C for 25 minutes. Figure 5.4 b) shows the resulting film profile. In this case, the trench was completely filled and the film was nearly planarized. The

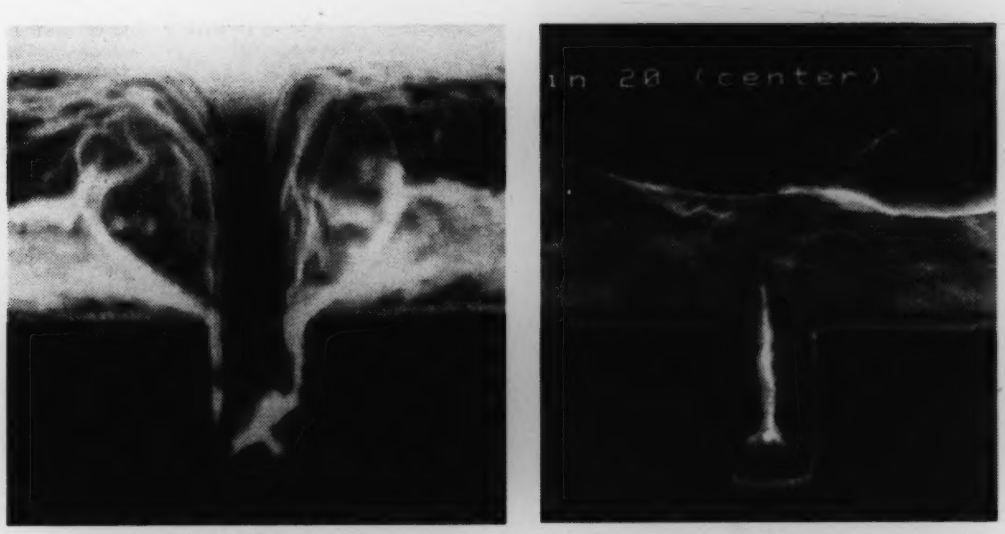

a) b)

Figure 5.4 a) Copper deposition over 0.35 μm (aspect ratio 2:1) topography. b) The resulting filled topography after the annealing procedure.

next phase in damascene processing is the chemical mechanical polishing (CMP) process which is used to eliminate all the Cu except that within the trench.

The initial GROFILMS simulation of the Cu deposition is depicted in Figure 5.5 a). The Cu is deposited onto a Ta underlayer as in the experiments. The resulting profile of the simulated Cu film deposition is in excellent agreement with the experimental SEM of Figure 5.4 a). The sidewall and bottom coverages are measured and listed in Table 5.4. There is good agreement of these quantitative values between experiment and simulation.

Setting the temperature to 450°C and simulating reflow for ~20 minutes results in the profile in Figure 5.5 b). The simulation indicates that the present process conditions will result in a completely filled trench suitable for CMP planarization. Comparison to Figure 5.4 b) indicates there is excellent agreement between the GROFILMS simulation and experiment.

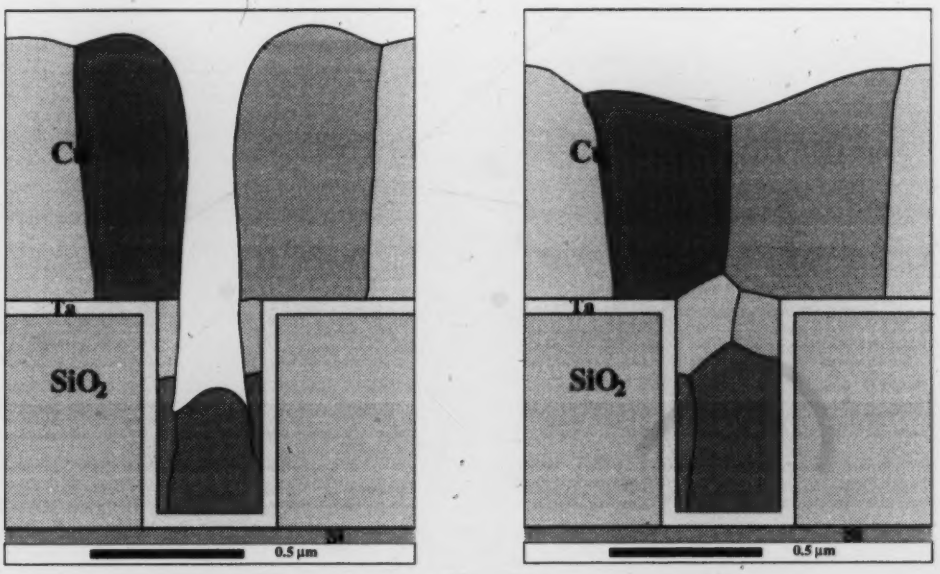

a) b)

Figure 5.5 a) GROFILMS simulation of the as-deposited copper. b) Simulation results of copper reflow agree well with Figure 5.4 b).

Table 5.4: Cu film profile properties for experiment and simulation results of Figure 5.4 (a) and Figure 5.5 (a) respectively (see p. 17 for coverage definitions).

	Experiment	Simulation
Bottom Coverage	0.44	0.45
Sidewall Coverage	0.05	0.04

5.1.2 GROFILMS analysis of the reflow parameters

A comprehensive study into the adjustable parameters of the reflow process is possible with the GROFILMS/SIMSPUD simulators. Primary goals in such a study is determining success of a particular process and for the optimization of the processing parameters. The list of parameters in Table 5.1 are under examination in this section.

The processing parameters associated with the annealing process are temperature and time. These two parameters are related as the reflow time will depend upon temperature. This dependence is due to the Arrhenius dependence of the diffusion coefficient on temper-

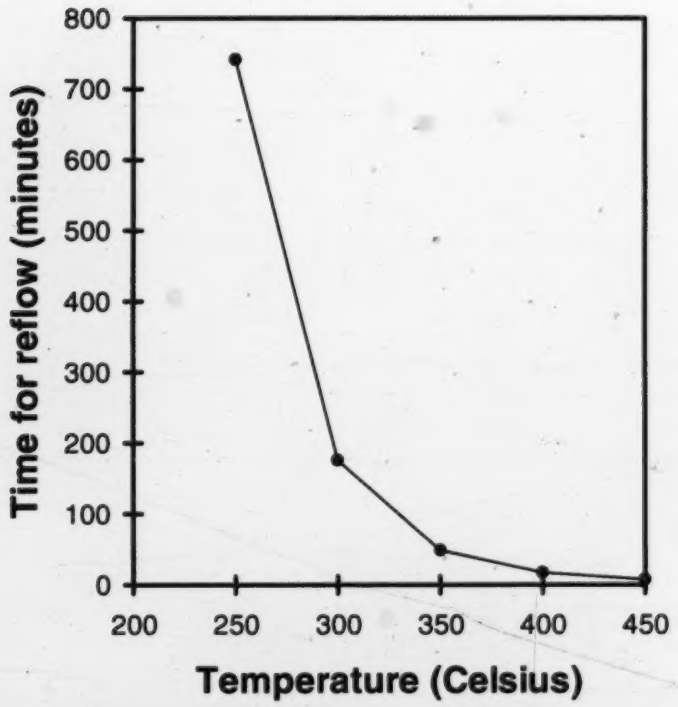

Figure 5.6 Absolute reflow times versus the anneal temperature. The exponential dependence of the surface diffusion on inverse temperature creates a strong temperature dependence of reflow time.

ature and is made explicit in equation (2.15).

Figure 5.6 shows a graph of the time required for complete reflow of the 1.25 μm Cu film over 0.35 μm 2:1 aspect ratio topography versus the anneal temperature. The criteria for complete reflow in this study is when the trench is completely filled, the Cu film is nearly planarized and the film is suitable for subsequent chemical mechanical polish (CMP) processing. Successful reflow occurs for each temperature in the range from 250°C to 450°C. The required times, however, range from an acceptable 13 - 14 minutes at 450°C to just under 12.5 hours at 250°C. The higher temperatures, however, may not be practical due to material incompatibilities and constraints on dopant diffusion in the devices. Thus, these processing parameters must be chosen to account for the trade-off between the lower temperatures and the longer anneal times.

An optimizable process parameter is the thickness of the initially deposited Cu film.

Thus, for a specific topographical feature (the same trench topography used in the previous sections: 0.35μm wide with a 2:1 aspect ratio shown in Figure 5.5), a series of simulation experiments is used to optimize the thickness of the Cu film for various reflow temperatures. The required anneal times were collected for a range of Cu film thicknesses and anneal temperatures.

The Cu was deposited at thicknesses ranging from 0.75 μm to 1.375 μm, and each deposition was annealed at temperatures ranging from 250°C to 450°C in 50°C increments. Simulation results indicated that a Cu film 0.65 μm thick was insufficient to guarantee a successful reflow of Cu as the underlayer (tantalum) was exposed and trench filling halted. A 1.5 μm Cu film was too thick as the Cu film capped the trench thus forming a void. An end point for each successful reflow process simulation was chosen such that the Cu film just filled the trench and was suitable for CMP (i.e. not to complete planarization but with complete trench filling).

Figure 5.7 is a graph presenting the reflow completion times for each GROFILMS simulation normalized to the time taken with an initial Cu thickness of 0.75 μm. These results show that as Cu film thickness increases from 0.75 μm, there is a general trend for the reflow times to decrease until the initial Cu film reaches 1.125 μm. The graph shows that the required reflow times at the 400°C and 450°C anneal temperatures continue to decrease until the initial film thickness is 1.25 μm. At this point, the reflow time is approximately 63% and 69%, respectively, of a 0.75 μm deposition. Under these specific system conditions and topography, a reduction of the anneal times by 20 - 25% for a given temperature can be achieved by proper choice of deposition thickness. While these trends are expected to be general, the optimum found here is, of course, specific to the conditions examined. Other topographies and sputter systems will require similar simulation studies to optimize.

The initial dramatic decrease in reflow times with increasing film thickness can be explained by the increased amount of copper within the trench resulting from the deposition. Less Cu is required to completely fill the trench, thus reducing the necessary anneal time. Furthermore, as the film becomes thicker, the gap within the trench becomes smaller thereby accentuating the curvature of the Cu surface. This increased curvature provides a stronger driving force for the surface diffusion thus enhancing the transport of Cu during the anneal process.

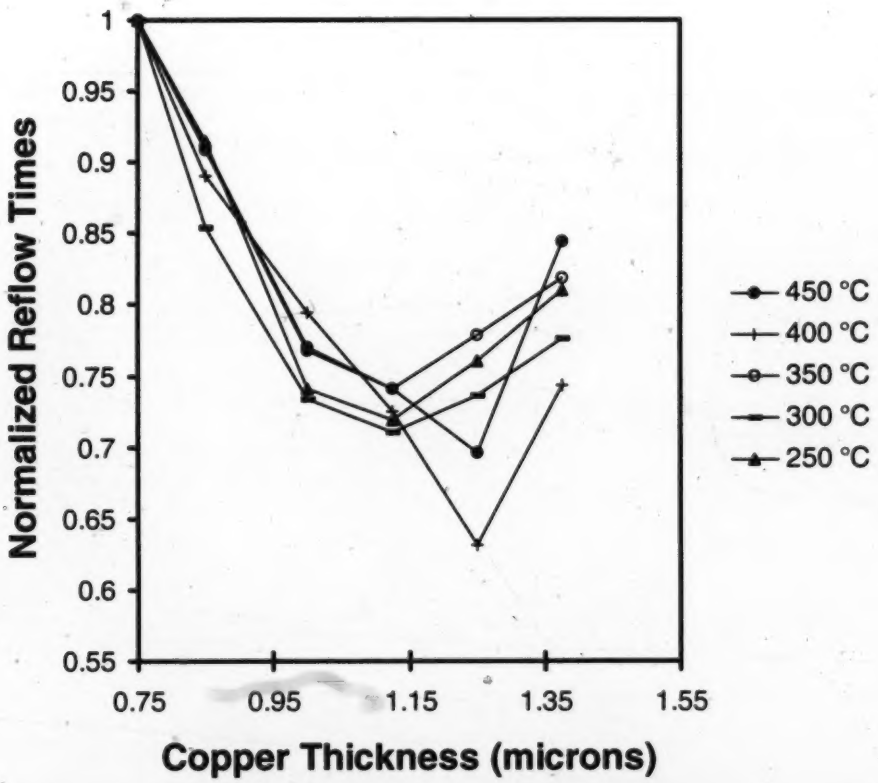

Figure 5.7 Normalized reflow times versus film thickness for various annealing temperatures (250°C to 450°C). The required reflow times (normalized to time required with 0.75 μm Cu) drop approximately 65% at 1.25 μm beyond which an increase occurs.

As the thickness of the deposited Cu film is increased, a point is reached whereby there is very little additional flux reaching the bottom of the trench. This is a direct result of ballistic shadowing by the sidewalls of the Cu at the trench. The trenches are nearly closed off for Cu thicknesses greater that 1.0 μm. The Cu at the bottom reaches a maximum and no longer contributes to the decrease in reflow times. Also, as the Cu thickness increases, the sidewalls become higher and possess less curvature. As the sidewalls offer a long flat surface, there is little driving force for the Cu to diffuse down into the trench. There exists a concave curvature at the bottom of the trench which drives the initial diffusion and fills the bottom of the trench with Cu from the sidewalls; however replacement Cu is slower to arrive due to the lack of surface curvature along the sidewalls.

Other processing parameters that can be varied in order to optimize the reflow process include the deposition system parameters such as chamber geometry. Careful control over these parameters can enable a tailored deposition of the initial copper film. For example, bottom coverage improvement was obtained by low pressure deposition, a process which narrows the flux distribution allowing for better filling [102].

Using the SIMSPUD and GROFILMS simulations, the effects various system parameters have on the reflow process can be studied. Two deposition systems are studied. The first is a "long throw" system with the target 30 cm from the substrate with 1 mTorr Ar deposition pressure. For comparison, a short throw system with a target to substrate separation of 10 cm was simulated (flux distributions generated by SIMSPUD for these two systems are presented in Figure 5.3). The long throw deposition simulation (Figure 5.8 a)) shows a tendency for much more initial bottom coverage than that deposited in the short throw system (Figure 5.9 a)). The short throw simulation (Figure 5.9 a)) reveals a larger voided region within the trench that will require more time to fill. Poor sidewall coverage may also result in failure due to discontinuous surface coverage during reflow.

The deposition simulations of Figure 5.8 a) and Figure 5.9 a) were reflowed at 450°C for 15 minutes to yield Figures 5.8 b) and Figure 5.9 b) respectively. The results show that the extent of filling is far greater for the long throw deposition process under identical reflow conditions: $t_L > t_S$ as labelled in the figures. However, longer deposition times are required when metals are deposited by a long throw system [103]; thus, process design must consider the trade-offs between the longer deposition time for long throw deposition and the extended reflow times required for the short throw deposition.

Other deposition variants, such as collimation or ionized sputtering, which also increase initial bottom coverage, will similarly reduce reflow times and increase reliability as long as adequate sidewall coverage is maintained.

For a particular topography, a deposition system may or may not be suitable to deposit Cu films that will lead to a successful reflow process. One possible failure mode resulting from the initial Cu deposition profile is the bridging of the trenches. Bridging can occur either during the deposition or the annealing procedure with either ultimately resulting in a voided region within the trench.

As an example of this type of system analysis, Figure 5.10 a) shows an initial depo-

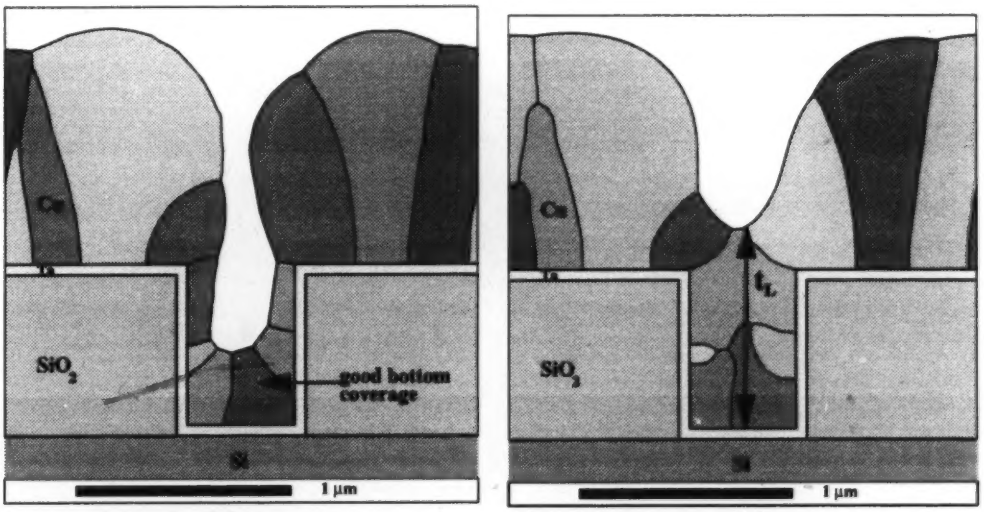

Figure 5.8 Long throw (30 cm) sputtering a) as-deposited and b) after a 15 minute anneal. Anneal temperature was 450°C.

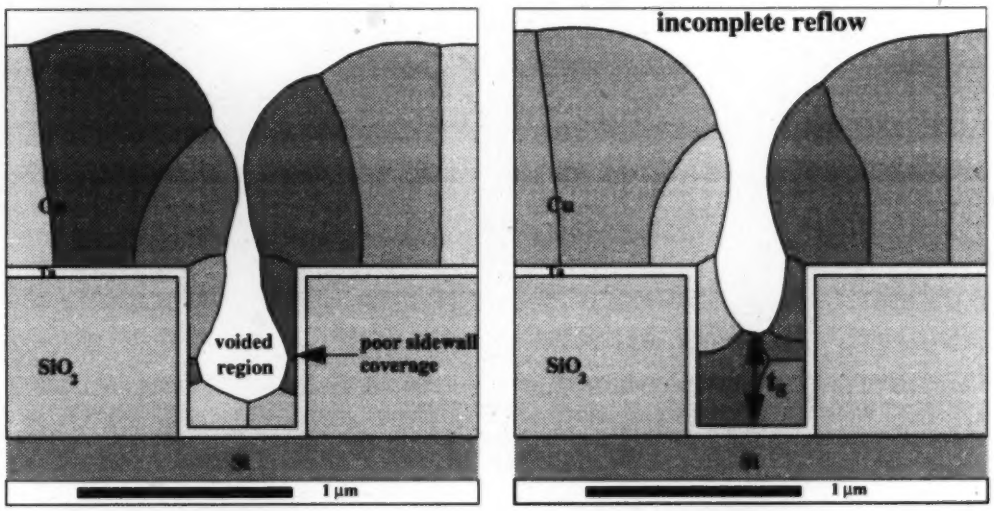

Figure 5.9 Short throw (5 cm) sputtering a) as deposited and b) after a 15 minute anneal. Anneal temperature was 450°C.

sition profile of Cu on a Ta underlayer in a short throw deposition chamber as in Figure 5.9. There appears to be sufficient Cu to fill the trench; however, after an anneal at 450°C, the resulting profile (Figure 5.10 b)) shows the trench was bridged by the Cu film. The bridging was a direct result of the lateral motion of the copper film surface at the onset of the anneal.

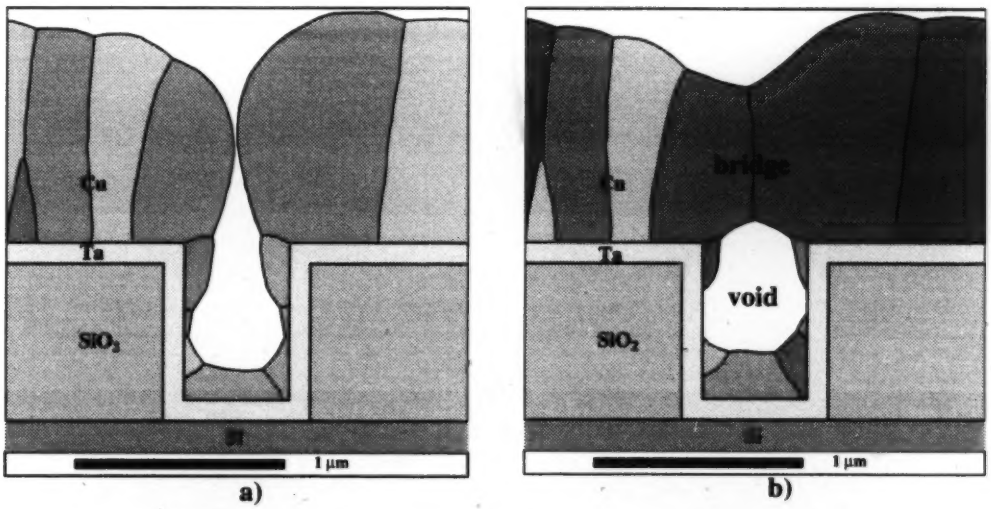

Figure 5.10 Bridging or capping of the trench may occur during deposition or during the reflow process. The short throw as-deposited Cu film on Ta (a) is reflowed in b). During reflow, the film above the trench closes off resulting in the formation of a void within the trench. This particular simulation also dewetted along the sidewalls.

Subsequent annealing will tend to minimize the overall free energy of the exposed surfaces. Thus the voided region within the trench will, in the absence of facetting, evolve from a keyhole shape to a circle which intrinsically has a lower total surface free energy. In this example, the diffusion of Cu exposed the sidewalls.

The reflow simulations of Figure 5.10 and that of Figure 5.9 were produced by the same deposition and anneal conditions. The fact that the reflow simulation of Figure 5.9 did not bridge over and Figure 5.10 did, can be attributed to the randomness of the process. One can conclude that this particular reflow process will succeed some of the time; however, uniform success across an entire wafer cannot be expected.

If complete bridging over the trench occurs, filling is no longer possible via surface diffusion alone. Volume diffusion or grain boundary diffusion of the copper must be relied upon to fill the voided region. These processes are, however, quite slow, and complete reflow would most likely require temperatures higher than that required for the process driven by surface diffusion. Thus, capping or bridging of the trench is wholly undesirable.

One can therefore make the assumption that the Cu films deposited in the short throw chamber may result in a successful reflow as in Figure 5.9. However, the results of Figure

5.10 indicate that the probability of complete success over an entire substrate is not very high. Thus, using this chamber geometry would not be suitable in production.

The GROFILMS simulations are two dimensional and this must be taken into consideration when making predictions of film behaviour. Though failure modes may be predicted by GROFILMS, there is the possibility that Cu from within the trench can be transported along the trench to the voided regions. For instance, if the trench is bridged in a single isolated location and reflow is allowed to continue throughout the rest of the trench, a surface curvature will evolve along the length of the trench. This curvature will transport material under the bridge and serve to fill the void. Likewise for the exposed underlayers due to the dewetting of Cu; material may be supplied by the filling along the trench length. However, the prediction of failure even in localized areas is cause for concern over a wafer with millions of critical trenches and vias.

5.2 Substrate Considerations

A variety of topographical features with different sizes and shapes can exist concurrently on a single substrate. For example, the vias and trenches with various aspect ratios fabricated by damascene processing must be reliably filled. Furthermore, the material upon which the Cu is deposited (the diffusion/adhesion/underlayer) will affect processing. Thus, substrate material and feature scale geometry are important considerations when developing a reflow process.

5.2.1 Multiple feature sizes

A particular deposition process may consistently result in a successful reflow for a certain topography; however, it may not work for a second topography. The GROFILMS simulation was used to study multiple topographies within a single simulation. An initial topography of two parallel trenches (one 0.35 μm 2:1 trench (A) and a 0.25 μm 2:1 trench (B) as shown in Figure 5.11) was selected, and three separate processes were developed and performed on the test topography.

The first simulated deposition used the angular flux distribution obtained by pinhole experiments of the system used to deposit the experimental results in this thesis (Figure 5.2 on p. 82). The copper was deposited to approximately 1.3 μm thick (shown in Figure 5.11

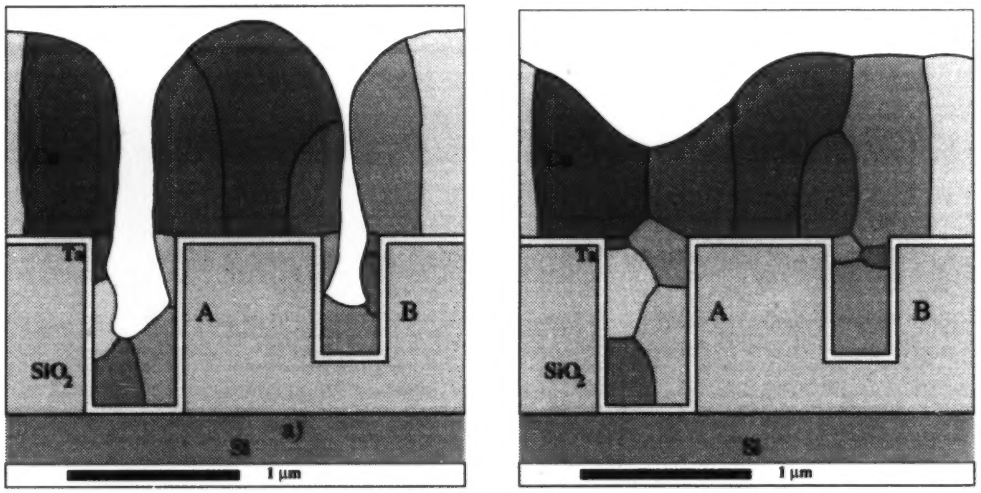

a) b)

Figure 5.11 a) An as deposited Cu profile over two trenches of different feature sizes. Deposition conditions emulate the experimental system detailed in this thesis. b) Successful reflow filling both trenches after a 15 minute anneal at 450°C.

a)) and reflowed at 450°C for about 15 minutes. The results are presented in Figure 5.11 b) and show both trenches were completely filled.

The second deposition process uses the angular flux distribution as obtained by SIMSPUD to represent the short throw system and deposition parameters (flux profile shown in Figure 5.3). The as-deposited film is presented in Figure 5.12 a). The reflow simulation results (Figure 5.12 b)) show, however, that this initial Cu deposition will not lead to successful filling of topography B. The Cu film bridged over the trench and a void was formed within the trench.

The third deposition process uses a flux distribution characteristic of a long throw system (flux profile shown in Figure 5.3). The film thickness of the as-deposited film (Figure 5.13 a)) is less; thus requiring a reduced deposition time. Figure 5.13 b) reveals that the reflow process would fill topography B but that there would be insufficient Cu to fill topography A.

The failure of the sputter reflow of copper in one topographical feature is not acceptable for a production process. Thus, when developing the process, all the topographies present on the substrate must be considered collectively.

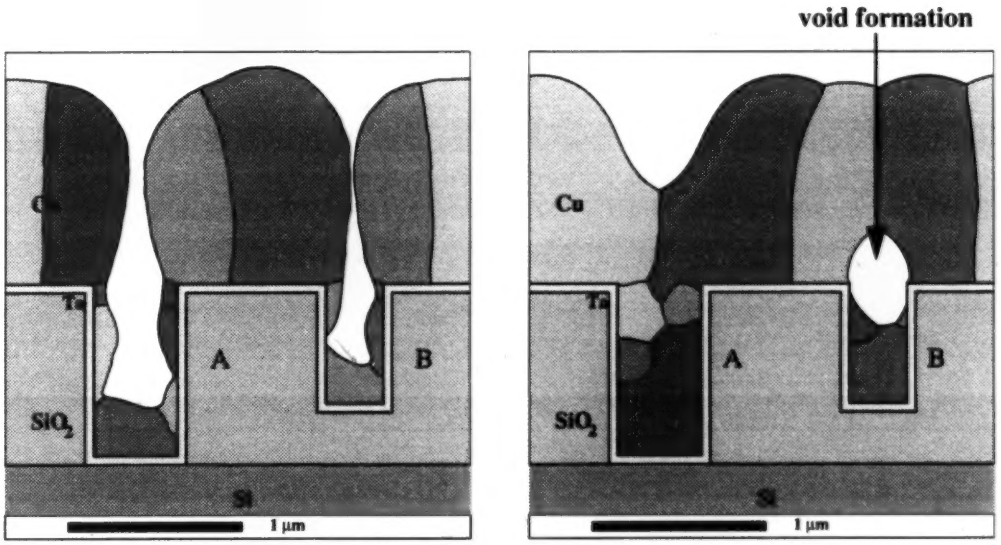

Figure 5.12 a) Cu profile deposited in a system with 10 cm target to substrate distance. b) Reflow simulation shows that the larger trench fills successfully but the smaller one forms a void.

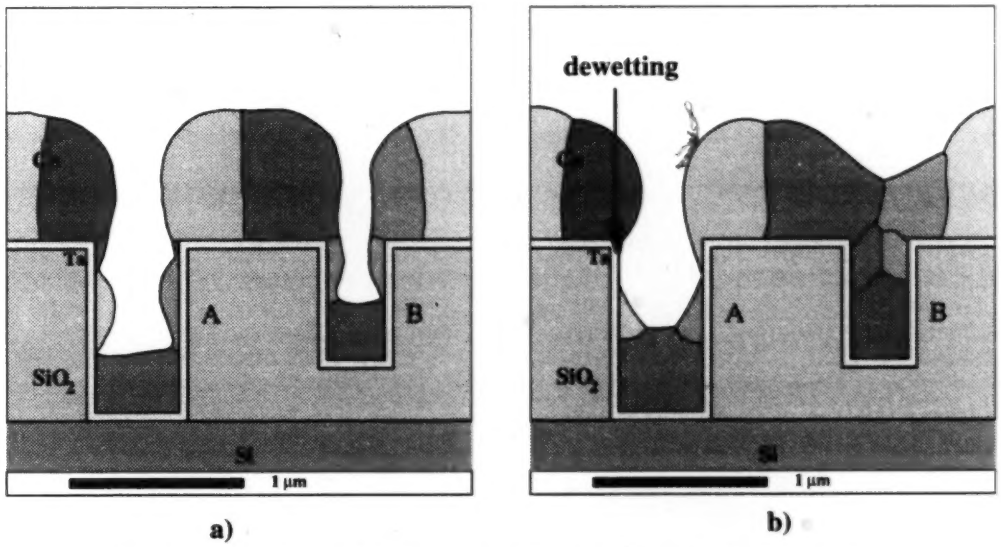

Figure 5.13 a) Cu profile deposited in a system with 30 cm target to substrate separation (long throw). b) Reflow simulation shows that the smaller trench fills successfully but there was insufficient material for the larger one to fill.

5.2.2 Underlayer material

The wetting behaviour (determined by interfacial energetics) of Cu films deposited upon different adhesion/barrier layers will greatly influence the as-deposited film profile and film microstructure. The Cu film may completely wet the surface resulting in continuous coverage, or agglomeration may occur and result in sidewall exposure. A Ta underlayer, for example, has been established as a good wetting layer for Cu, while tungsten (W) underlayers result in poor wetting and Cu agglomeration [99]. Figure 5.14 is a GROFILMS simulation result that demonstrates how the wetting characteristics expected for Cu on W can affect step and bottom coverage.

In terms of a Cu reflow process, exposed sidewalls result in a discontinuous Cu surface that does not provide the necessary capillary driving forces for diffusion. Thus the filling of the topography is impeded. An initial profile similar to Figure 5.14 is undesirable and should be avoided by another choice of an underlayer or by tailoring the deposition process. A simulated reflow on the film of Figure 5.14 resulted in minimizing the surface curvature of each grain while establishing equilibrium grain boundary grooving and wetting angles. As the wetting angles of Cu on W are quite high, the anneal did not result in migration of Cu into the trench and consequently, the Cu that had agglomerated on the sidewalls did not make contact to the Cu at the bottom. Thus the trench did not fill and reflow was unsuccessful.

The coverage along the sidewall may be initially continuous but the step coverage may be too low such that subsequent annealing can expose the underlayer. As an example of this, the GROFILMS simulation result of Figure 5.15 demonstrates failure during the anneal process. Figure 5.15 a) is an initial deposition profile of a Cu film on W and shows complete coverage of the sidewalls. Figure 5.15 b) indicates, however, that there was insufficient sidewall material to maintain that coverage throughout the reflow process. Diffusion of Cu to the concave surface at the bottom initially removed the Cu from neighbouring sidewall regions, thus exposing the sidewalls. The wetting characteristic of Cu on the underlayer (in this case W) promoted agglomeration thereby drawing the Cu away from the exposed region. A continuous Cu surface, and thus the capillarity driving force, was no longer available for filling the trench during the remaining anneal. To prevent

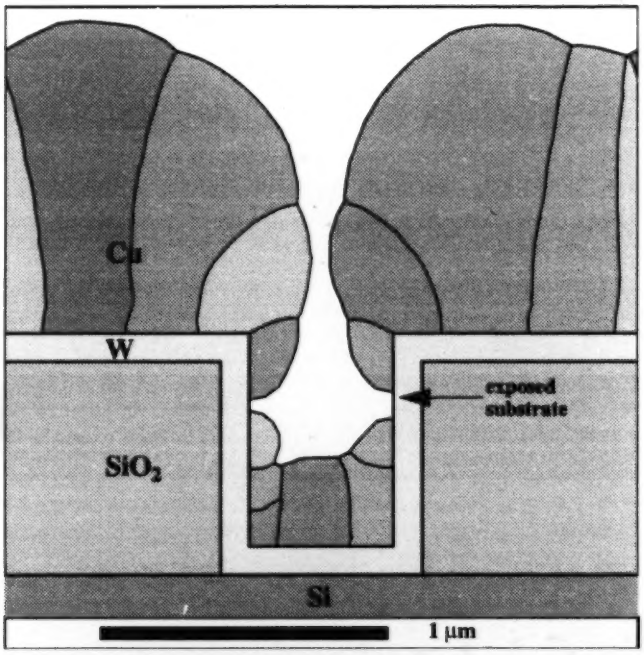

Figure 5.14 As-deposited Cu on a W underlayer. The poor wetting properties of Cu on W results in excessive Cu agglomeration on the sidewalls. Discontinuous surface diffusion paths inhibit the reflow process.

the dewetting of Cu during reflow, sufficient Cu (from above the ILD) is required. This condition must be provided by proper development of the deposition process.

5.2.3 Copper reflow into via structures

Via structures are for interconnection between metallization levels and for contact to devices. Process development for filling vias using the sputter reflow of copper into the vias can be facilitated using the GROFILMS simulator in quasi-three dimensional mode (as discussed on p. 59).

The sputter deposition of Cu onto the substrate with the via structures is the first step. At this point, it is useful to compare the simulation results of Cu deposition into vias with those into trenches under identical processing conditions. The flux distribution describing the Intel Cu sputter reflow system is used to generate the following simulations. Figure 5.16 presents the results of a 0.5 μm Cu deposition into a) a 0.5 μm-wide trench with aspect ratio 1:1 and b) a 0.5 μm-wide via with aspect ratio 1:1. Analysis of the simulation results show

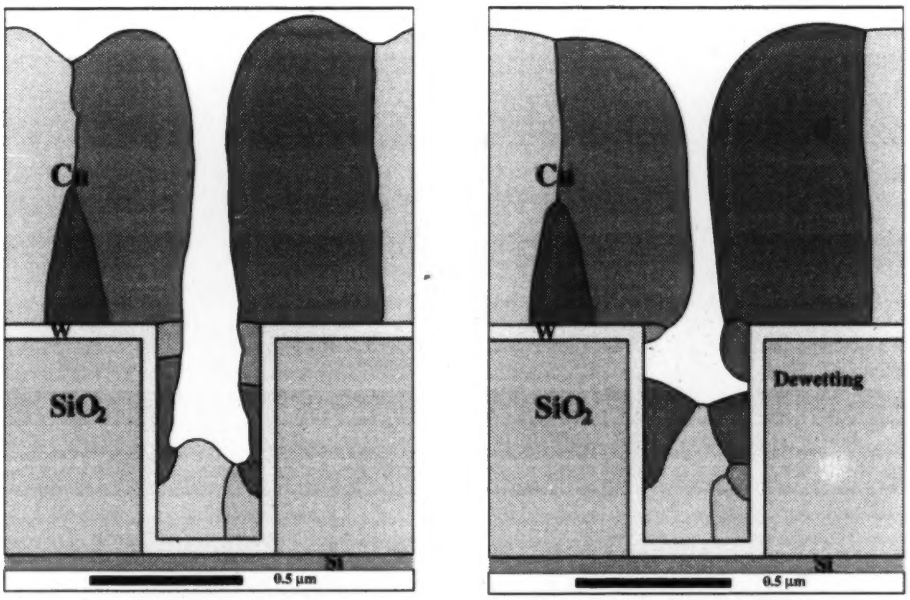

a) b)

Figure 5.15 Dewetting is a possible failure mode if sidewall coverage is insufficient to maintain a continuous surface diffusion path during reflow. The as-deposited Cu film on W (a) is reflowed. The results (b) show that dewetting has occurred.

the bottom coverage of the trench deposition to be 0.83, significantly higher than the via bottom coverage of 0.45. The sidewall coverages are 0.11 for the trench and 0.08 for the via. The poor sidewall coverage of PVD Cu in via structures has been experimentally reported to inhibit via filling [104].

Figures 5.16 c) and d) are the resulting simulated profiles after a 15 minute anneal at 450°C. The trench is completely filled while the via is capped. The capping results from the extreme out-of-plane radius of curvature (see Figure 3.14) that drives capillarity diffusion. In this case, the anneal process closes the top of the hole in the Cu film. The capping occurred in under five minutes and effectively eliminated surface diffusion paths, and thus filling halted. Subsequent annealing removed Cu from the nearby surface to thicken the cap and bring the internal void to equilibrium.

Equilibrium in this case is dominated by the presence of grain boundary grooves. The grooves allow for the existence of a global curvature to exist in the via at equilibrium. Figure 5.17 illustrates this concept by comparing the schematic diagrams of the local geometry

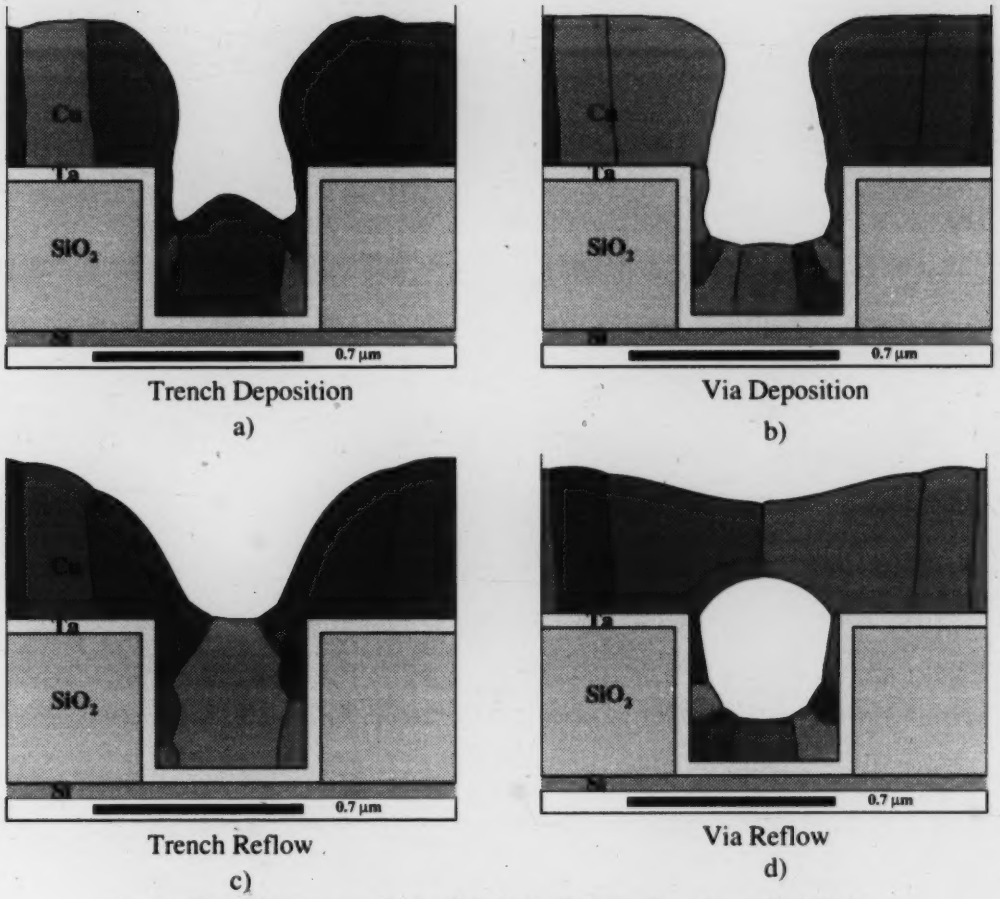

Figure 5.16 Sputter reflow of Cu into 0.5 μm deep trench and via with aspect ratio 1:1. A 0.5 μm thick Cu deposition is shown for the trench a) and the via b). Identical reflow conditions fills the trench c) and caps the via d).

of a surface with highly concave curvature with and without grain boundary grooving effects. The thin solid line represents the initial surface profile; the dotted line represents the profile after annealing.

Figure 5.17 a) considers no grain boundary grooving. Here the total free energy is lowered by relocating material from the sidewalls to the bottom thereby reducing total surface curvature. When grain boundary grooving is prominent as in Figure 5.17 b), minimization of the local free energy in the vicinity of the grain boundary results in a grooving profile. This reduces curvature on either side of the groove ($\kappa_a > \kappa_b$ in Figure 5.17). In effect, the kink introduced by the grain boundary groove appreciably reduces the gradient in

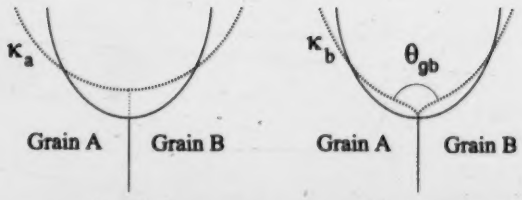

Figure 5.17 Schematic representation of the observed grain boundary grooving effects on local surface diffusion behaviour. The thin solid line is the initial profile and the thick dashed line represents the profile after annealing. a) shows the evolution of the film profile when no grooving is considered and b) when grooving is prominent.

the chemical potential of the surface thereby reducing the driving force for diffusion.

The grain boundary grooves are suspected to affect reflow of Cu into the via. Thus, a simulation is performed excluding all microstructure. The as-deposited Cu film profile into a via is presented in Figure 5.18 a). Note the lack of grains as the film is represented by its profile alone. The reflow simulation, Figure 5.18 b), successfully fills the via. There is no capping of the via as the uninhibited diffusion into the via is great enough to overcome the lateral motion of the film profile due to the out-of-plane curvature. This result is of importance as the initial Cu microstructure will determine success or failure of the reflow process. The next section discusses more of the microstructure effects on processing.

Alternative processing procedures are required to fill both trenches and vias with the sputter reflow of copper. One possible solution is to tailor the initial film profile, thickness and texture to maximize surface diffusion. Another solution could be incorporating two sputter deposition steps with the second following an anneal and CMP. This second deposition could fill the voided vias (now with the caps removed). The features to be filled would be less deep, have of a less extreme aspect ratio and have a Cu layer on which subsequent deposition occurs. A third possible solution [104] is to deposit a conformal seed layer using CVD and follow with a high temperature sputter deposition.

5.3 Microstructural Effects on Copper Reflow

The microstructure of a thin metal film is suspected to affect the uniformity of the reflow process from trench to trench [105]. A perfect example of such variation in reflow is

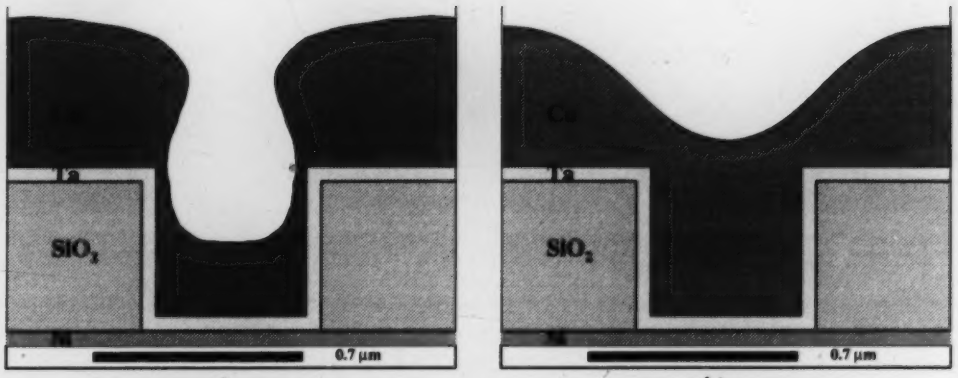

a) b)

Figure 5.18 a) A simulated deposition of Cu into a via without any microstructure. b) The simulated reflow for 20 minutes that results in successful filling due to no surface interaction with grain boundary grooves.

demonstrated in a transmission electron micrograph (TEM) of three parallel trenches of sputter reflowed copper (Figure 5.19 a)). The TEM clearly shows the random evolution of the film profiles as the two outer trenches are completely filled and the copper is somewhat planarized. However, the middle trench reveals that the reflow process has not progressed as far. A detailed look of this underfilled trench by TEM (see Figure 5.19 b) shows the preferential orientation of the copper grains, grain boundary grooving, and the internal microstructure of the film. These results lend credence to the assumption that the microstructure of the Cu film may affect reflow processing. Both TEM micrographs were supplied by D. S. Gardner at Intel Components Research.

5.3.1 Analyzing microstructure effects using GROFILMS.

GROFILMS is used to study the microstructural effects on the copper reflow process. Cu reflow is simulated over topography comprised of multiple parallel trenches similar to those of Figure 5.19. The advantage of these simulations is the ability to study the profile evolution of multiple trenches during a single process and to determine process variability due to the different fundamental phenomena of grain boundary grooving and facetting.

Figure 5.20 details the as-deposited copper in which the texture of each trench exhibits a different arrangement of grains. This configuration is created solely by the stochastic

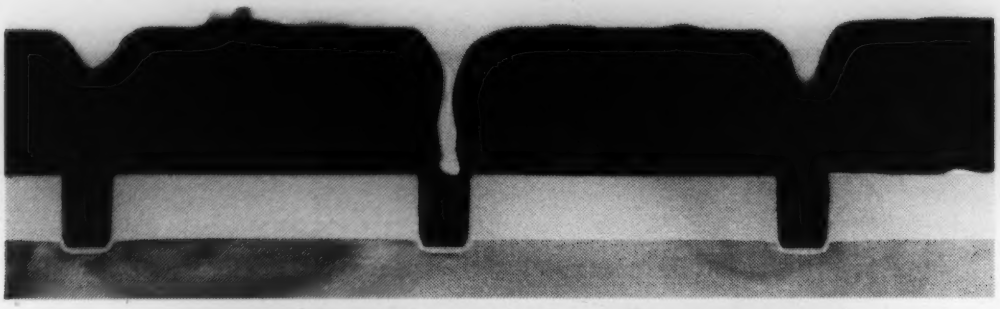

a)

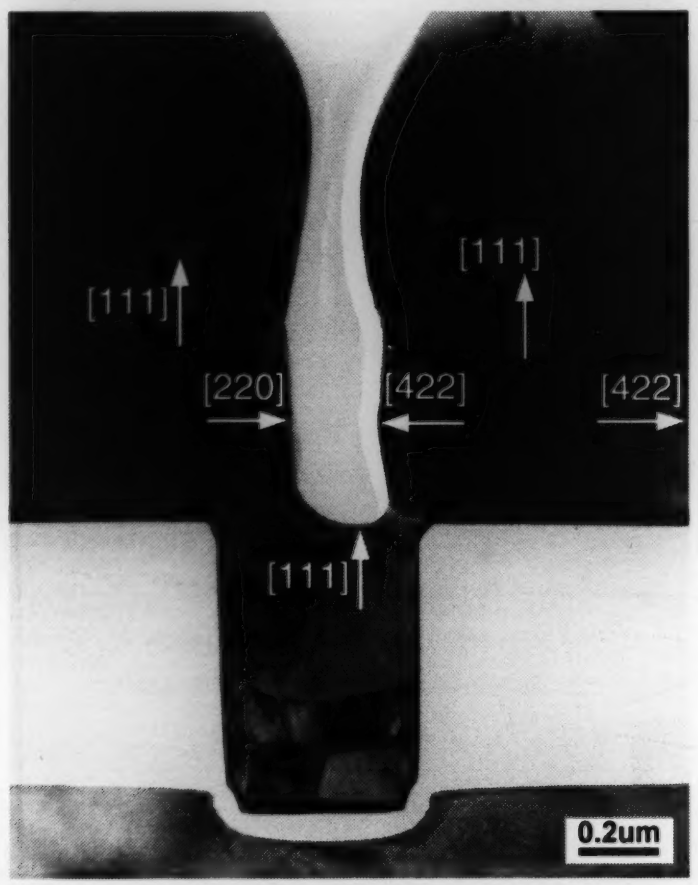

b)

Figure 5.19 a) Sputter reflow of copper on tantalum in 1.5:1 aspect ratio trenches. The three parallel trenches show various stages of reflow, illustrating the potential variability of the process. b) is a more detailed image of the middle trench of a) showing crystal orientation, grain distribution and grain boundary grooving.

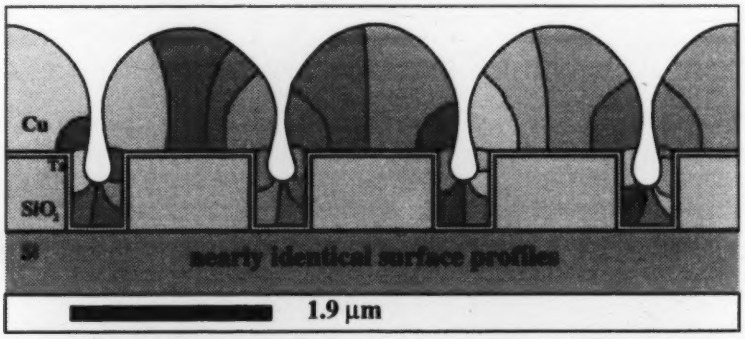

Figure 5.20 GROFILMS simulation of Cu deposition over four parallel trenches corresponding to those of Figure 5.19. This simulation incorporates no grain boundary grooving or facetting, thus the smooth nearly identical profiles within each trench. The random texture within the trenches is the only form of variability over the trenches. This simulation is used as the starting point for each of the reflow simulations of this discussion.

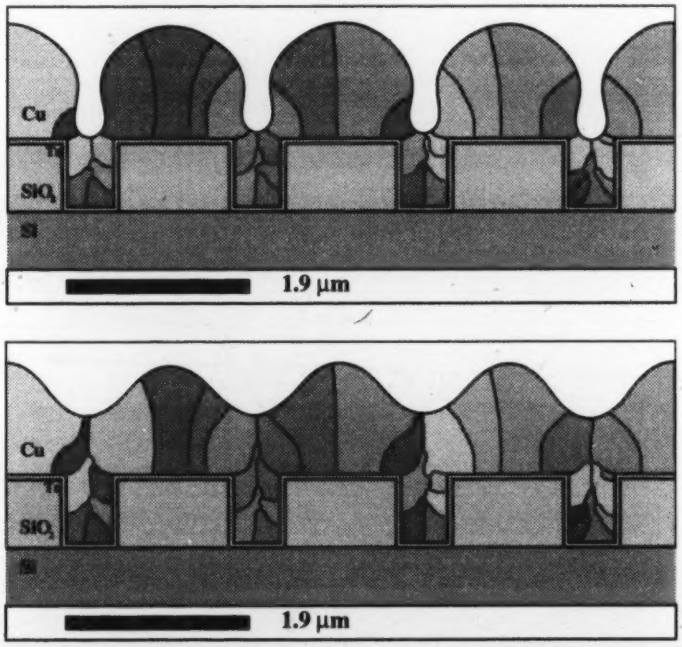

Figure 5.21 GROFILMS reflow simulations using Figure 5.20 as the starting point. These simulations do not include grain boundary grooving effects or facetting. Thus, the results exhibit a uniform surface profile in each trench. a) is annealed for 10 minutes, b) for 50 minutes at 450°C.

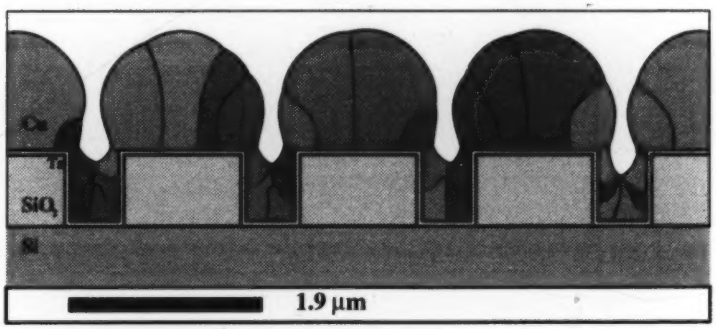

a)

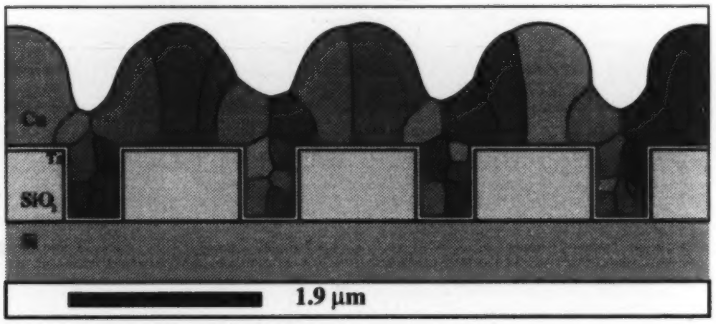

b)

Figure 5.22 Reflow simulations incorporating the grain boundary grooving phenomenon. The simulations show increased variation in surface profiles and stage of reflow between the trenches. a) is annealed for 10 minutes b) for 50 minutes at 450°C.

nature of the ballistic impingement, surface diffusion and nucleation. The surface profile is smooth as grain boundary grooving and facetting were neglected. Generally, there is little variation between the film profile of each trench. This deposition exhibits sufficient sidewall coverage to maintain a surface diffusion path throughout a reflow process. Each subsequent simulation uses this deposition profile as a starting point and simulates an anneal for 10 and 50 minutes at 450°C.

Reflow simulations that do not include facetting or grain boundary grooving (Figure 5.21 a) and b)) show very uniform filling from one trench to the next. Furthermore, the time required to completely fill each trench is the same, indicating that each trench progresses identically. Omitting the real effect of film microstructure (grooving and facetting) eliminates most of the variable nature of the reflow process from trench to trench.

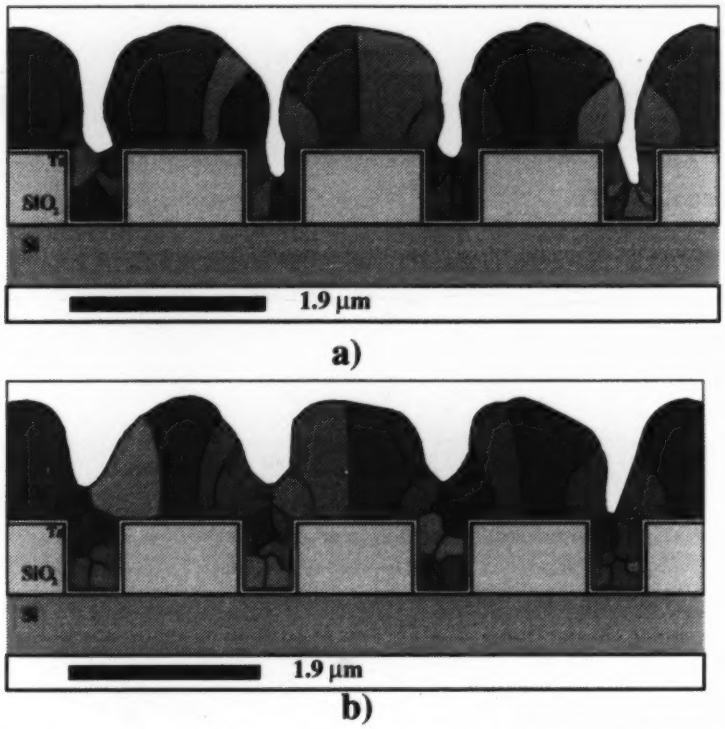

Figure 5.23 Reflow simulations of four parallel trenches including both grain boundary grooving and facetting phenomena. a) is annealed for 10 minutes, b) is annealed for 50 minutes at 450°C.

The reflow simulations of Figure 5.22 incorporate the effects of grain boundary grooving on the film profile. The figure shows that there is indeed a varied progression of filling from trench to trench solely on the basis of varying grain structures (most noticeable in the rightmost trench where there exists the most grains: 6 compared to 5 in the other trenches). Time required to fill a trench can be increased as surface diffusion is slowed where the grooving of the grains lowers the adjacent surface free energy below that expected for a continuous surface with the same curvature. For instance, while every trench is filled after a 10 minute anneal in Figure 5.21 a) (no microstructure), no trench in Figure 5.22 a) which includes the effects of grain boundary grooving has progressed to that stage.

After annealing for 50 minutes, each trench of Figure 5.22 b) is completely filled. Careful inspection of the morphology above each of the trenches reveals the same characteristic differences; a slow down in reflow progress. The profiles are similar but have definite distinct shapes unlike the profiles of Figure 5.21 b) which are nearly identical. It is

assumed that larger variations in the number of grain boundaries (grain density) affecting reflow will result in greater variation from trench to trench.

The inclusion of facetting along with grain boundary grooving into the GROFILMS simulation (Figure 5.23) shows another microstructural effect on the reflow process. Once the reflow process has begun, the facets are quickly exposed as these low energy crystal planes form the equilibrium state. GROFILMS results indicate that the surface diffusion flux is now no longer uniform over the film profile as the facets effectively resist movement off equilibrium. Once a surface normal is moved from equilibrium, there is a rush of diffusion as the next low energy configuration is sought. Thus, the time evolution of the reflow profile can be described by sporadic adjustments of the exposed facets.

Figure 5.23 a) shows an increase in the variation of the surface profile from one trench to the next. Definite facetted surfaces have also appeared. The 50 minute anneal results, Figure 5.23 b), have filled all the trenches but as seen from the profile of the rightmost trench, the filling is far from uniform. Thus, the unique evolution of each trench is further differentiated by the facetting of the film as the microstructure is once again a key factor in the evolution of the film profile.

5.3.2 Grain boundary grooving and its effect on reflow times [106]

Grain boundary grooving is suspected to affect the surface diffusion rates during the reflow of the film within trenches and vias as discussed above. The filling rate is reduced as surface diffusion is slowed where the grooving of the grains kinks the surface and lowers the adjacent surface free energy below that expected for a surface with the same gross curvature. See the discussion on p. 98 and Figure 5.17 regarding the energetic reduction mechanisms.

A GROFILMS study has been developed to isolate and determine the effect on reflow times by varying the density of grain boundaries on the surface of the initial film profile. Initially, a Cu film profile is deposited free of any microstructure as presented in Figure 5.24. This profile is subsequently used as the starting point for arbitrarily adding microstructure. Figure 5.25 a) presents the same initial profile except with the addition of five grain boundaries. The location of each of the grain boundaries was chosen randomly; however, it will be discussed that the position of the boundaries is an important factor influenc-

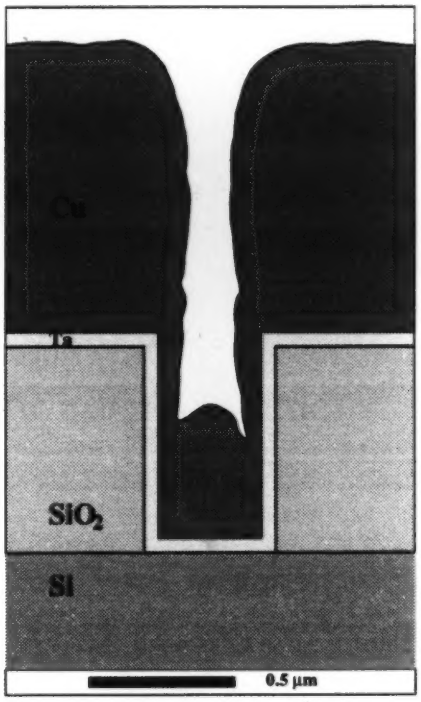

Figure 5.24 The original deposition profile without any microstructure. This simulation is used as the starting point for each of the following reflow simulations where the grain boundaries are arbitrarily added one at a time.

ing reflow times. Each new profile, with an incremental number of grain boundaries, is used to simulate reflow to a completion point (the film in the centre of the trench reaches a height, *h*, above the substrate as shown in Figure 5.25 b)). The GROFILMS simulations do not include facetting or crystal orientations.

As more grain boundaries are added into the initial profile, Figure 5.26 shows there is an increase in the time needed for the reflow to reach completion. In this figure, time to completion is shown versus the number of grain boundaries (or complexity of the microstructure). The trend of increasing times with microstructure supports the above hypothesis that the presence of grain boundaries and a grooved profile will slow down local diffusion. Furthermore, it is noted that the position of grain boundaries within topography also has a strong impact on reflow times. As the grain boundaries near the bottom of the trench are quickly buried, they contribute minimally to the slow-down of diffusion. This is evident by the levelling off of required reflow times at 15.25 minutes shown the compiled simulation

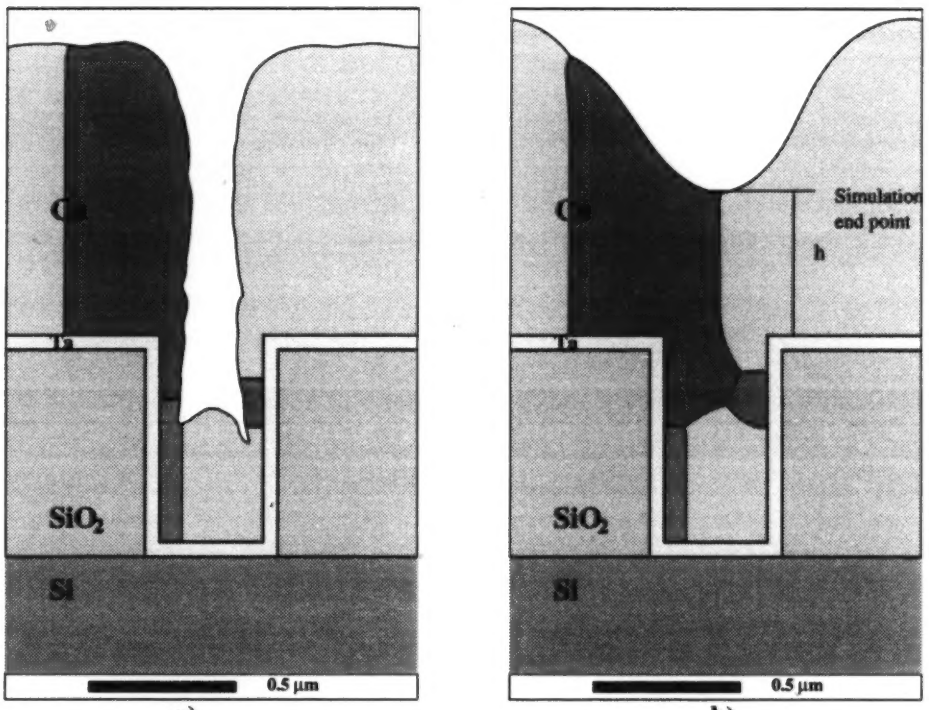

Figure 5.25 a) The original deposition profile (see Figure 5.24) with five arbitrarily added grain boundaries. b) The completed reflow simulation using a) as the initial profile. All reflow simulations were halted at the same point as shown in b).

results presented in Figure 5.26. The large number of grains (mostly added along the side-walls of the trench) rapidly get buried and contribute to the surface energetics for only a very short time. Thus, if many nuclei form on the sidewalls and bottom of the trench and the grains are covered soon into the reflow process, there should be minimal impact on the necessary reflow time needed. Grooves with longer lifetimes such as those higher up the side-wall of the profile tend to remain exposed throughout most of the anneal and substantially retard the process.

For given topographies and deposition conditions, a worst case scenario requiring the longest anneal time for successful reflow can be predicted. A reflow process utilizing the anneal time necessary for filling this trench should then be uniformly successful over the entire wafer. To determine this worst case scenario, knowledge of the Cu microstructure is necessary. It is noted that sputtered copper films on a Ta underlayer have an approximate

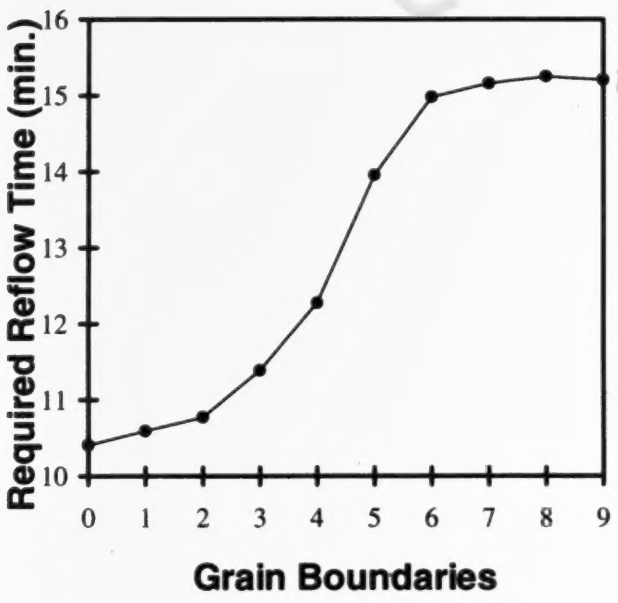

Figure 5.26 A plot of reflow times versus the number of grain boundaries indicates the extent to which the microstructure of the initial film plays a role in affecting the required reflow times.

grain size of 0.3 μm [78]. The experimental TEM of Figure 5.27 indicates there are many grains of the as-deposited copper distributed along the sidewalls of the trench and often a single large grain at the bottom. Thus an initial profile with a high density of grains along the sidewalls of the trench and with large grains of average size of 0.3 μm above the trench is assumed to be the microstructure representing the Cu film requiring the longest anneal time. This profile is most closely represented by the addition of nine grain boundaries to the test profile. The resulting reflow time is approximately 15 minutes which is within the level region of the graph (Figure 5.26). It should also be noted that some of the smaller grains along the sidewalls annealed out during the reflow.

Obviously, the variability of the grain boundary locations will have important implications to process development as reflow conditions must allow for worst case configurations. Tailoring the grain structure by adjusting deposition conditions, choosing specific wetting underlayers, or incorporating nucleation sites may increase control over the statistical variations in reflow rates.

Figure 5.27 Transmission electron micrograph of as deposited Cu showing the bimodal nature of the grain size distribution. The existence of many small grains along the sidewall is evident.

5.4 Summary

This chapter detailed the extensive study of the sputter reflow of copper using experimental and computational efforts. The experimental data was obtained by D. S. Gardner at Intel Components Research. The SIMSPUD and GROFILMS simulations were used to model the reflow process from the reactor to the feature scale. The research presented in this chapter was approached on both the fundamental and practical levels.

Chapter 6 Summary and Recommendations

6.1 Summary

6.1.1 GROFILMS model development

The GROFILMS simulator uses a line-segment/nodal approach to represent a thin film's surface profile and microstructure. Upon this basis, two growth models were developed, each sharing a common set of routines for nodal advancement and film representation. The first, originally conceived by Dr. S. Dew, is based upon quasi-equilibrium assumptions to thin film growth. That is, impinging particles will settle into energetically favorable locations within a specified diffusion length (a material and process-dependent simulation parameter). The algorithms and energetic calculations have since been extensively modified (Chapter 3) and tested (Chapter 4) by the author. The second model, developed solely during this thesis, features a kinetic description of the major physical processes that occur during thin film growth and post-deposition processing. In particular, surface diffusion due to capillarity was examined and implemented for post-deposition annealing simulations.

6.1.2 Fundamental physical properties and characteristics of thin films

Chapter 1 stated the need for process simulators that are based upon comprehensive physical models. GROFILMS was developed to be a physically based process simulator and therefore models many of the thin film properties, processes and characteristics. The material characteristics that influence development of metallization processes in the sub-micron regime include substrate wetting, grain boundary grooving, facetting, and microstructural development. These characteristics are governed by the material properties and the physical processes that occur during growth. The material properties are the interfacial energetics, diffusion parameters, and substrate surface properties. The physical processes are ballistic impingement of flux, nucleation, surface diffusion, and grain boundary migration. Since GROFILMS is a process simulator, the processing parameters are also incorporated into the models. These include processing temperatures, time, particle fluxes, and topogra-

phy.

6.1.3 Sputter Reflow of Copper

GROFILMS was used to extensively study the sputter reflow of copper for use in multilevel metallization of ULSI circuits. This study focussed upon processing conditions with emphasis placed upon determining success of the reflow process and to optimize the deposition and annealing parameters. Furthermore, an in-depth study of the effects of the fundamental properties of Cu on the reflow process was conducted.

The deposition parameters were analyzed with regard to their effects on the reflow process by using the reactor-scale simulator, SIMSPUD, or equivalent experimentally determined flux distributions. The accumulated results provide information for the assessment of facilities and their effectiveness as a sputter reflow system. For example, a long throw system (generating a collimated flux) was shown to deposit Cu films capable of successful reflow for a 0.35 μm 2:1 aspect ratio trench, while a short-throw system did not.

The flux distribution generated by the Intel Cu reflow deposition system was input into the GROFILMS simulator and subsequently used to generate a design of experiments aimed at optimizing the initial Cu film thickness. With a deposition of 1.125 μm of Cu, reflow times were shown to be reduced by 65% of that required by the minimum successful Cu film thickness (0.75 μm). Similar optimization can be performed for a variety of topographies and system parameters.

Variable topographies were shown to be a major factor in process development. Substrates with multiple feature sizes will tend to require much more extensive development to ensure reliable filling of all the features. Developing the deposition process was shown to be important to ensure the concurrent and successful filling of all the various features.

Filling vias was a special developmental issue for sputter reflow of copper. Simulations of the Intel Cu reflow system into a 0.5 μm via with aspect ratio 1:1 was not successful. The capillarity forces were great enough to rapidly close off the via before filling occurred. Alternative processing techniques are needed to solve the trench/via filling issues.

This simulation study of the sputter reflow of Cu analyzed the fundamental microstructural effects on reflow. It was determined that the microstructure of the film affects re-

flow by increasing the variability between trenches. The inhibiting effects of grain boundary grooving on the transport of Cu during reflow was demonstrated and shown to be important in determining the required anneal time. Control over the texture and microstructure during the deposition, i.e. depositing larger and fewer grains by choice of underlayer material, deposition temperature, or flux distribution, can be effective in optimizing a reliable reflow process.

6.2 Recommendations for future projects

The following recommendations and ideas for research projects are suggested for the present version of the GROFILMS/SIMSPUD simulators.

This thesis presented via reflow simulations. A comprehensive study requires a balance between experimental and simulation results. As reflow into vias is a significantly different process than reflow into trenches, a set of experimental results for use as verification of the GROFILMS simulation is necessary. Once convinced of the validity of the GROFILMS' results, a reasonable design of experiments that study the process can be developed and presented.

There exists an enthusiastic interest in the unique properties of thin films deposited by glancing angle deposition (*GLAD* films). GROFILMS can be used to answer the questions about the dominant physical growth processes, characterize the development of various structures and develop processes to deposit the types of films desired.

Electrochemical deposition has been developed to work with the SIMBAD simulator. This was accomplished by adding a finite element mesh above the film to model the varying concentration of the Cu precursors within solution. The transport analysis should be incorporated into the GROFILMS simulator. An electrochemical simulation using GROFILMS will have the added benefit of the capability of storing surface concentration data and calculating specific reaction rates.

The line-segment nodal structure with which GROFILMS represents the film and its microstructure can be used as the basis of other simulation analysis. For example, the results of a Ti GROFILMS deposition simulation were used with a unique transmission line matrix diffusion model to evaluate the effectiveness of the film as a barrier layer [110]. Also, other metallization properties can be evaluated. For example, electromigration-induced

voiding, stress evaluation, and heat transfer simulations could be developed to use the GROFILMS output.

The chemical vapour deposition abilities of the GROFILMS simulator will need to be verified against experimental results. Presently, the model has been evaluated in terms of diffusion, nucleation and growth of the film. Possible systems that are available for verifying GROFILMS could be the CVD deposition of Al from TIBA [111] or W from tungsten-hexafluoride [111]. These processes are used in fabrication and have been well studied for their kinetics and deposition results. Once verified, the GROFILMS simulator can be extended to study the alternatives such as Cu CVD or barrier layer deposition such as TiN CVD. Along with each of the possible processes to study, a collection of the relevant model parameters (reaction rates, activation energies, etc.) should be compiled.

Chemical vapour deposition is an important thin film processing technique. While the basis for simulating the feature-scale thin film growth during a CVD process is established, the precursor flux distributions are necessary for a complete simulation package. Thus, a reactor scale model (analogous to the existing PVD reactor scale model: SIMSPUD) that incorporates system geometry, temperatures, and gas flows is desired.

The variation in species composition within a film can be represented in a GROFILMS simulation. The underlying framework for composition representation is currently available in the present simulation. However, refinement of the code as well as verification of results are necessary. This type of information can provide clues to the performance of and development of such thin films as TiN, or TiW(N) barrier layers, and Al-Cu alloys. Impurity concentrations resulting from CVD processes and contamination due to ambient gases could also be evaluated.

The development of a fully three-dimensional thin film process simulator is another project that could be considered. A three-dimensional simulation can provide details of film properties that have previously been inferred or unavailable. For example, the formation of a polycrystalline film or a bamboo structure down the length of a trench can provide insight to developing a highly EM resistant metallization line. Simulations of via deposition with trenches (dual damascene) will benefit from a true three-dimensional representation.

The major concerns in the full three-dimensional project that must be addressed are the computation requirements, surface calculations (diffusion, energetics, populations),

three-dimensional surface representation and advancement, and flux generation. Each of these becomes more complicated and intractable in terms of numerical calculation. Novel computational algorithms will play an important role in this project.

The GROFILMS simulator is a comprehensive thin film simulator and thus requires many physical parameters. In order to solve the kinetic diffusion equations, reaction rates, adsorption/desorption rates, a database of material and reaction parameters is essential. It would be beneficial to have a collection of this data prepared in a database, such that a minimum number of assumptions need be made by the user.

References

[1] L. Gwennap, "Birth of a Chip," *Byte*, Dec. 1996.

[2] R. W. Keyes, The Physics of VLSI Systems, Addison-Wesly Pub. Co., Reading, Mass. (1987).

[3] Intel Corporation, Santa Clara, 2200 Mission College Blvd., Santa Clara, California 95052-8119, USA. Electronic source: http://www.intel.com/pressroom.html.

[4] Cable News Network, Inc. Stated goal of Intel chairman Andrew Grove. "Companies, Government Join to Shrink Computer Chip Size," http://www.cnn.com/TECH9709/11/shrinking.chips.ap/index.html. CNN Web posted at 9:06 p.m. EDT September 11, 1997.

[5] G. Moore, "Moore's Law Extended: The Return of Cleverness. *An Exclusive Interview with Gordon Moore*," *Solid State Technology* **40** (7), 364 (1997).

[6] J. Bokor, A. Neuruther, W. G. Oldham, "Advanced Lithography for ULSI," *IEEE Circuits and Devices*, January, 11 (1996).

[7] A. M Hawryluk, N. M. Ceglio, D. A. Markle, "EUV Lithography," *Solid State Technology* **40** (7), 151 (1997).

[8] J. Tao, N. W. Cheung, Chenming, "Electromigration Characteristics of Copper Interconnects", *IEEE Electron Device Lett.* **14** (5), 249 (1993).

[9] D. Pramanik, V. Jain, "Barrier Metals for ULSI Processing and Reliability," *Solid State Technology* May 1991, 97 (1991).

[10] J. P. Krusius, "Process Modeling for Submicron Complementary Metal-Oxide-Semiconductor Very Large Scale Integrated Circuits," *Journal of Vacuum Science and Technology A* **4** (3), 905 (1986).

[11] T. S. Cale, M. K. Jain, G. B. Raupp, "Programmed Rate Processing to Increase Throughput in LPCVD," *Journal of the Electrochemical Society* **137** (5), 1526 (1990).

[12] S. Hong, E. Kim, B-S Bae, K. No, S-C Lim, S-G Woo, Y-B Koh, "A Simulation Model for Thickness Profile of the Film Deposited Using Planar Circular Type Magnetron Sputtering Sources", *Journal of Vacuum Science and Technology A* **14** (5), 2721 (1996).

[13] J-R. Zhou, D. K. Ferry, "3D Simulation of Deep-Submicron Devices. How Impurity Atoms Affect Conductance," *IEEE Computational Science and Engineering*, p. 30, Summer (1995).

[14] L. J. Friedrich, S. K. Dew, M. Brett, T. Smy, "Thin Film Microstructure Modeling Through Line Segment Simulation," *Thin Solid Films* **266**, 83 (1995).

[15] D. Pramanik, "Aluminum-Based Metallurgy for Global Interconnects," *MRS Bulletin* November 1995, 57 (1995).

[16] D. Pramanik, A. N. Saxena, "Aluminum Metallization for ULSI," *Solid State Technology* **33**, 73 (1990).

[17] P.-H. Wang, P. S. Ho, C. Lee, H. Kawasaki, "Initial Void Formation in Bamboo Al-Cu(1%) Two-level Structure," Stress-Induced Phenomena in Metallization, edited by P. S. Ho, J. Bravman, C-Y. Li, J. Sanchez. AIP Conference Proceedings 373, Palo Alto, Ca , p 143 (1995).

[18] H. Toyoda, T. Kawanoue, S. Ito, M. Hasunuma, H. Kaneko, "Effects of Aluminum Texture on Electromigration Lifetime.," Stress-Induced Phenomena in Metallization, edited by P. S. Ho, J. Bravman, C-Y. Li, J. Sanchez. AIP Conference Proceedings 373, Palo Alto, Ca, p 169 (1995).

[19] T. Nogami, T. Nemoto, "Cu Behaviors Induced by Aging and Their Effects on Electromigration Resistance on Al-Cu Lines," Stress-Induced Phenomena in Metallization, edited by P. S. Ho, J. Bravman, C-Y. Li, J. Sanchez. AIP Conference Proceedings 373, Palo Alto, Ca, p 198 (1995).

[20] G. K. Rao, Multilevel Interconnect Technology, McGraw-Hill, p 8 (1993).

[21] T. Ohba, "Chemical-Vapor-Deposited Tungsten for Vertical Wiring," *MRS Bulletin* **20** (11), 46 (1995).

[22] International Conference on Metallurgical Coatings and Thin Films, San Diego, CA, (1997).

[23] D. S. Gardner, "Encapsulated Copper Interconnection Devices Using Sidewall Barriers", *Thin Solid Films* **262**, 104 (1995).

[24] Fishkill, N.Y., September 22, 1997, IBM announces CMOS 7S process technology. Web posted: http://www.chips.ibm.com/news/cmos7s.html. and CNN Web posted at: September 23, 1997 6:02 p.m. EDT (1802 GMT) http://cnn.com/TECH/9709/23/ chip.whats.next/index.html.

[25] P. Doppelt, T. H. Baum, "Chemical Vapor Deposition of Copper for IC Metallization: Precursor Chemistry and Molecular Structure", *MRS Bull.* **19**, 41, August (1994).

[26] V. M. Donnelly, M. E. Gross, "Copper metalorganic chemical vapor deposition reactions of hexafluoroacetylacetonate Cu(I) vinyltrimethylsilane and bis (hexafluoroacetylacetonate) Cu(II) adsorbed on titanium nitride", *Journal of Vacuum Science and Technology A*, **11** (1), 66 (1993).

[27] J-C Chiou, Y-J Chen, M-C Chen, "Copper Chemical Vapor Deposition from Cu(hexafluoroacetylacetonate)trimethylvinylsilane", *Journal of Electronic Materials* **23** (4), 383 (1994).

[28] P. L. Pai, C. H. Ting, *Proc. 6th VLSI Multilevel Interconnection Conference*, IEEE, New York, (1989) p. 258.

[29] J. S. H. Cho, H-K Kang, S. S. Wong, Y S-D., "Electroless Cu for VLSI", *MRS Bulletin* **18**, 31 (1993).

[30] B. J. Howard, C. Steinbruchel, *Applied Physics Letters* **59**, 914 (1991).

[31] M. J. Hampden-Smith, T. T. Kodas, "Copper Etching: New Chemical Approaches", *MRS Bulletin* **18,** 39 (1993).

[32] P. Singer, "Making the Move to Dual Damascene Processing," *Semiconductor International* **20** (9), 79 (1997).

[33] R. R. Uttecht, R. Geffken, *Proc. 8th VLSI Multilevel Interconnection Conference,* IEEE, New York, p. 20 (1991).

[34] S. P. Murarka, J. Steigerwald, R. J. Gutmann, *MRS Bulletin* **18**, 46 (1993).

[35] S. Wang, 'Barriers Against Copper Diffusion into Silicon and Drift Through Silicon Dioxide", *MRS Buletin* **19** (8) 30, (1994).

[36] T. Smy, S. K. Dew, M. J. Brett, *MRS Bulletin* **20**, 65 (1995).

[37] A. Natori, M. Fukuda, H. Yasunaga, "Monte Carlo Simulation of Heterogeneous Thin Film Growth," *Journal of Crystal Growth* **99**, 112 (1990).

[38] J. Salik, "Computer Simulation of Thin Film Nucleation and Growth," *Journal of Applied Physics* **57** (11), 5017 (1985).

[39] S. Ling, M. P. Anderson, "Development and Evolution of Thin Film Microstructures: A Monte Carlo Approach," *Journal of Electronic Materials* **17** (5), 459 (1988).

[40] D. J. Srolovitz, A. Mazor, B. G. Bukiet, P. S. Hagan, "Summary Abstract: Theory and Simulations of Zone II Microstructures in Thin Films," *Journal of Vacuum Science and Technology A* **6**(3), 1640 (1988).

[41] G. S. Bales, A. Zangwill, "Macroscopic Model for Columnar Growth of Amorphous Films by Sputter Deposition," *Journal of Vacuum Science and Technology A* **9** (1), 145 (1991).

[42] A. Mazor, B. G. Bukiey, D. J. Srolovitz, "The Effect of Vapor Incidence Upon Thin-Film Columnar Growth", *Journal of Vacuum Science and Technology A* **7** (3), 1386 (1989).

[43] J. Chen, "Model for Columnar Microstructure of Thin Solid Films", *Physical Review Letters* **56** (13), 1396 (1986).

[44] R. W. Smith, "A Kinetic Monte Carlo Simulation of Fiber Texture Formation During Thin Film Deposition", *Journal of Applied Physics* **81** (3), 1196 (1997).

[45] P. Ramanlal, L. M. Sandler, "Theory of Ballistic Aggregation", *Physical Review Letters* **54** (16), 1828 (1985).

[46] P. Meakin, P. Ramanlal, L. M. Sandler, R. C. Ball, "Ballistic Deposition on Surfaces", *Physical Review A*. **34** (6), 5091 (1986).

[47] P. K. Swaminathan, C. S. Murthy, M. J. Redmon, "Computer Simulations of Epitaxial Growth," *Physical Review B* **39** (7), 4541 (1989).

[48] T. Shibayanagi, H. Takatani, S. Hori, "Monte Carlo Simulation for the Behaviour of Low Mobility Grain Boundaries in Grain Growth," *Materials Transactions, JIM,* **32** (1), 25 (1991).

[49] H. J. Frost, C. V. Thompson, D. T. Walton, "Simulation of Thin Film Grain Structures - I. Grain Growth Stagnation," *Acta. Metall. Mater.* **38** (8), 1455 (1990).

[50] S. P. Chen, D. J. Srolovitz, A. F. Voter, "Computer Simulation on Surfaces and [001] Symmetric Tilt Grain Boundaries in Ni, Al, and Ni_3Al," *Journal of Materials Research* **4** (1), 62 (1989).

[51] A. F. Voter, "Interatomic Potentials for Atomistic Simulations," *MRS Bulletin* **21** (2), 17 (1996).

[52] H. Camon, Z. Moktadir, "Atomic Scale Simulation of Silicon Etched in Aqueous KOH Solution", *Sensors and Actuators A* **46-47**, 27 (1995).

[53] H. Liao, T. S. Cale, "Numerical Simulations of Thin Film Thermal Flow," *Thin Solid Films* **253**, 419 (1994).

[54] S. K. Dew, Processes and Simulation for Advanced Integrated Circuit Metallization, Ph.D. Dissertation, Electrical Engineering, University of Alberta, Edmonton, AB, (1992).

[55] C. Werner, J. I. Ulacia, F. C. Hopfmann, P. Flynn, *Journal of Electrochemical Society* **139**, 3423 (1989).

[56] E. Bar, J. Lorenz, "3D Simulation of Tungsten Low-Pressure Chemical Vapor Deposition in Contact Holes," *Applied Surface Science* **91**, 321 (1995).

[57] E. Bar, J Lorenz, "3-D Simulation of LPCVD Using Segment-Based Topography Discretization," *IEEE Transactions on Semiconductor Manufacturing* **9** (1), 67 (1996).

[58] J. G. Shaw, C. C. Tsai, "Monte Carlo Simulations of Plasma-deposited Amorphous Silicon," *Journal of Applied Physics* **64** (2), 699 (1988).

[59] S.-S. Han, L. Cai, G. S. May, A. Rohatgi, "Modeling the Growth of PECVD Silicon Nitride Films for Solar Cell Applications Using Neural Networks," *IEEE Transactions on Semiconductor Manufacturing* **9** (3), 303 (1996).

[60] C. C. Fang, V. Prasad, F. Jones, "Molecular Dynamics Modeling of Microstructure and Stresses in Sputter-Deposited Thin Films", *Journal of Vacuum Science and Technology A* **11** (5), 2778 (1993).

[61] S. Yamamoto, T Kure, M. Ohgo, T. Matsuzama, S. Tachi, H. Sunami, "A Two-Dimensional Etching Profile Simulator: ESPRIT," *IEEE Transactions on Computer-Aided Design* **6** (3), 417 (1987).

[62] W. Oldham, A. Neureuther, C. Sung, J. Reynolds, S. Nandgaonkar, "A General Simulator for VLSI Lithography and Etching Processes: Part II - Application to Deposition and Etching," *IEEE Transactions on Electron Devices* **27** (8), 1455 (1980).

[63] I. V. Katardjiev, G. Carter, M. J. Nobes, S. Berg, H.-O. Blom, "Three-dimensional Simulation of Surface Evolution During Growth and Erosion," *Journal of Vacuum Science and Technology A* **12** (1), 61 (1994).

[64] F. Sullivan, "Who Needs Efficient Algorithms?", *IEEE Computational Science and Engineering*, p. 1, Fall 1995.

[65] Y. Saito, S. Hirasawa, T Saito, H. Nezu, H. Yamaguchi, N. Owada, "Molecular dynamics Analysis of Reflow Process of Sputtered Aluminum Films", *IEEE Transactions on Semiconductor Manufacturing* **10** (1), 131 (1997).

[66] H. van Kranenburg, C. Lodder, "Tailoring Growth and Local Composition by Oblique-Incidence Deposition: A Review and New Experimental Data," *Materials Science and Engineering* **R11** (7), 295 (1994).

[67] A. Yuuki, Y. Matsui, K. Tachibana, "A Study on Radical Fluxes in Silane Plasma CVD from Trench Coverage Analysis," *Japanese Journal of Applied Physics* **28**, 212 (1989).

[68] K. Robbie, L. J. Friedrich, S. K. Dew, T. Smy, M. Brett, "Fabrication of Thin Films with Highly Porous Microstructures", *Journal of Vacuum Science and Technology A* **13** (3), 1032 (1995).

[69] S. K. Dew, T. Smy, M. Brett, *Japanese Journal of Applied Physics* **33**, 1140 (1994).

[70] M.J. Brett, S. K. Dew, T. J. Smy, "Thin Film Microstructure and Process Simulation Using SIMBAD," *Thin Films* **22**, 1 (1996).

[71] R. A. Sigsbee, "Vapor to Condensed-Phase Heterogeneous Nucleation", Nucleation, ed. Zettlemoyer, A. C., Marcel Dekker Inc., New York, N.Y., p. 163 (1969).

[72] B. A. Movchan, A. V. Demchishin, *Fiz. Metal. Metalloved.*, **28** 653 (1969).

[73] R. N. Tait, Thin Film Microstructure Effects in VLSI Metallization, Ph. D. Dissertation, Department of Electrical Engineering, University of Alberta, Edmonton (1992).

[74] J. A. Thornton, "The Microstructure of Sputter-Deposited Coatings", *Journal of Vacuum Science and Technology A*, **4** (6), 3059 (1986).

[75] J. A. Thornton, "Influences of Apparatus Geometry and Deposition Conditions on the Structure and Topography of Thick Sputtered Coatings", *Journal of Vacuum Science and Technology*, **11** (4), 66 (1974).

[76] R. Messier, A. P. Giri, R. A. Roy, "Revised Structure Zone Model for Thin film Physical Structure," *Journal of Vacuum Science and Technology A* **2** (2), 500 (1984).

[77] J. S. Colligon, "Energetic Condensation: Processes, Properties, and Products," *Journal of Vacuum Science and Technology A* **13** (3), 1649 (1995).

[78] D. P. Tracey, D. B. Knorr, "Texture and Microstructure of Thin Copper Films", *Journal of Electronic Materials* **22**, 611 (1993).

[79] J. M. Blakely, Introduction to the Properties of Crystal Surfaces, Pergamon Press, Oxford, 12 (1973).

[80] M. Nieuwenhuizen, H. B. Haanstra, *Philips Tech. Rev.* **27**, 87 (1966).

[81] R. N. Tait, T. Smy, M. J. Brett, *Thin Solid Films* **226**, 1966 (1993).

[82] T. Young, *Philos. Trans. Soc. London* **95**, 65 (1805).

[83] R. E. Johnson, *Journal of Physical Chemistry* **63**, 1655 (1959).

[84] T. Smy, S. S. Winterton, S. K. Dew, M. J. Brett, *Journal of Applied Physics* **78**, 3572 (1995).

[85] W. W. Mullins, "Theory of Thermal Grooving", *Journal of Applied. Physics* **28**, 333 (1957).

[86] P. Shewmon, Diffusion in Solids, Warrendale, Pa. : Minerals, Metals & Materials Society, (1989).

[87] W. W. Mullins, "Mass Transport at Interfaces in Single Component Systems," *Metallurgical and Materials Transactions A* **26A**, 1917 (1995).

[88] C. Herring, Physics of Powder Metallurgy, W. E. Kingston, ed., McGraw-Hill, New York, NY, 1951, p. 143.

[89] J. D. Verhoeven, Fundamentals of Physical Metallurgy, John Wiley & Sons, New York, 1975, p. 201.

[90] C. V. Thomson,"Secondary Grain Growth in Thin Films of Semiconductors: Theoretical Aspects," *Journal of Applied Physics* **58** (2), 763 (1985).

[91] S. Shingubara, H. Kotani, K. Ando, H. Sakaue, F. Nishiyama, T. Takahagi, "Effect of Interface Reaction and Wetting Properties on Al Reflow Characteristics," Advanced

Metallization and Interconnect Systems for ULSI Applications in 1996, Conference Proceedings ULSI XII, Materials Research Society, 1997. p. 117.

[92] L. J. Friedrich, K. Robbie, S. K. Dew, M. J. Brett, T. Smy, "Grain Oriented Thin Film Microstructure Simulator", Process Control, Diagnostics and Modeling in Semiconductor Manufacturing, editors: M. Meyyappan, D. J. Economou,S. W. Butler, 1995, p. 541.

[93] K. Ralls and J. Wulff, Introduction to Material Science and Engineering, John Wiley and Sons, New York, N.Y.1976.

[94] P. R. Besser, J. E. Sanchez, D. Field, "The Linewidth Dependence of Microstructure in Damascene Fabricated Aluminum Interconnects," *Advanced Metallization Conference in Boston*, 89 (1997).

[95] J. E. Taylor, J. W. Cahn, C. A. Handwerker, "Overview No. 98: I-Geometric Models of Crystal Growth," *Acta. Metall. Mater.* **40** (7), 1443 (1992).

[96] C. R. M. Grovenor, H. T. G. Hentzell, D. A. Smith, *Acta. Metall.* **32**, 773 (1984).

[97] D. S. Gardner, 1995 Proceedings of the VLSI Multilevel Interconnection Conference, ed. T. E. Wade, VMIC, 5316 Whitham Court, Tampa, p. 287 (1995).

[98] L. E. Murr, Interfacial Phenomena in Metals and Alloys, Addison - Wesley, Reading, Mass. (1975).

[99] K. Abe, Y. Harada, H. Onoda, 1995 Proceedings of the VLSI Multilevel Interconnection Conference, ed. T. E. Wade, VMIC, 5316 Whitham Court, Tampa, p. 308 (1995).

[100] Landolt-Bornstein, Numerical Data nd Functional Relationships in Science and Technology, Chapter 13. Springer-Verlag, Berlin, 1987.

[101] G. A. Chadwick, D. A. Smith, Grain Boundary Structure and Properties, Academic Press, New York, N. Y., 1976.

[102] T. Saito, N. Fukuda, H. Tamaguchi, S. Hirasawa, K. Hinode, N. Owada, "Cu Metallization with Low-pressure Long-throw Sputtering Method for Submicron Damascene Wiring," Advanced Metallization and Interconnect Systems for ULSI Applications in 1996, Conference Proceedings ULSI XII, Materials Research Society, 1997. p 149.

[103] J. N. Broughton, M. J. Brett, S. K. Dew, G. Este, " Ti Sputter Deposition at Low Pressures and Long Throw Distances," *IEEE Transactions on Semiconductor Manufacturing* **9** (1), 122 (1996).

[104] L-Y. Chen, W-Y Hsu, R. Tao, D. Cong, Q-Z. Hong, R. Mosely, V Cordasco, F. Chen, "Low Temperature Copper Planarization Using CVD and PVD Copper Process Integration," Advanced Metallization and Interconnect Systems for ULSI Applications in 1997, San Diego, CA, September 30 - October 2, 1997.

[105] R. Brain, Capillary-Driven Reflow of Thin Cu Films with Submicron, High Aspect Ratio Features, Ph.D. Dissertation, California Institute of Technology, Pasadena, California. (1996).

[106] L. J. Friedrich, D. S. Gardner, S. K. Dew, M. Brett, T. Smy, "Microstructural Effects on the Copper Reflow Process", 1996 Proceedings of the VLSI Multilevel Interconnection Conference, ed. T. E. Wade, p. 213 (1996).

[107] D. P. Tracey, D. B. Knorr, "Texture and Microstructure of Thin Copper Films", *Journal of Electronic Materials* **22**, 611 (1993).

[108] J. Tao, N. W. Cheung, Chenming, *IEEE Electron Device Lett.* **14** (5), 249 (1993).

[109] L. J. Friedrich, D. S. Gardner, S. K. Dew, M. J. Brett, T. Smy, "Copper Reflow Processing Times as a Function of Film Microstructure," Advanced Metallization and Interconnect Systems for ULSI Applications in 1996, Conference Proceedings ULSI XII, Materials Research Society, 1997. p 155.

[110] X. Gui, L. J. Friedrich, S. K. Dew, M. J. Brett, and T. Smy, "TLM Modeling of Grain Boundary Diffusion In Thin Films With Microstructural Details", Proc. 1st Int. Workshop on Transmission-Line Matrix (TLM) Modeling - Theory & Applications, Victoria, B.C., Canada, Aug. 1995, pg. 129.

[111] J. R. Creighton, J. E. Parmeter, "Metal CVD for Microelectronic Applications: An Examination of Surface Chemistry and Kinetics," *Critical Reviews in Solid State Materials Science* **18** (2), 175 (1993).

[112] M. E. Coltrin, R. J. Kee, J. A. Miller, "A Mathematical Model of the Coupled Fluid Mechanics and Chemical Kinetics in a Chemical Vapor Deposition Reactor," *Journal of Electrochemical Society: Solid-State Science and Technology*, February 1984, 425 (1984).

[113] G. S. Bales, A. C. Redfield, A. Zangwill, "Growth Dynamics of Chemical Vapor Deposition," *Physical Review Letters* **62** (7), 776 (1989).

[114] S. K. Dew, T. Smy, M. J. Brett, "Simulation of the Microstructure of Chemical Vapor Deposited Refractory Thin Films," *Journal of Vacuum Science and Technology B* **10** (2), 618, (1992).

[115] M. J. Cooke, G. Harris, *Journal of Vacuum Science and Technology A* **7**, 3217 (1989).

[116] T. S. Cale, G. B. Raupp, *Journal of Vacuum Science and Technology B* **8**, 1242 (1990).

[117] M .J. Cooke, G. Harris, "Monte Carlo Simulation of Thin-Film Deposition in a Rectangular Groove," *Journal of Vacuum Science and Technology A* **7** (6), 3217 (1989).

[118] J. J. Hsieh, "Influence of Surface-Activated Reaction Kinetics on Low-Pressure Chemical Vapor Deposition Conformality Over Micro Features," *Journal of Vacuum Science and Technology A* **11** (1), 78 (1993).

[119] K. J. Laidler, Chemical Kinetics 3rd Edition., Harper & Row, Publishers Inc., New York, N.Y. (1987) Chapter 7.

[120] Kisliuk, "Using Contact Resistance to Measure Adsorption of Gases on Metals," *Bell Syst. Tech. Journal* **37** (4), 925 (1958).

[121] J. R. Creighton, "The Surface Chemistry and Kinetics of Tungsten Chemical Vapor Deposition and Selectivity Loss," *Thin Solid Films* **241**, 310 (1994).

Appendix A Chemical Vapour Deposition Simulation

A.1 Modeling the physical processes of chemical vapour deposition

In a typical CVD reactor, the deposition can be described by seven basic processes as presented schematically in Figure A.1. The first and last of which are the forced transport of reactant and by-product gases into and out of the system. This transport of gases through the system has been frequently modeled using fluid mechanics on the reactor scale [112]. The reactor scale models can be used to predict gas phase temperature, velocity and chemical species concentration profiles.

The second and sixth stages are the transport of reactants and by-product gases to and from the substrate and the ambient gases. This transport is primarily due to diffusion (at typical pressures) and is modeled by diffusive flux equations [113] or ballistic transport of particles [114]. The ballistic component of the reactants in the gas phase leads to a geometry dependent nonuniform flux distribution and thus possible nonconformal film coverage on the surface. Scattering of the flux on the features, however, is also very important in determining film conformality. Monte Carlo models were developed to directly simulate the scattering process [114] [115]. Since the Monte Carlo method can be computationally intensive, especially in cases of high scattering probabilities, analytical integral-differential material balance equations for molecular transport have been solved [116].

The third step in a typical CVD process is the adsorption of the reactant gases onto the surface. The adsorbates are often mobile and can diffuse along the surface. As surface diffusion of the adsorbates can redistribute the concentration of reactants along the surface, it can be an important mechanism that may influence film conformality.

The adsorbed species then react in the fourth step to form a solid deposit and volatile by-products. The fifth step is the desorption of both the precursors and the reaction by-products. Each of the process are listed in Table A.1 along with the scale at which each is commonly modeled.

Table A.1: The fundamental processes during thin film growth by typical chemical vapour deposition.

Process	Scale
Bulk gas transport	System
Gas transport to surface	System/Feature
Adsorption	Feature
Surface Reactions	Feature
Desorption	Feature
Gas transport from the surface	System/Feature
Bulk gas transport (exhaust)	System

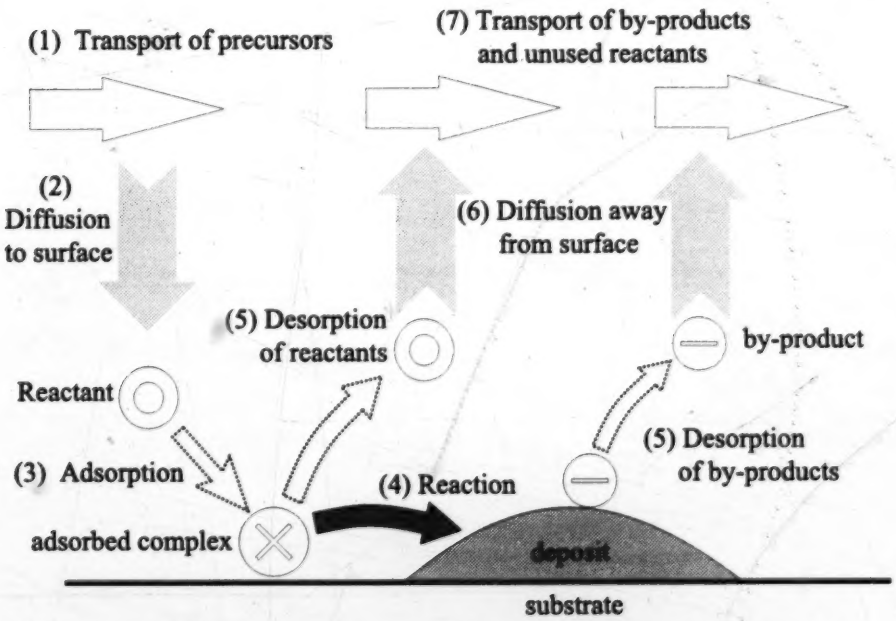

Figure A.1 A schematic diagram detailing the seven basic processes that occur during the deposition of a thin film via chemical vapour deposition.

GROFILMS simulates the physical and chemical processes directly above and on the substrate. These processes are the direct ballistic impingement of the precursor molecules from the vapour phase, scattering of the molecules from the surface, surface coverage and mechanism dependent adsorption and desorption of the precursor and product gases, surface chemical reactions of arbitrary order, adatom surface diffusion and capillarity driven surface diffusion of the film. This appendix will summarize the work that has been done with respect to the development of the GROFILMS CVD model.

A.2 Quasi-equilibrium CVD model

Many of the Monte Carlo simulations make the kinetic assumption that the deposition reaction is first order and the fraction of the impinging particles that are consumed by this reaction is characterized by a sticking coefficient, s [114] [67]. The sticking coefficient will be dependent upon adsorption and desorption rates (R_i and R_d) of the precursors as well as the overall rate of the limiting reaction (R_r) according to the relationship [117]:

$$s = \left(1 + \frac{R_d + R_i}{R_r}\right)^{-1} \tag{A.1}$$

The sticking coefficient model of the CVD reaction kinetics is a simple model easily incorporated into the quasi-equilibrium GROFILMS simulator. Essentially, an impinging particle will represent the reaction precursor in the gaseous phase. Upon impact, there is a finite probability that the precursor will react to form the solid species (the probability is typically 1.0 for PVD simulations). The other option is the desorption of the precursor back into the vapour where it follows another ballistic trajectory. The reemergence into the gas phase can effectively transport the precursors over long ranges into regions of the topography normally difficult to access due to shadowing. Thus, filling of very deep topographies is possible.

The CVD process studied in this section is the deposition of tungsten (W) from tungsten hexaflouride (WF_6) and silane (SiH_4). The rate-limiting reaction is dependent upon processing conditions. Thus for each process, an empirically determined sticking coefficient is necessary. However, qualitative changes in film coverage and microstructure can be determined by varying the sticking coefficient to reflect the changes in process condi-

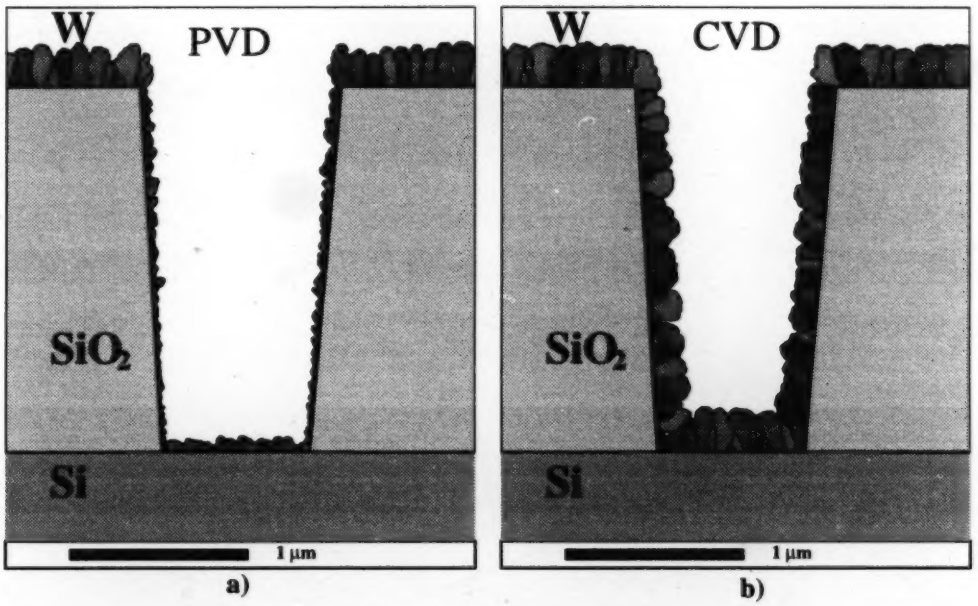

Figure A.2 a) 0.25 μm PVD deposition of W into a 2.5 μm deep trench showing very low sidewall and bottom coverages. b) 0.25 μm CVD deposition of W in the same trench reveals excellent sidewall and bottom coverage. The sticking coefficient was 0.01.

tions [114].

The simulations of Figure A.2 show the results of W PVD (unity sticking coefficient) and W CVD (sticking coefficient of 0.01) films deposited 0.25 μm thick into a 2.5 μm deep trench. The PVD simulation (Figure A.2 a)) reveals a highly columnar microstructure, especially along the sidewalls where the columns are oriented toward the vertical. The bottom coverage is 0.375 and the minimum sidewall coverage is a mere 0.125. This film compares to the W CVD simulation (Figure A.2 b)) using a sticking coefficient of 0.01 and which has grown a denser film with bottom coverage of unity and a minimum sidewall coverage of 0.5. The columns along the sidewall of the trench do not exhibit a preferred orientation as evident by the PVD simulation.

A.3 Kinetic model of CVD

The kinetic GROFILMS simulator was developed to incorporate the physical and chemical mechanisms that ultimately control the deposition rates of a CVD process. It is found that a single parameter sticking coefficient model may qualitatively describe film

growth for certain regimes, though it will not necessarily adequately describe the complicated kinetics that do occur. For example, the deposition rate of the CVD process will be dependent upon the available concentrations of the reactants upon the surface (assuming a single rate-limiting reaction). The reactant concentrations will in turn depend upon the adsorption rates and the available adsorption sites (thus the concentration of adsorbed (reactant or by-product) species will also determine adsorption rates). Furthermore, the relative reactant surface concentrations will depend upon adsorption mechanism, gas pressures, reaction rates and temperatures. To study processes that exhibit this complicated, interdependent system of rates and mechanisms requires a simulator based upon the fundamental process models. The following sections describe the development of the kinetic GROFILMS simulator for the study of CVD systems and processes.

A.3.1 Gas Phase Ballistic Transport

The first step in any film growth process is to transport a precursor element through the vapour phase to the substrate. Knowledge of the gas phase and adatom transport mechanisms during film growth are of vital importance in determining the evolution of thin film growth over ULSI topography. These mechanisms are direct ballistic impingement from the vapour phase and re-emission from the surface.

GROFILMS generate particles and launches them from randomly chosen locations immediately above the substrate. Each particle is given a linear trajectory predetermined from an angular distribution function describing the incoming flux. Gas phase collisions between the precursor species are not simulated by GROFILMS. This omission is justified as there is infrequent interaction between CVD particles due to the low pressures within the system. Typical mean free paths of the gas phase precursor in a CVD system are of the order of 10 - 100 μm, much larger than the features sizes under consideration.

GROFILMS models the impingement of flux by using kinetic rate equations. However, the spatial distribution of the impinging flux is determined by a Monte Carlo generation of the ballistic precursor flux. To bridge the two models, a sufficiently large number of particles are launched above the substrate to determine an impingement factor along the surface of the film which in turn is used to solve the rate equations. To obtain the statistical description of the ballistic processes, each particle is initially given a weight of unity, $w_j = 1$.

Upon impact at a specific node, a chemisorption probability is calculated and the particle weight is reduced by that amount

$$w_{j,k} = w_{j,k-1} - s_i \tag{A.3}$$

Here, j is the particle index, k is the impact index for this particle. Impact sites are labelled i and s_i is the chemisorption probability at i. A complete discussion of the chemisorption problem follows.

If the particle weight is non-zero after such an impact, a re-emission angle is calculated on the basis of specular reflection and the particle is re-launched. The launch - impact - re-emission cycle continues until either the particle weight has been reduced virtually zero or the particle has reentered the source gas. Thus, the impact statistics at each node can be described by

$$I_i = \frac{1}{I_0}\sum_{j'} w_{j',k} \tag{A.4}$$

where the subscript j' indicates the particle in the vapour phase that impinges upon site i and I_0 is a normalization factor.

GROFILMS is developed with the intent to provide a tractable simulation. The spatial results of the computationally expensive Monte Carlo generation of the ballistic flux is stored in the surface nodes along the film profile. As the film grows and the surfaces advance, the ballistic component requires recalculation. To minimize computation, it is assumed that the spatial distribution of fluxes need only be calculated when sufficient surface advancement has occurred. Further, a large fraction of the information in the spatial distribution is kept from one iteration to the next. The newly calculated distribution is then calculated on the basis of the historical distribution in concert with the newly obtained ballistic generation of flux. By keeping the information from past iterations, a smaller number of particles need to be generated, thus saving important computational time.

A.3.2 Chemisorption probabilities

A sticking coefficient should not be used as a first- principle parameter as it can be feature and flux dependent [118]. In particular, adsorption rates of the precursors will be dependent upon surface coverages (of reactants and by-products) which in turn will be re-

lated to the local reaction and desorption rates. Therefore, the chemisorption probability used in equation (A.3) is written as $s_i(\theta_i)$ where the chemisorption probability is determined by the local surface properties, θ_i, at each impact site, i.

A model, first proposed by Langmuir, describes the kinetics of nondissociative adsorption processes by allowing all particles impinging upon empty lattice sites to instantly chemisorb while the others bounced off occupied sites [119]. This leads to the chemisorption probability being a linearly decreasing function of surface coverage and is given as

$$s = s_0(1 - \theta) . \tag{A.5}$$

Here s is the chemisorption probability, θ is the surface coverage and s_0 is the zero coverage probability. This is a rather simplistic model. In 1958, Kisliuk derived a sticking coefficient function considering mobile physisorbed precursor states [120]. This model allows for impinging particles to physisorb at any site. The physisorbed adatoms may then either desorb or move along the surface until a suitable chemisorption site is found. The expression for the chemisorption probability then becomes

$$s = s_0 \frac{(1 - \theta)}{(1 - \theta + K\theta)} , \tag{A.6}$$

where K is a probability factor depending upon the desorption (k_d) and diffusion (k_m) rates via the relation

$$K = \frac{k_d}{k_d + k_m} . \tag{A.7}$$

Under the special condition of immobile adatoms, $k_m = 0$, K becomes unity and (A.6) reduces to Langmuir's equation (A.5). As the precursor mobility becomes more dominant, K decreases and the chemisorption probability remains high until the surface coverage is near saturation. Kisliuk's model has been extended further by incorporating island formation and site revisiting (the adatoms can visit a chemisorption site more than once). The final expression depends only upon the variables θ and K yet accounts for two, four, and six step site revisiting. The analysis was completed for both square and hexagonal lattice structures.

By knowing *a priori* the kinetics of the adsorption processes for a given system any

functional form for the chemisorption probability can be incorporated into a GROFILMS algorithm. Further, this analysis can be extended to a variable number of species. Each species in the vapour phase, labeled by g, will have its own impingement factor, $I_i(g)$.

A.4 Surface activated reaction kinetics

The concept of surface activated reaction kinetics is used in the GROFILMS CVD model. The kinetics require the adsorption of the precursor species, $A_{i(g)}$, onto available surface sites, $*$, which then become an activated species: A_i^*. The special case of a simple adsorption reaction is shown in (A.8) (other possibilities include adsorption with decomposition whereby two sites, $2*$, are required).

$$A_{i(g)} + * \leftrightarrow A_i^* \tag{A.8}$$

i in the above discussion and (A.8) determines which precursor species is reacting. The surface-activated species then reacts to deposit the solid film, $S_{(s)}$ and j volatile by-products, X_j^*. (A.9) shows an example of this reaction whereby a simple decomposition occurs.

$$xA_i^* \rightarrow yS_{(s)} + zX_j^* \tag{A.9}$$

where x, y, and z are coefficients for the mass balance equations. When two reactants are required, the surface reaction becomes:

$$wA_i^* + xA_{j\neq i}^* \rightarrow yS_{(s)} + zX_j^* \tag{A.10}$$

with w also a coefficient. Any of the j by-products may instantly desorb in the reaction equations of (A.9) and (A.10) or may linger as inhibitors or poisons slowing further adsorption of the precursors until the desorption reaction occurs freeing up a surface site:

$$X_j^* \rightarrow X_{j(g)} + * \tag{A.11}$$

The influence of the surface-activated reactions on the deposition properties requires further investigation. One can speculate from the above discussion that the sticking probability, as dependent upon surface coverages (equations (A.5) and (A.6)), will necessarily vary strongly on the reaction kinetics on the surface. Thus in total, the sticking coefficient is a complex function of precursor ballistics, feature geometries, kinetic rates, and deposi-

tion history. Most experimental validation done was based on the first-order sticking parameter model. As the reaction kinetics are more complicated than the first-order assumption, the range of validity of these models is in question. However, each of the surface reactions has an associated rate equation that must be solved kinetically. Acquiring experimental data on each of these intrinsic rate equations is difficult. Thus simplification of the system to reactions most likely to be the rate limiting step may be required.

A.4.1 Adsorption kinetics

Adsorption is the process by which molecular or atomic species in a gaseous phase bind to a surface. The binding mechanism is either physisorption or chemisorption, the latter being much stronger. For the adsorption processes concerned, it is assumed that all species adsorbing to a surface are physisorbing with chemisorption saved for incorporation of the deposit into the solid.

Adsorption of gaseous species is handled by GROFILMS by first determining a specific adsorption reaction rate, $k_a(g)$, for each gas, g (more than one gaseous precursor adsorbing onto the surface will result in competitive adsorption). This adsorption rate can be found empirically or can be predicted using the theory of absolute reaction rates. The following form is the most general equation for the specific adsorption rate constant [119].

$$k_a = k_{oa}\exp\left(\frac{-\varepsilon_0}{kT}\right) \tag{A.12}$$

where

$$k_{oa} = \frac{kT}{h}\frac{f^\circ}{F_g f_s}. \tag{A.13}$$

The lower case f's are complete partition functions and the upper case F represents the partition functions per unit volume of the gaseous species. The subscripts g and s refer to the reactants: gaseous species and adsorption centers respectively and the superscript $^\circ$ refers to the activated species.

The adsorption rate over the entire surface is $\nu_a = c_g k_a$, where c_g is the concentration of the precursor species per cubic centimeter in the gas phase. Under the specific conditions of simple adsorption of the gaseous species onto a mobile adsorption layer the most

general case (A.12) reduces to:

$$\nu_a = c_g \frac{kT}{h} \cdot \frac{h}{(2\pi mkT)^{1/2}} \exp\left(\frac{-\varepsilon_0}{kT}\right) \tag{A.14}$$

If the gas is considered to be ideal, the value $c_g kT$ can be replaced by the pressure, p. Further, if no activation energy for adsorption is needed, $\varepsilon_0 = 0$, (A.14) reduces to

$$\nu_a = \frac{p}{(2\pi mkT)^{1/2}}, \tag{A.15}$$

This is the familiar Hertz - Knudsen equation describing the number of gas molecules striking a surface 1 cm^2 in unit time.

Another adsorption example considers when gas adsorbing onto the surface forms an immobile layer. Thus the translational contribution of the activated species and the partition function of the adsorption centers, f_s, are unity (ignoring the vibrational and rotational contributions). Equation (A.12) then becomes:

$$\nu_a = c_g c_s \cdot \frac{h^2}{(2\pi m)^{3/2}(kT)^{1/2}} \exp\left(\frac{-\varepsilon_0}{kT}\right) \tag{A.16}$$

Here c_s is the concentration of adsorption sites per square centimeter of the surface.

The adsorption rate is proportional to the concentration of the precursor in the gas phase, c_g. However, this concentration is weighted by the impingement statistics along the surface of the film. Thus the rate of adsorption at each location along the surface, i, is multiplied by the normalized impact statistics of (A.4):

$$\nu_a' = \nu_a I_i \tag{A.17}$$

A.4.2 Desorption

As with the derivation of the adsorption rate equation, a desorption rate, ν_d, can be found from the theory of absolute rates [119]:

$$\nu_d = c_a k_{od} \cdot \exp\left(\frac{-\varepsilon_1}{kT}\right). \tag{A.18}$$

Here, c_a is the concentration of adsorbed complexes, k_{od} is the pre-exponential factor depending upon the partition functions of the activated and adsorbed complexes, and ε_1 is the energy of activation for desorption per molecule. Typical desorption rates will depend upon the concentration of the species, c_a, the thermal energy, and an activation energy, ε_1.

A.5 Adatom and capillarity diffusion

Each adsorbate can diffuse according to its properties outlined by the user input or material defaults. The diffusion of adsorbates can lead to better film coverages as the reactants can diffuse into high aspect ratio topography that is geometrically shadowed from the ballistic component of impinging particles.

Adatom diffusion on the substrate and film surfaces is modeled using Fick's first law of diffusion. This law relates the flux of material to the local concentration gradient:

$$J = -D\nabla c(x) \tag{A.19}$$

The diffusion coefficient, D, is dependent upon temperature in an Arrhenius manner:

$$D = D_0 \exp\left(-\frac{E_a}{kT}\right) \tag{A.20}$$

A simple finite difference algorithmic approach is used to determine the flux of particles across the simulation space.

Diffusion of material driven by capillarity is considered. This topic is extensively discussed in chapters 2 and 3.

A.6 Chemical reactions

Surface reactions are of primary importance in all CVD processes. It is these reactions that result in the deposition of the film onto the substrate. The reaction calculations depend upon rate equations and mass balance equations. Given the surface reaction equations ((A.9) or (A.10)), and knowing the surface concentrations and reaction rates, the number of reactions taking place in a time step can be calculated.

The rate equation is reaction specific. An example of a rate equation for (A.10) can look like:

$$v_r = k_r[A_i]^{\alpha}[A_j]^{\beta} \tag{A.21}$$

where v_r and k_r are the reaction rate and reaction rate coefficient respectively. The brackets denote species concentration values and α and β indicate to which order the rate is dependent. The value of k_r can be determined from experiment or predicted from the theory of absolute rates [119].

The kinetic algorithms utilize both the rate equations and the mass balance equations to determine the change in the present species concentrations and the volume of solid deposited.

A.7 Simulations of tungsten chemical vapour deposition

The reduction of tungsten hexaflouride by hydrogen is a W CVD process that will deposit tungsten thin films [111]. The following equations simplify the description of the reactions that occur during this W CVD process. The first is the adsorption of hydrogen onto empty sites (*) on the surface:

$$H_{2(g)} + 2* \leftrightarrow 2H_{(a)} \tag{A.22}$$

Next is the dissociation of WF_6 onto the surface leaving a solid deposit and adsorbed fluorine adatoms. This equation actually compiles the dissociation reactions of the sub-fluorides (WF_x) into a single representative equation.

$$WF_{6(g)} + 6* \rightarrow 6F_{(a)} + W_{(s)} \tag{A.23}$$

The final reaction combines the fluorine and hydrogen adatoms into a volatile species that immediately desorbs from the surface.

$$F_{(a)} + H_{(a)} \rightarrow HF_{(g)} + 2* \tag{A.24}$$

The reaction proceeds through the irreversible step between $F_{(a)}$ and $H_{(a)}$. An overall deposition rate law that encompasses the previous reactions and their rates can is written as:

$$\text{rate} = k_r\theta_F\theta_H = KP(WF_6)^{1/6}P(H_2)^{1/2} \tag{A.25}$$

This rate equation indicates a 1/2 order dependence on $P(H_2)$. The 1/2 order dependence is readily seen under typical processing conditions [121].

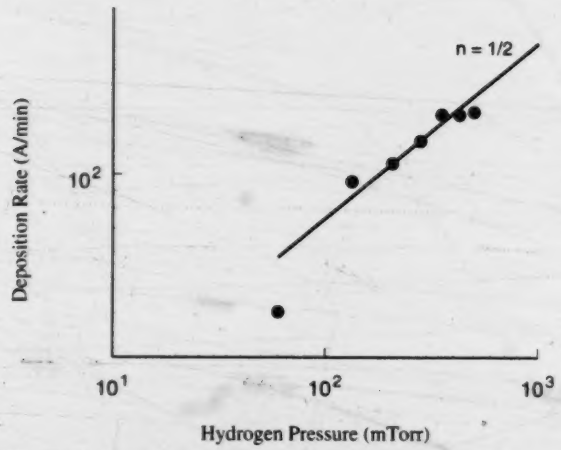

Figure A.3 Deposition rate dependence upon H_2 pressure. The line indicates the 1/2 order dependence.

The reaction equations of (A.22) to (A.24) are used in the GROFILMS simulator to simulation W CVD and determine deposition rates under varying conditions. The rates of each reaction was estimated and calibrated against experimentally obtained results. The kinetic and processing parameters are listed in Table A.2.

The 1/2 order dependence on the pressure of H_2 is reproduced by the GROFILMS simulator. These results are presented in Figure A.3 with the line indicating true 1/2 order dependence. Deviation from 1/2 order behaviour at lower pressures is expected from Langmuir-Hinshelwood kinetics as discussed in the next paragraph in terms of WF_6 pressure dependence.

Table A.2: Reaction and process parameters used in obtaining the simulated results of Figure A.3

Reaction (A.22) rate	10^5 /s/cm^2
Reaction (A.23) rate	10^4 /s/cm^2
Reaction (A.24) rate	10^5 /s/cm^2
WF_6 pressure	25 mTorr
Temperature	350 °C

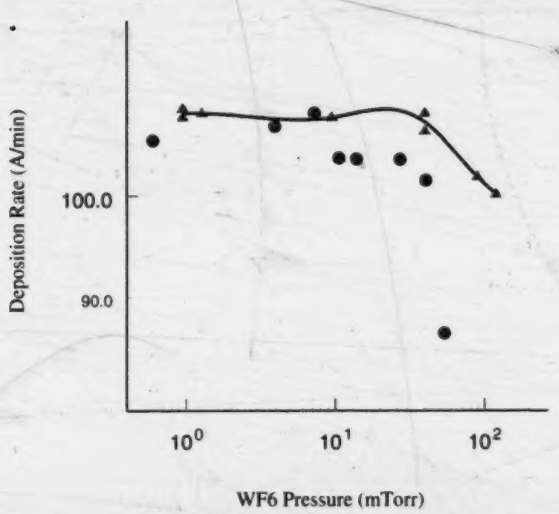

Figure A.4 Deposition rate dependence upon WF_6 pressure. The circles are the simulation results and indicate a negative order dependence at higher WF_6 pressures. The triangles and the line are experimentally obtained data as taken from reference [121] and also indicate the shift to negative order.

If the reactants of (A.24) compete for surface sites via Langmuir-Hinshelwood kinetics, the rate of production of $HF_{(g)}$ will be positive order in P_{WF_6} at low WF_6 pressure and negative order in P_{WF_6} at high WF_6 pressure. This behaviour arises as the reaction rate is governed by the low fluorine concentration on the surface. The available fluorine and thus the reaction rate increases with P_{WF_6} (positive order). At high WF_6 pressure, the surface sites are filled by the fluorine and the number available to adsorbing H decreases with increasing P_{WF_6}. Thus, the reaction rate will also decrease (negative order).

Figure A.4 presents experimental [121] (triangles) and simulation (circles) results of W deposition rates as a function of P_{WF_6}. The transition to negative order dependence is expected from Langmuir-Hinshelwood surface reactions and is shown by both results at P_{WF_6} above 80 mTorr. The H_2 pressure was kept constant at 40 mTorr and P_{WF_6} was varied over two orders of magnitude.